

**NUMERICAL STUDY ON TIDAL CURRENTS AND BED
MORPHOLOGY IN SITTAUNG RIVER ESTUARY, MYANMAR**

A Dissertation

Submitted to the National Graduate Institute for Policy Studies (GRIPS)
and International Centre for Water Hazard and Risk Management (ICHARM),

Public Works Research Institute (PWRI)

in Partial Fulfillment of the Requirements for the Degree of

Ph.D. in Disaster Management

by

Tanjir Saif Ahmed

September 2020

Declaration

Except where specific reference has been made to the work of others, the work embodied in this thesis is the result of investigation carried out by the author. No part of this thesis has been submitted or is being concurrently submitted in candidature for any degree at any other institution.

Tanjir Saif Ahmed

Abstract

Present study describes tidal currents, sediment transportation, sand bar migration and bank erosion of the Sittaung River estuary in Myanmar based on analysis of satellite images, field investigation and numerical simulation. Stream channels and sand bars move dramatically leading to severe bank erosion at a rate of around 1 km every year at the most active areas. Numerical tool is provided for prediction of drastic morphological changes and probable countermeasures against sediment induced disaster like bank erosion are recommended. Contents of this study are organized in five chapters.

Chapter 1 briefly describes the background, challenges and issues associated with estuary morpho-dynamics of the study area, necessity and position of the present study through literature reviews. Understanding sediment transport processes in estuaries composed of very fine sediment is justified and probable contribution of the study in scientific field are described here.

Chapter 2 discusses the geo-morphological and hydrological features of the study area, intensity and severity of bank erosion by means of satellite images and data collected during field investigation. Tidal bores, strong tidal currents and presence of very fine particles with mean diameter of 0.02 to 0.04 mm as bed and bank materials impact erodibility and transportability of such materials so actively.

Chapter 3 describes the weakness of existing formulas in treating fine sediments. To solve this issue, a new model is proposed for treating sediment transport process of very fine sediment and combined it with the depth-averaged two-dimensional Reynolds equations to simulate tidal bores, associated tidal currents, sediment transportation and active morphological changes. The proposed model is tested for validity, by being applied to the estimation of suspended sediment concentration and particle sizes. Computed results show that tidal bores and associated tidal currents are reproduced well where the

bore is identified as a discontinuous water surface configuration and that the particle sizes of suspended sediment are predicted well.

Chapter 4 describes numerical results on stream channel pattern and sand bar evolution using the numerical tool proposed in the previous chapter. Such results are compared with available satellite images and data obtained during field investigation. Channel bifurcation and channel closing are also reproduced. It is understood that such channel-change elements are responsible for the development process of sand bars and that the cyclic change of the bank line shifting may be caused by stream channel bifurcation. In addition, spur dykes are employed on the created morphology for channel-change and sand-bar control purposes. The analysis results show that such control structures can be effective as hard countermeasures to control severe erosion in the estuary. The periodicity of a decadal scale is simulated on smaller temporal and spatial scales. The results show that stream channel bifurcation characteristics is the governing factor behind the periodicity of the channel change. The lifetime of one channel can be quantified as a ratio of the cumulative volume of suspended sediment discharge and suspended sediment discharge along the channel. Long term morphological changes are discussed based on experimental study and necessary indication is provided for future prediction.

Such tool can be employed for the prediction of channel change and sand bar deformation, identification of vulnerable locations to bank erosion and probable countermeasures for combating sediment induced natural disasters in the estuaries composed of such fine particles around the world. Dissemination of such outputs to the policymakers and stakeholders are discussed for future planning of socio-economic development of the estuary region.

Acknowledgement

I express my sincere gratitude to my supervisor Professor Shinji EGASHIRA, for constantly taking care of me, my study and reviewing all my study outputs with time and effort. He contributed to my study with utmost suggestions and guidance which played an instrumental role in bringing my study into the present shape. He taught me hydraulics and sediment hydraulics during this study period which improved my understanding very much on this field. I thankfully remember the times of discussions before my qualifying examination, after every field investigation and validation of simulated results and also before preliminary presentations and the final defense. Above all, through the entire journey that made my path smoother gradually. Such knowledge will be helpful to judge and handle sediment issues in the practical field in the future.

I am grateful to Associate Professor Atsuiro YOROZUYA who kindly joined field measurements to my study area in October- 2017, February- 2018, 2019 and 2020 and provided necessary field information that were critical for validating the simulated results. Moreover, I was given opportunities to join field measurements with him in Bangladesh in August- 2017 and 2018. In both opportunities, I travelled along the major rivers of Bangladesh and learnt techniques to observe fluvial processes more actively. Such experience is a big asset for my career.

I express my sincere gratitude to Professor Hitoshi IEDA for his suggestive comments during my qualifying examination, preliminary presentations and the final defense. He guided me to think deeply about the contribution of the research on socio-economic aspect and challenges that might incur for globally sensitive issues like climate change and sea level rise. His comments helped me a lot to come up with future scopes of extended studies.

I received preliminary guidance from professor Takenori SHIMOZONO. He gave me useful suggestions for setting up initial and boundary conditions for numerical simulation. He provided valuable comments relating to long term simulation of morphological changes in the estuary and they helped me discuss prediction of long term morphological change in the target region.

I am grateful to Professor Toshio KOIKE as he kindly joined all the research meetings, suggested to include greater scientific challenges that the study area faces and actively provided necessary guidance which motivated me to conduct numerical simulations on different experimental channels.

I am grateful to Dr. Daisuke HARADA for his kind support and cooperation in teaching operation of numerical models which are the key tools to my study. I thank all the ICHARM Researchers, Dr. Naoko NAGUMO and other supporting staff who actively participated in field investigations, joined research meetings, supported me with valuable comments and collected necessary information from the study area.

During this hectic study- period, I lost my father Mr. Md. Saifullah Talukder. He is my inspiration and strength. After his demise, it was severe mental stress for me to concentrate in my daily life and study. I dedicate this study to him. I have mother and one younger brother in my family. They have been by my side all the time. I am sincerely thankful to them.

I would like to express deepest respect to the authority of the National Graduate Institute for Policy Studies (GRIPS) for selecting and supporting me as a doctoral program student. I am indebted to the International Centre for Water Hazard and Risk Management (ICARM) and the Public Works Research Institute (PWRI) for allowing me to work as a research assistant and supporting me to smoothly carry out my study in Japan.

Table of Contents

Declaration	ii
Abstract	iii
Acknowledgement.....	v
Table of Contents.....	vii
List of Figures	viii
List of Tables.....	xiv
Chapter 1: Introduction.....	1
1.1 Background	1
1.2 Objectives.....	3
1.3 Contents	5
Chapter 2: Characteristics of the Sittaung River estuary	6
2.1 Introduction.....	6
2.2 Morphological characteristics	9
2.3 Hydrological characteristics and sediment sizes	21
2.4 Summary	34
Chapter 3: Numerical model for tidal currents and sediment transportation	35
3.1 Introduction.....	35
3.2 Governing equations	39
3.3 Formulas for erosion and deposition rates	40
3.4 Tests of validity for simulating tidal currents	45
3.5 Tests of validity for prediction of particle sizes distribution.....	51
3.6 Rule of channel bifurcation and lifetime of channels	54
3.7 Summary	56
Chapter 4: Numerical simulations on sand bar evolution, bank erosion and decadal periodicity of channel change.....	57
4.1 Introduction.....	57
4.2 Numerical simulation of sand bar evolution	57
4.3 Numerical simulation of bank erosion	79
4.4 Impact of spur dykes on estuary morphology	83
4.5 Sand bar formation processes with channel bifurcations	86
4.6 Summary	101
Chapter 5: Conclusion	103

List of Figures

Figure 2.1	The study area including Sittaung river, the estuary and the Gulf of Martaban	08
Figure 2.2	Landsat composite images obtained in (a) March, 1973, (b) February, 1989, (c) November, 2000, (d) December, 2006, (e) December, 2015 and (f) February, 2020 showing morphological change in the study area	11
Figure 2.3	Landsat composite images obtained in (a) January 13, 2002 and (b) December 15, 2002	12
Figure 2.4	Landsat images obtained in (a) February 01, 2003, (b) December 26, 2003 and (c) December 12, 2004	12
Figure 2.5	Landsat images obtained in (a) April 19, 2005, (b) April 06, 2006, (c) December 18, 2006, (d) January 03, 2007, (e) December 23, 2008 and (f) February 12, 2010	13
Figure 2.6	Landsat images obtained in (a) December 08, 2014, (b) May 30, 2015, (c) December 27, 2015, (d) January 12, 2016, (e) January 30, 2017 and (f) December 16, 2017	14
Figure 2.7	Landsat images obtained in (a) December, 2018, (b) April, 2019 and (c) February, 2020	15
Figure 2.8	Bank line change along west bank since 2007	16
Figure 2.9	Landsat 8 image on 14 th January, 2020. Bank lines on January, 2015 and April, 2017 are superimposed on the recent satellite image	17
Figure 2.10	(a) The stream channel near the bank line at Mamauk (the UAV camera focussing towards upstream), (b) The side slope of erodible bank composed of very fine (clay type) materials (picture taken before the tidal bore came), (c) After the passage of tidal bore, strong tidal currents take place causing severe bank erosion and (d) Occurrence of bank collapse owing to base erosion resulting from strong currents following the passage of bore front.	18
Figure 2.11a	Bank erosion process due to tidal currents	19
Figure 2.11b	Bank erosion process due to tidal currents	20
Figure 2.12	Data on monthly maximum discharge observed at Madauk from (a) 1991 to 2000 and (b) 2001 to 2010	21

Figure 2.13	Hydrographs specified at Madauk in recent years	22
Figure 2.14	Tidal water level (hourly) measured by University of Hawaii Sea Level Center (UHSLC) at Mawlamyine in 2019	22
Figure 2.15	Temporal change of water level observed at Mawlamyine during February, 2019	23
Figure 2.16	Survey sites in Sittaung river and estuary	24
Figure 2.17	(a) Propagation of tidal bore and (b) temporal change of water surface elevation after passage of bore	25
Figure 2.18	Locations of bed materials collected during first field survey in 2017 and their grain size distribution	26
Figure 2.19	Locations of bank materials collected during first field survey in 2017 and their grain size distribution	27
Figure 2.20	Locations of bed materials collected during second field survey in 2018 and their grain size distribution	28
Figure 2.21	Locations of bank materials collected during second field survey in 2018 and their grain size distribution	29
Figure 2.22	Locations of bed materials collected during second field survey in 2019 and their grain size distribution	29
Figure 2.23	Locations of bank materials collected during second field survey in 2019 and their grain size distribution	30
Figure 2.24	Summary of sediment particle sizes measured in the estuary	30
Figure 2.25	Sittaung river estuary for analysis of excess width and the ideal width	33
Figure 2.26	Analyzed results of Ideal as well as Excess width	34
Figure 3.1	Schematic diagram of flow velocity at bed load layer and erosion velocity	41
Figure 3.2	Control volume for mass conservation equation of very fine sediment	44
Figure 3.3	Specified locations for comparison of computed results and observed data	46
Figure 3.4	Computed and measured velocities at Alanbya	47

Figure 3.5	Computed and measured suspended sediment concentration at Alanbya	47
Figure 3.6	Comparison of computed results on water surface elevation at D (see Figure 4.1) with observed data	48
Figure 3.7	Computed water surface configurations for case 1	49
Figure 3.8	Temporal changes of computed water surface elevations at sites near Mamauk and comparison with observed data	49
Figure 3.9a	Tidal bore front captured using Unmanned Aerial Vehicle (UAV) during the field observation	50
Figure 3.9b	Computed velocity field reproducing the tidal bore near Mamauk	51
Figure 3.10	Computed size distribution curves of suspended sediment together with measured suspended and bed sediment	54
Figure 3.11	Schematic diagram for channel bifurcation and lifetime of channel	55
Figure 4.1	(a) The computation domain for computing bed evolution in the estuary, temporal change of (b) computed water surface elevation and (c) suspended sediment discharge at the downstream boundary The computation domain for	58
Figure 4.2	Cumulative volume of suspended sediment at different cross-sections	59
Figure 4.3	Ratio of bed load and suspended load at different cross-sections	60
Figure 4.4	Developing process of sand bars and stream channel pattern after computations of 5, 10, 15, 20, 25, 30, 35, 40 and 45 days for Case 3	61
Figure 4.4	Developing process of sand bars and stream channel pattern after computations of 30, 60 and 90 days for Case 3	62
Figure 4.5	(a) Computed stream channel pattern from Sittaung Bridge to Alanbya and (b) boat tracks (travel paths) during ebb tide	63
Figure 4.5	Computed water surface elevation at cross-section A-A' (shown in Figure 4.5a) near Alanbya (c) during ebb tide and (d) during flood tide	63

Figure 4.6	Velocity and the vectors at specified stages during (a) ebb tide and (b) flood tide for Case 3	64
Figure 4.7	(a) Spatial distribution of velocity at specified stage during flood tide and (b) lateral velocity profile and bed elevation across the cross-section P-P' for case 3	65
Figure 4.8	(a) Velocity distribution at one specified stage during ebb tide, (b) bed evolution for Case 3 and (c) Landsat 8 satellite image on April, 2019	66
Figure 4.9	Temporal changes in bed elevation along the longitudinal sections denoted by A-A' and B-B' for Case 3	66
Figure 4.10	Developing process of sand bars and stream channel pattern after computations of 20 days, 40 days, 70 days and 90 days for Case 4	67
Figure 4.11	Spatial distributions of velocity at specified stages during (a) ebb tide and (b) flood tide for Case 4	68
Figure 4.12	Locations of analysis of velocity at different points and cross-sections	69
Figure 4.13	(a) Location of cross-section A-A', lateral velocity profile and bed elevation at specified stages during (b) ebb tide and (c) flood tide for case 4	70
Figure 4.14	(a) Location of cross-section at B-B', lateral velocity profile and bed elevation at specified stages during (b) ebb tide and (c) flood tide for case 4	70
Figure 4.15	(a) Locations of points C and D; (b) Temporal change of velocity at Point C and (c) Temporal change of velocity at Point D for Case 4	71
Figure 4.16	(a) Spatial distribution of velocity at one specified stage during ebb tide, (b) bed evolution for Case 4 and (c) Landsat 8 satellite image on November, 2017	71
Figure 4.17	Computed cumulative volume of suspended sediment discharge at different cross-sections for case 4	72
Figure 4.18	Temporal changes of lateral bed profiles different cross-sections for case 4	73

Figure 4.19	Lateral distribution of unit discharge near Alanbya at specified stages of flood and ebb tides after 70 days for case 4	74
Figure 4.20	Downstream boundary employed as (a) constant amplitude and (b) varied amplitude	75
Figure 4.21	Temporal changes of suspended sediment discharge at different cross-sections	75
Figure 4.22	Temporal changes of suspended sediment discharge, velocity and water surface elevations at point A (see Figure 4.21)	76
Figure 4.23	Lateral distribution of unit discharge at different cross-sections	77
Figure 4.24	Daily discharge hydrograph from July to September in recent years	78
Figure 4.25	Bank line shift and bed elevation after computations of 4 days, 10 days, 18 days and 23 days	80
Figure 4.26	Change in bed elevation after computations of 4, 10 and 18 days with employment of bank erosion model	82
Figure 4.27	Spatial distribution of velocity at specified stages of (a) flood tide and (b) ebb tide with employment of bank erosion	83
Figure 4.28	Different sets of spur dykes employed to test their influences on bed morphology	84
Figure 4.29	Change in bed elevation after computations of 10 days for set 1, set 2 and set 3 spur dykes	84
Figure 4.30	Bed elevations at initial stage, after computations of 10 days for set 1, set 2 and set 3 of spur dykes	85
Figure 4.31	Changes in bed elevation after computation of 25 days for set 1, set 2 and set 3 spur dykes	86
Figure 4.32	Experimental channel (symmetric shape) to simulate channel bifurcations and lifetime of channels	87
Figure 4.33	Temporal changes of channel pattern for Case 1	88
Figure 4.34	Temporal changes of lateral bed profile at cross-section A-A' (Figure 4.33)	89

Figure 4.35	Suspended sediment discharge and its cumulated volume at different channels, A and B for Case 1	89
Figure 4.36	Temporal changes of channel pattern for Case 2	90
Figure 4.37	Suspended sediment discharge and its cumulated volume at different channels for Case 2	91
Figure 4.38	Experimental channel (asymmetric shape) to simulate decadal periodicity in a smaller scale	92
Figure 4.39	Developing process of channels with sand bars for Case 1 after computation of 10 days, 15 days, 20 days, 30 days, 50 days and 60 days	93
Figure 4.40	Temporal changes of cross-sectional shapes as well as of unit discharges at specified points for each channel	94
Figure 4.41	(a) Actual discharge hydrograph employed at upstream boundary and (b) corresponding measured tidal motion at Mawlamyine, employed as downstream boundary for Case 4	95
Figure 4.42	Specified cross-sections for investigating suspended sediment discharge and cumulative volume of suspended sediment discharge for Case 4	96
Figure 4.43	Temporal change of computed suspended sediment discharge at different cross-sections (see Figure 4.42) for Case 4	96
Figure 4.44	Temporal changes of cumulative volume of suspended sediment discharge at different cross-sections (see Figure 4.42) for Case 2	97
Figure 4.45	Developing process of channels with sand bars for Case 4 after computations of 3, 6, 15, 30, 45, 60, 75 and 84 days	98
Figure 4.46	Developing processes of channel pattern with sand bars after computations of 5, 10 and 15 days using the initial configuration shown in (a)	99
Figure 4.47	Comparison of the computed channel pattern with sand bars to recent satellite image	100
Figure 4.48	Spatial distribution of velocity during ebb tide at (a) initial stage and (b) after 15 days	101

List of Tables

Table 1	Calculation condition for tidal bore and associated tidal currents	45
Table 2	Calculation conditions for creation of bed morphology	58
Table 3	Computed and observed volume of supply discharge at upstream boundary	79
Table 4	Calculation conditions for symmetrical funnel shaped experimental domain	88
Table 5	Calculation conditions for asymmetrical funnel shaped experimental domain	92

Chapter 1: Introduction

1.1 Background

The Sittaung River drains an area of around 36000 km² to the estuary where flow discharge varies from around 500 m³/s during the dry season up to 5000 m³/s in the monsoon. The estuary stretches towards the Gulf of Martaban with a funnel shape to the south. Due to such a shape, a bore front followed by strong tidal currents takes place. The bed and banks of the estuary are composed of very fine particles with median diameter ranging 0.02 to 0.04 mm. Strong tidal currents cause very active sediment transportation, sand bar deformation and corresponding channel changes leading to severe bank erosion at a rate of around 1 km every year in most active areas.

Stuart (1932) observed a tidal bore in March- 1931 and made a brief discussion on its type. He explains that ‘the famous bore of the Sittaung is due to the shallow, funnel-shaped estuary, which is particularly adapted to its formation. The intensity of the bore seems to vary periodically, possibly owing to changes in the sandbanks at the mouth of the river; the bore was very high about 1924-25, but has decreased since then. It is found to attain its maximum intensity of the year during the spring tides in February and March, when the tidal range is large; the sudden tidal wave may then be 5.5 feet high, and has been known to attain the height in 2 minutes. The bore attains the same height in July, August, September and October, but rises more slowly, owing to the action of flood-water coming down the river. The bore gives warning of its approach by a distinct roaring noise; in the deep channel on the west it appeared as a sudden series of swells without any waves breaking, but in the shallow channel on the east it was a racing, breaking wave followed

by two or three more breaking waves. Along the shore it rose to a height of about 5 to 6 feet, but in the center of the channel the height was estimated at not more than 4 feet’.

Analysis of previous literature and maps show that the physical setting of the Sittaung River estuary is nearly undisturbed, free from major human intervention and the estuary is rich with huge natural resources of migratory birds on the tidal mudflats, fish in the Gulf of Martaban and agricultural land on both banks of the estuary. However, the area was found highly susceptible to changes according to Landsat satellite images acquired since 1973 and investigated to check the morphological characteristics of the study area. The satellite image analysis revealed that the area is very much changeable due to dramatic variability in flow pattern, movement of sand bars and severe bank erosion. Analysis of bank line shifts also found that the bank line retreated more than 10 km along the west bank during the last 10 years. It is inevitable that such severe bank erosion brings about immense stress on socio-economic structures: for example, destruction of villages, loss of cultivable lands and disruption of communication facilities.

To understand physical characteristics precisely and check the actual scenario, detailed field investigations were conducted. The investigations included observation and measurement of the flow pattern of tidal bores and associated tidal currents, investigation of sediment particle sizes of bed and bank materials, measurement of representative cross-sections along the Sittaung River and also at some locations in the estuary. In addition, historical hydrological information was also collected and analyzed as a part of the baseline study. The occurrence and subsequent consequences of severe disasters motivated me to study the phenomena, identify the reasons behind such a severe problem and try to provide technical solutions as well as policy level input.

1.2 Objectives

Many researchers studied tidal bore with mathematical expressions since the last century. A tidal bore is a positive surge that may form at flood tide in shallow estuaries with a large tidal range (Bazin, 1865; Tricker, 1965; Lynch, 1982; Chanson, 1999, 2001; Simpson et al., 2004, Wolanski et al., 2004). Tidal bore dynamics have been studied based on numerical simulation by several researchers (Bonneton et al., 2015; Yu et al., 2012; Pan et al., 2007; Madsen et al., 2004 and Wolanski et al., 2004). Riddler (2017) simulated the propagation of a tidal bore in the Sittaung River estuary using a flow model but did not discuss the relation between tidal currents and sediment transportation.

Several studies have been conducted based on sediment transportation in the Gulf of Martaban (Liu et al., 2020; Matamin et al., 2015; Hedley et al., 2010; Robinson et al., 2007; Rao et al., 2005; Ramaswamy et al., 2004;). Shimozono et al. (2019) ‘explored morphological changes in the study area and identified an auto-cyclic process in a sedimentary system driving large scale channel migration in decadal to multi-decadal cycles’. These studies discuss sediment transportation and the geo-morphological characteristics of the Gulf of Martaban as a whole, but do not put particular attention to the tidal bores, associated tidal currents, sediment transport and bank erosion in estuaries.

There are many modelling systems available worldwide, each one with its own approach for a proper description of cohesive sediment dynamics. Among them, well-known systems are Delft3D (DELTAWARE, 2016), Telemac-Mascaret (TELEMAC-MASCARET, 2016), MIKE (DHI, 2016), SisBaHia and COPPE/EFJR, (Peixoto et al., 2017). In addition, the International River Interface Cooperative (iRIC) is proposed for

modeling flow, sediment transport and morpho-dynamics in rivers and other geophysical flows (Nelson et al., 2016).

In the sediment transport scheme, the upward flux of suspended sediment from the river bed is evaluated using Itakura and Kishi's formula (Itakura & Kishi, 1980). Garcia & Parker (1991) analyzed seven sets of formulas available in the literature for predicting the entrainment of uniform sediment into suspension and proposed the empirical fit which would provide reasonable estimates of the sediment entrainment coefficient for sediment particles whose sizes range from 0.0625 mm to 0.50 mm (Einstein, 1950; Engelund and Fredsoe, 1976; Smith and McLean, 1977; Itakura & Kishi, 1980; Van Rijn, 1984; Celik and Rodi, 1984; Akiyama and Fukushima, 1986). While checking existing methods for treating suspended sediment, it was clear that transport of fine particles available in the study area cannot be treated using existing formulas. All other methods actually over-estimates sediment concentration in the water layer.

In this study, numerical simulations were conducted to reproduce tidal bores, associated tidal currents and bed morphology in the study area using two-dimensional depth-averaged Reynolds' equation and a sediment transport model. In the sediment transport process model, a new scheme was proposed to treat sediment transportation and associated channel changes in the bed composed of fine materials. Using the proposed model, stream channel patterns and sand bar evolution were reproduced and compared with satellite images. Moreover, a bank erosion model was employed to test the model capability in reproducing bank erosion in the target area. Experimental channels were employed to simulate channel bifurcations, lifetime of channels and long term morphological change.

1.3 Contents

Chapter 2 describes morphological and hydrological characteristics based on analysis of satellite images, data collected during field investigations and from secondary sources. Changes in channel pattern, migration of sand bars and severity of bank erosion are analyzed using satellite images. The characteristics of tidal bores, associated tidal currents and particle sizes of bed and bank materials are identified through analysis of hydrological information and field data.

The numerical model employed for analysis of tidal currents and associated sediment transportation is discussed in Chapter 3. As the study area consists of very fine sediment particles with median grain sizes ranging 0.02 to 0.04 mm, classic methods of sediment transport cannot treat the transport of such fine materials. For this reason, a new method is proposed to evaluate the erosion rate of bed sediment composed of such fine materials. Using the proposed treatment, a numerical model is validated and the particle size distribution of suspended sediment is predicted well.

In Chapter 4, numerical results of channel patterns, bed evolution and the characteristics of sediment transport are described. In addition, comparison of the created morphology with available satellite images are shown. A bank erosion model is employed and computed results are discussed. The effect of spur dykes as structural countermeasures to erosion is tested for channel and sand bar control. Numerical results on channel bifurcations, periodicity of channel change and lifetime of a channel are discussed. Chapter 5 wraps up the discussion and discusses the probable contribution of this study for the prediction of channel change, sand bar deformation, identification of vulnerable locations for bank erosion and possible hard and soft countermeasures to combat such severe sediment-induced natural disasters.

Chapter 2: Characteristics of the Sittaung River estuary

2.1 Introduction

Yamashita and Aung (2016) described the 'Sittaung River (also spelled as Sittang or Sittoung) generates originally at the edge of the Shan Plateau, southeast of Mandalay Region (20°31' N and 96°18' E) and then flows southward through Bago Region until it enters into the Gulf of Martaban. The total river length is 420 km. It flows through flat areas between the forested Bago Mountains on the west and the steep Shan Plateau on the east. The river is contributed by 22 major streams and the total watershed area is 330,350 km².

The Sittaung River, the estuary and the Gulf of Martaban are shown in Figure 2.1. Due to the shallow depth and the funnel shape, tidal bores and associated strong tidal currents take place during spring tides on the new moon and the full moon. Such strong currents cause bed variation and corresponding channel shifting leading to severe bank erosion. 'Loss of land for agriculture and settlements due to bank erosion has made a significant impact on the livelihood of local people' (ICHARM Newsletter, April 2019, Volume 14). The dominance of very fine particles in bed and bank materials and the influence of strong tidal currents increase the erodibility and transportability of fine particles in the estuary area.

Tidal bores in different parts of the world have been studied by many researchers since decades ago. Tidal bores are defined and classified in many studies (Tricker, 1965; Lynch, 1982; Rowbotham, 1983; Bartsch-Winkler and Lynch, 1988; Chanson, 1999, 2001, 2012; Savenije, 2005; Lin, 2008; Freidrichs, 2010). The depths and cross-sectional

area of tidal channels are discussed in some recent studies (Lauven et al., 2018; R. C. Steijn et al., 2019). R. C. Steijn et al. (2019) made a brief discussion on the Sittaung River estuary. They analyzed the rates of coastal erosion, studied cases of extreme dynamics and proposed adaptation strategies. The only estuary with comparable extreme rates of channel migration, tidal bore formation and fine sediment transport the Qiantang estuary in PR China on the coast of the East China Sea (Xie et al., 2018; Chen et al., 1990).

Riddler (2017) visited the Sittaung River twice. During the second trip, depth measurements were carried out. The boat could only sail the deeper parts of the river. Thus, it was not possible to obtain a complete cross-section. Shimozono et al. (2019) ‘explored morphological changes of the study area which has great morphological dynamism from extreme tidal energy and large sediment inputs, through field surveys and satellite imagery analysis’. They identified ‘an auto-cyclic process in a sedimentary system driving large-scale channel migration in decadal to multi-decadal cycles’.

As the Sittaung River runs up to the Gulf of Martaban, studies have also been conducted regarding tidal currents and sediment transport characteristics in the (Ramaswamy et al., 2004; Rao et al., 2005; Robinson et al., 2007; Hedley et al., 2010; Matamin et al., 2015). On a recent study, Liu et al. (2020) discussed sediment budget and mass balance in the Gulf of Martaban and explained interesting phenomena of seasonal variation in spatial distribution of sediment in the Gulf. The Virginia Institute of Marine Science is focusing on understanding mass balances and sediment budgets in relation to sea-level change in the Gulf and anticipates that the fate of the Irawaddy-Salween delta depends on geology, sea-level rise, sediment starvation, or most likely a combination of all these factors.

In light of the above studies conducted on the study area, this chapter describes morphological characteristics using historical satellite images, hydrological characteristics including tidal currents, historical discharge information, tidal range and seasonal variations and data collected in field investigations.

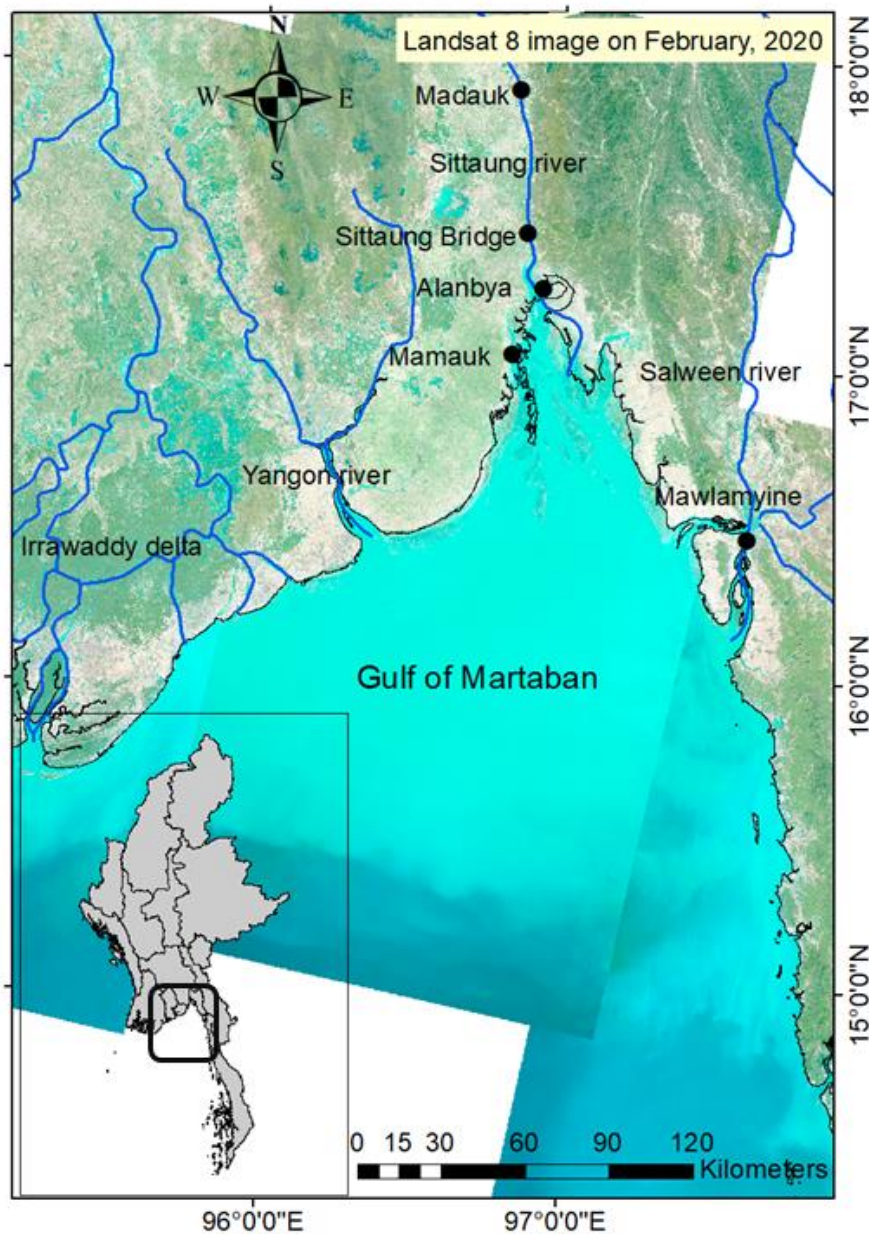


Figure 2.1 The study area including Sittaung river, the estuary and the Gulf of Martaban

2.2 Morphological characteristics

Figure 2.1 illustrates the locations of discharge and water-level measurement stations, places of field investigations, locations vulnerable to bank erosion and the overall geomorphological set-up to the Situang River, the estuary and the Gulf.

There is a discharge measurement station at Madauk which is maintained by the Department of Meteorology and Hydrology, Myanmar. The location is $17^{\circ}55'0.012''$ N and $96^{\circ}50'60''$ E. Historical discharge information since 1987 was acquired to check yearly flow along Sittaung river. There are 3 major bridges across Sittaung river, from the upstream, the first one near Taungoo, the next one near Madauk and the last one near Sittaung old town. The location of the bridge is $17^{\circ}27'7.848''$ N and $96^{\circ}52'33.24''$ E.

Alanbya village is the most affected area due to severe bank erosion in recent years. Especially from 2002 to 2006, due to very active channel change and bank erosion, this village area disappeared from the map. The location is $17^{\circ}16'22.62''$ N and $96^{\circ}55'47.208''$ E. Since 2010, the bank line was retreated more than 10 km near Mamauk. For this reason, Mamauk is a strategically important location for observation of tidal bores and bank erosion. In the very recent past, for example, in 2019, Mamauk disappeared from the map. The location of Mamauk is $17^{\circ}3'48.168''$ N and $96^{\circ}49'52.572''$ E.

Mawlamyine is situated at the outfall of the Salween River which is at $16^{\circ}27'54''$ N and $97^{\circ}37'19.2''$ E. The University of Hawaii Sea Level Center (UHSLC) measures tidal water levels at this location. The Gulf of Martaban is located at northern Andaman Sea and roughly covers the latitude range from 15° N to 18° N and the longitude range from 95° E to 97.5° E. It is a tide-dominated bay with variable tidal ranges. 'The dominant tide in this area is semi-diurnal with M2 and S2 components' (Sindhu and Unnicrishnan, 2013). 'Along the Ayeyarwady delta, the highest tidal range of 7 m is found at Elephant

point, while the Ayeyarwady river mouth is characterized as meso-tidal with a range between 2 and 4 m' (Ramaswamy et al., 2004).

'Due to long-term accumulation of high sediment fluxes from the Ayeyarwady and Salween rivers since the late Miocene, the northern part of the Andaman Sea (i.e. the Gulf of Martaban) is much shallower' (Morley, 2013, Liu et al., 2020). 'Due to high sediment discharge from adjacent rivers, the prevailing monsoonal winds, strong wave, tidal currents and shallow water depth, the Gulf of Martaban experiences suspended sediment concentrations up to 500 mg/liter, making it one of the world's largest high turbidity zones' (Ramaswamy et al., 2004, Liu et al., 2020). 'Remote sensing data reveals a near homogeneous surface suspended sediment concentration turbid water covering the entire Gulf of Martaban during the north-east monsoon season' (Liu et al., 2020).

Photo analyses were conducted to grasp morphological changes, such as channel pattern changes and bank line shifting in the estuary. Figure 2.2a-f shows historical morphological changes through analysis of Landsat 5 and Landsat 8 satellite images from 1973 to the present. The locations of Sittaung Bridge, Alanbya village as well as Mamauk are illustrated to show how active bank erosion and subsequent channel changes take place. From 1973 to 1989, bank erosion occurred westwards and the Mamauk area was severely affected as shown in Figure 2.2a,b. From 1989 to 2000, main channel shifted eastwards causing erosion along the left bank as shown in Figure 2.2b,c. The eastward erosion continued till 2006 and Alanbya disappeared from the map during this time period as seen in Figure 2.2c,d. Figure 2.2e,f shows the Mamauk area facing erosion tendency again after 1989 and it is already disappeared before February, 2020.

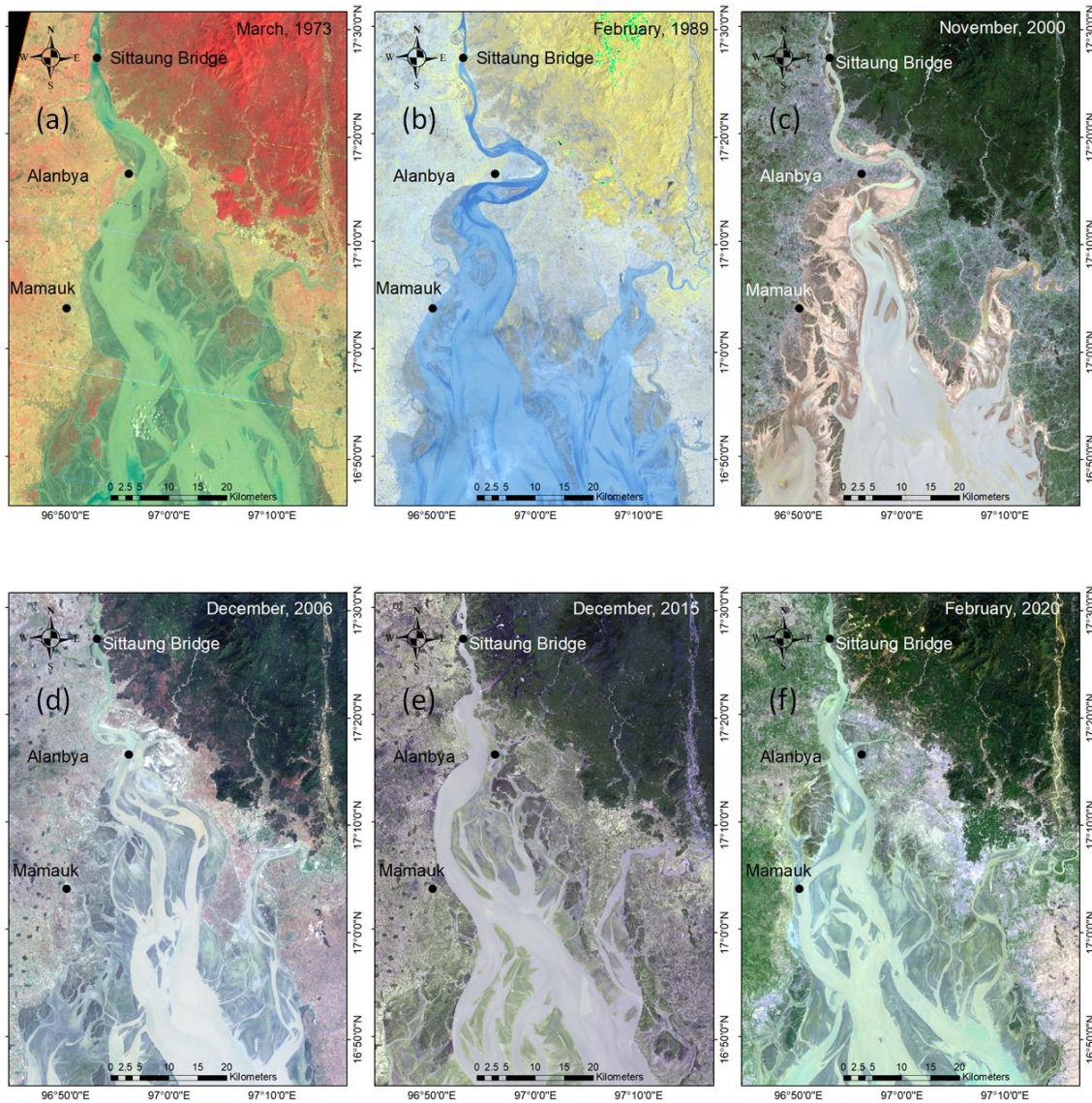


Figure 2.2 Landsat composite images obtained in (a) March, 1973, (b) February, 1989, (c) November, 2000, (d) December, 2006, (e) December, 2015 and (f) February, 2020 showing morphological change in the study area

The spatial and temporal movements of sand bars and stream channels are described precisely year-by-year. Figure 2.3 shows temporal changes from January to December, 2002. During this time, a major shift in the main channel course occurred near Alanbya village accelerating erosion leading to the disappearance of the village in later years. Moreover, near Mamauk, two major channels merged into a single channel flowing

eastwards which became the cause of severe erosion eastwards in the next couple of years. However, during the decade from 2000 to 2010, Mamauk was out of danger more than 10 km far away from the main channel.

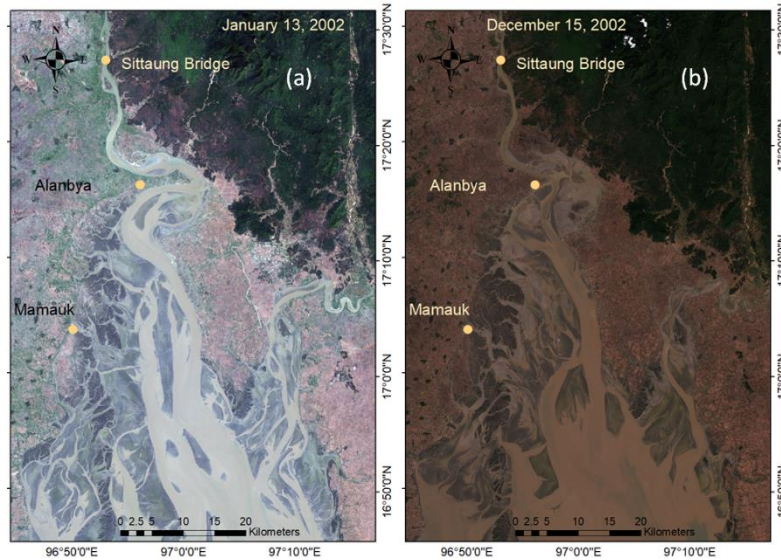


Figure 2.3 Landsat composite images obtained in (a) January 13, 2002 and (b) December 15, 2002

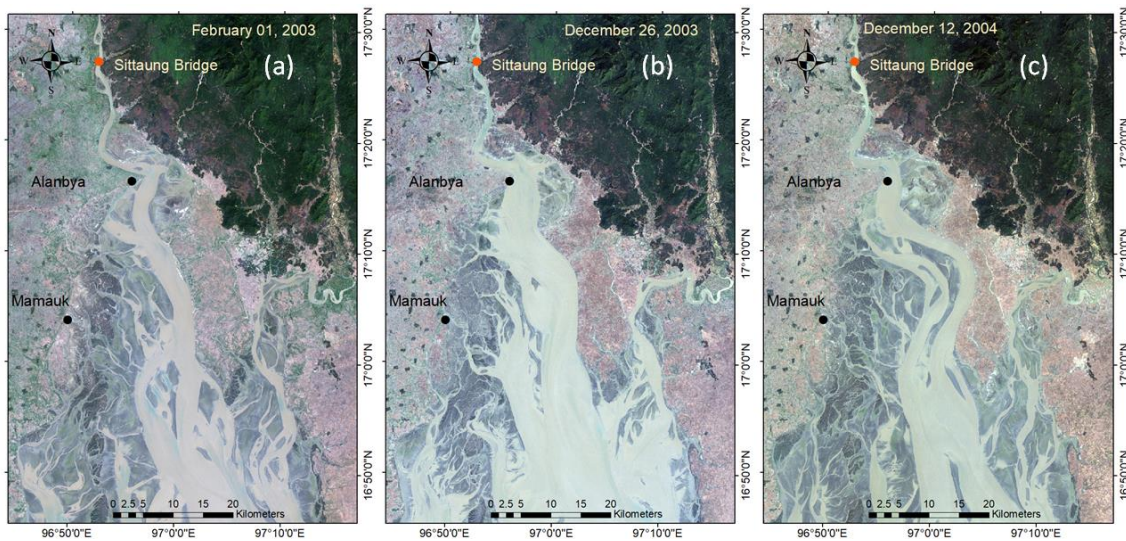


Figure 2.4 Landsat images obtained in (a) February 01, 2003, (b) December 26, 2003 and (c) December 12, 2004

Figure 2.4 illustrates satellite images acquired in February and December 2003 and December in 2004. These images show that Alanbya had already disappeared because of

erosion resulting from the shifting of the main channel. In addition, the eastward erosion was much more dominant and the bank line took a concave shape after the lateral bank line retreated considerably. Generation of sand bars in the middle of the channel was also observed after the occurrence of eastward bank erosion.

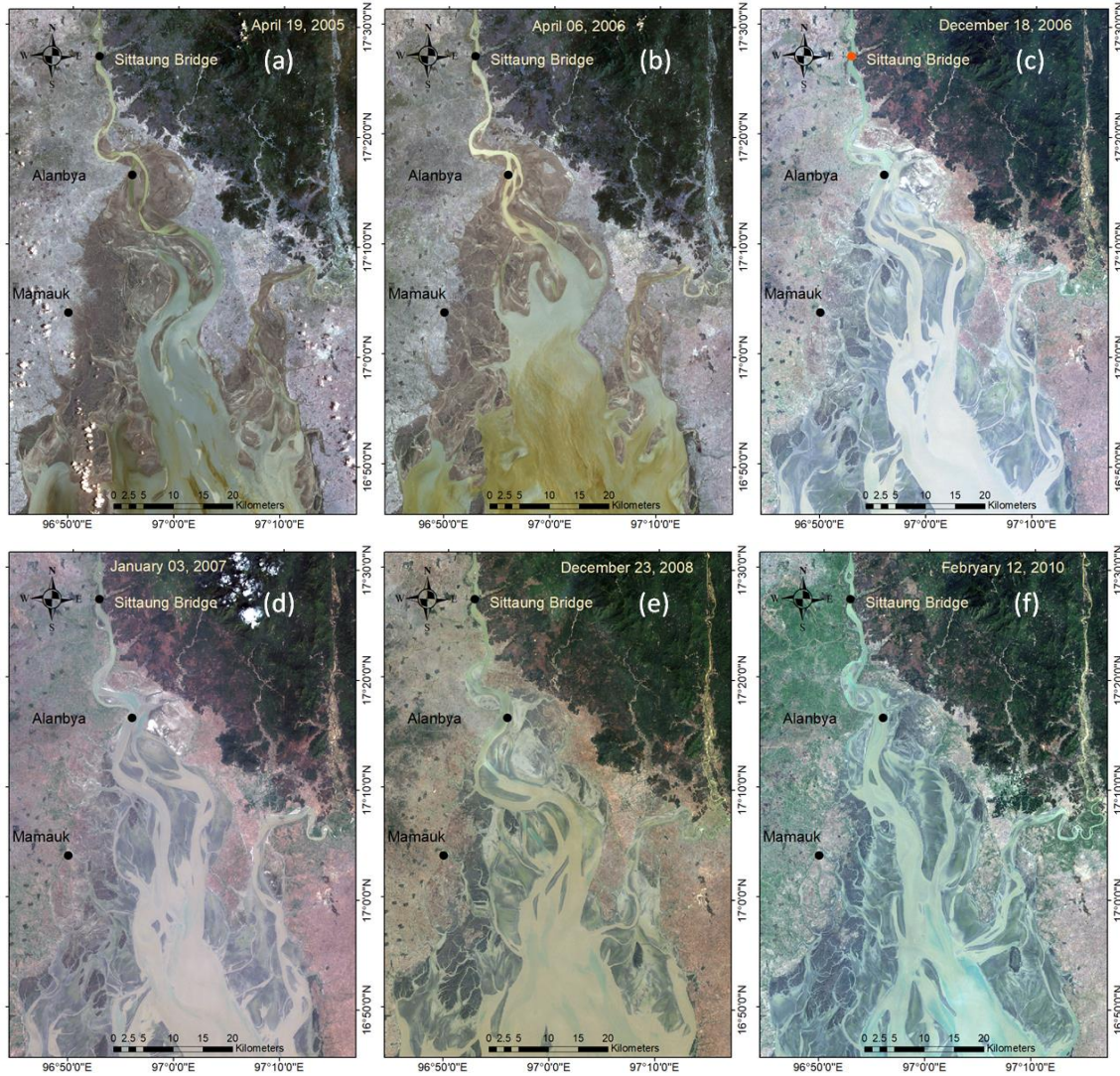


Figure 2.5 Landsat images obtained in (a) April 19, 2005, (b) April 06, 2006, (c) December 18, 2006, (d) January 03, 2007, (e) December 23, 2008 and (f) February 12, 2010

In the later years, erosion hitting the eastern bank became severe and then channel shifting nature stopped such an erodible tendency, too. Figure 2.5 illustrates temporal changes in channel pattern and sand bar locations with bank lines from April- 2005 to

April- 2010. From 2005 to 2007, the rigorous bank erosion continued eastwards and sand bars with a wide variety of shapes were observed in the middle of the main channel during this time period. However the erosion along the left bank came to a halt in 2008 and the main channel straightened during 2010 bringing the left bank erosion to a complete stop.

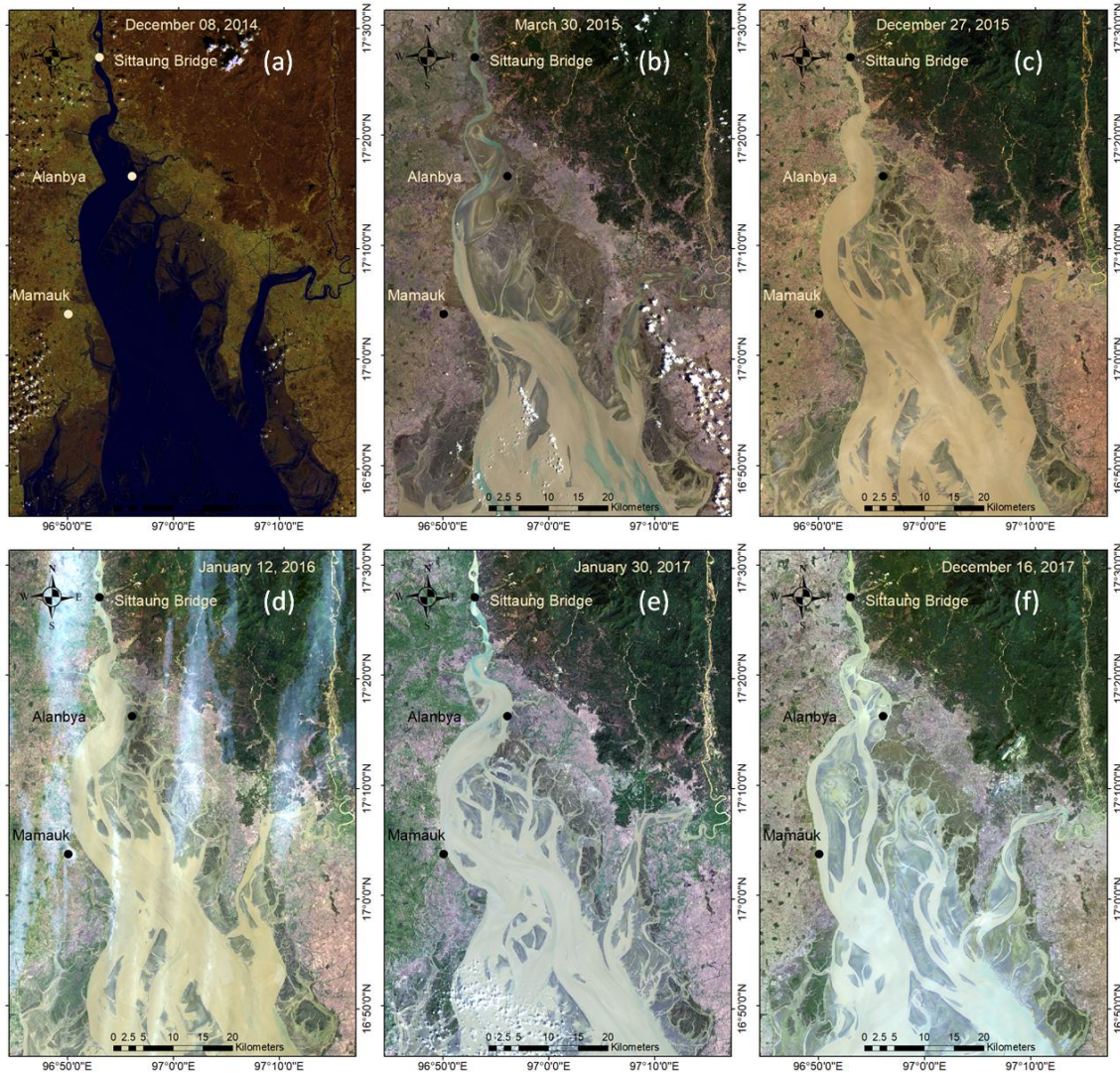


Figure 2.6 Landsat images obtained in (a) December 08, 2014, (b) May 30, 2015, (c) December 27, 2015, (d) January 12, 2016, (e) January 30, 2017 and (f) December 16, 2017

Radical change in bank erosion tendency was observed during the next decade, i.e. from 2010 to 2020. During this decade, the main channel started flowing westwards and corresponding westward bank line retreat was also observed during this time period.

The location of Alanbya was once at the right bank of the channel. However the main channel started flowing westwards and the village is now located at the left bank. In addition, the bank line approached toward Mamauk at a rate of around 1 km every year. Figure 2.6 illustrates main channel, sand bars and bank lines from 2014 to 2017. During these years, the main channel flowed attacking the right bank and bank lines near Mamauk faced severe erosion. A major change in the main flow channel was observed after the monsoon in 2017. The main channel bifurcated into two different channels and Mamauk suffered from bank erosion.

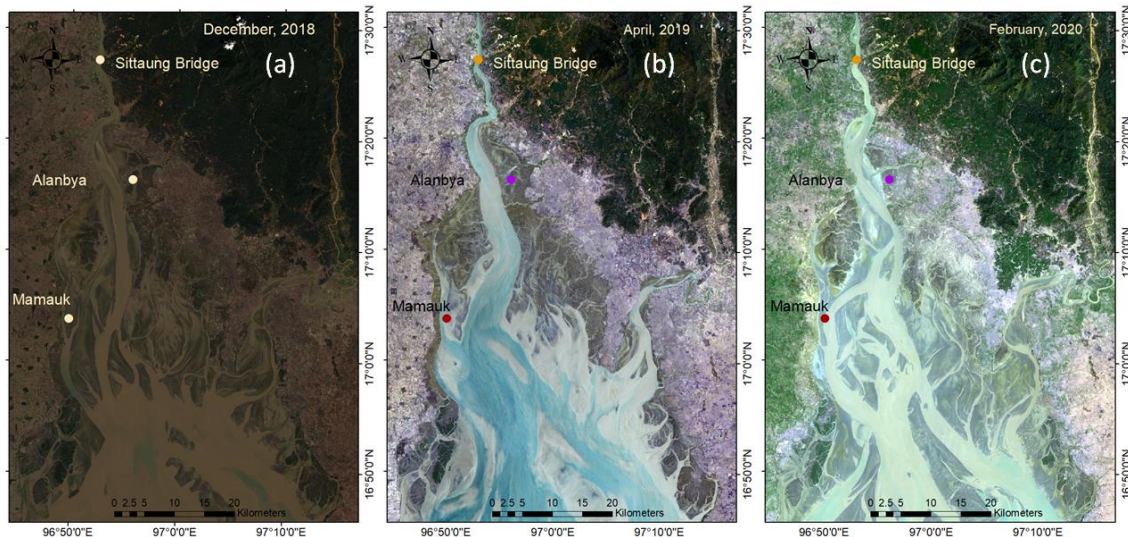


Figure 2.7 Landsat images obtained in (a) December, 2018, (b) April, 2019 and (c) February, 2020

Erosion along the right bank stopped in recent years. The main channel straightened and considerable deposition occurred near the west bank. Such changes in the channel and sand bar geometry has been observed since 2018 and satellite images are illustrated in Figure 2.7. The tendency of bank erosion along the left bank, though on a small scale till now is observed in Figure 2.7c. The analysis of the bank line images proves the periodicity of bank line change at a decadal to multi-decadal time-scale.

Figure 2.8 shows the bank line of the estuary identified in 2007, 2016, 2017 and 2018 by means of radar image analysis (ALOS-2). The result shows that ‘bank erosion takes place very actively and bank line retreats over 10 km at most active locations in latest ten years’ (Ahmed et al., 2019).

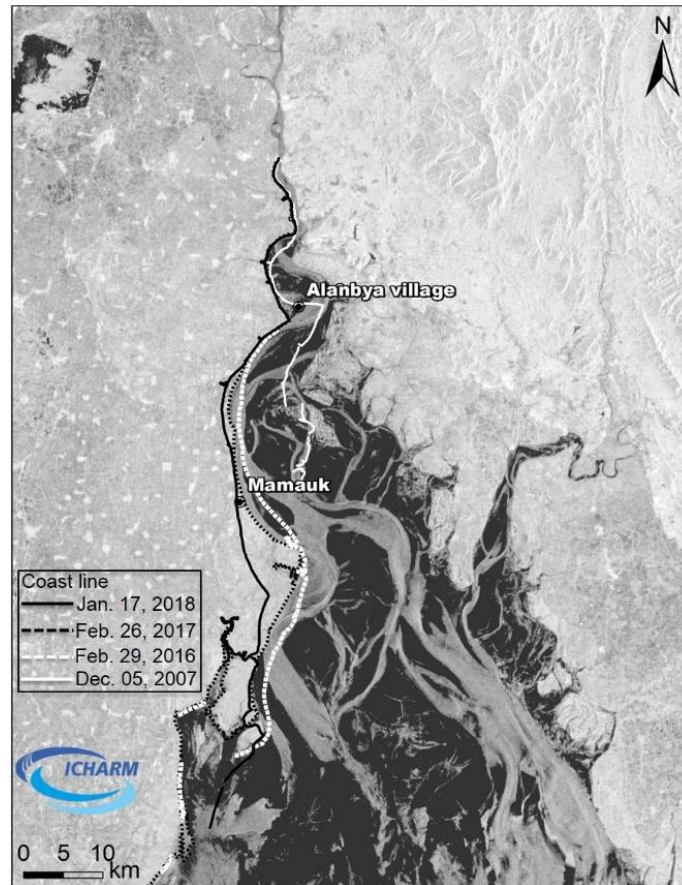


Figure 2.8 Bank line change along west bank since 2007

Figure 2.9 shows Landsat 8 composite satellite images on January 14, 2020. The locations of Sittuang Bridge, Alanbya village and Mamauk are also illustrated. The bank lines in January- 2015 (red colored lines) and April- 2017 (black colored lines) extracted from Landsat composite raster images are superimposed on a recent bank line image in January- 2020. It is clear that very severe bank line retreated significantly was occurred in recent years and Mamauk disappeared due to the bank line shifting.

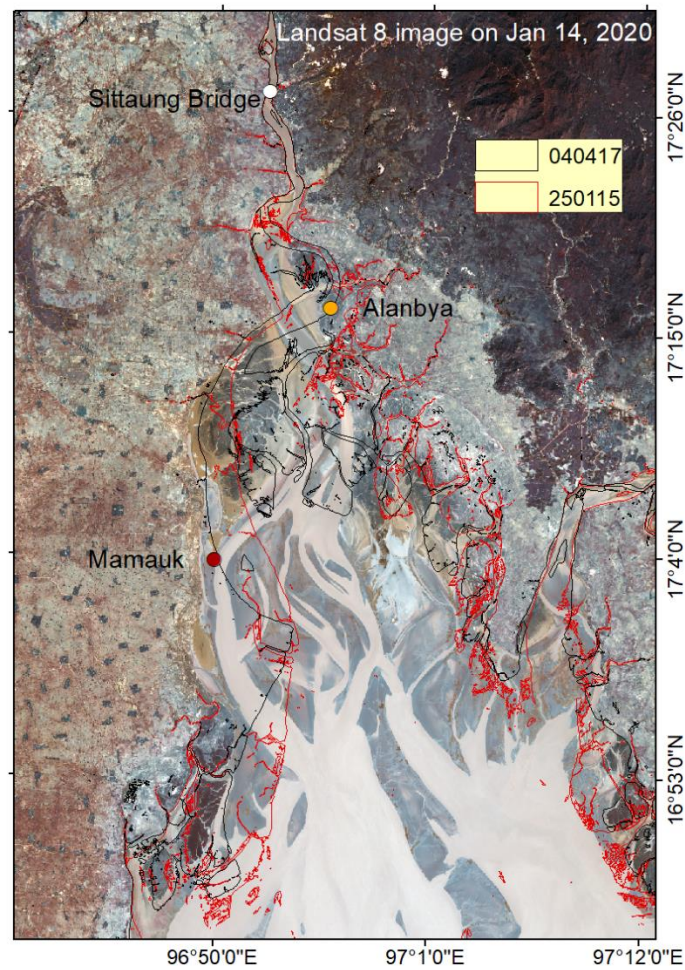


Figure 2.9 Landsat 8 image on 14th January, 2020. Bank lines on January, 2015 and April, 2017 are superimposed on the recent satellite image

Such severe bank erosion was experienced physically on February 16, 2018 at Mamauk which is one of the active bank erosion areas. The main purpose was to investigate how the bank erosion takes place as well as to infer parameters associated with the bank erosion. At the site, observations were performed by means of eye-inspections and an Unmanned Aerial Vehicle (UAV) to investigate the behavior of the bore front, tidal currents following the passage of the bore front and the process of bank erosion. The bore front reached the observation site at 14:40 on February 16, 2018. Immediately after the passage of the bore front, strong currents were formed for about 2

hours; the maximum current was estimated to be 4–5 m/s at 15:15 in and area 20–30 m apart from the bank, and the water surface velocities were 2.15 m/s at a location 10 m apart from the bank and 1.46–1.53 m/s near the bank according to the measurements by means of floating matters.



Figure 2.10 (a) The stream channel near the bank line at Mamauk (the UAV camera focussing towards upstream), (b) The side slope of erodible bank composed of very fine (clay type) materials (picture taken before the tidal bore came), (c) After the passage of tidal bore, strong tidal currents take place causing severe bank erosion and (d) Occurrence of bank collapse owing to base erosion resulting from strong currents following the passage of bore front

Figure 2.10 illustrates some representative photos of the banks near Mamauk which were taken during the field investigations before and after the propagation of a tidal bore. Figure 2.10a shows a stream channel flowing just adjacent to the bank line near Mamauk. The photo is taken using UAV focusing on the upstream side. The

irregularity in the bank line on the left and very shallow sand bars on the right are clearly visible. Figure 2.10b shows the close-up view of the bank slope which shows the abundance of silty clay and clay type particles as bank materials. Figure 2.10c illustrates strong tidal currents hitting the banks. The abrupt shape of the bank shows rigorous bank erosion. Figure 2.10d shows a bank feature in which a bank is about to collapse. Such a bank collapse is considered to take place continuously in time and space.

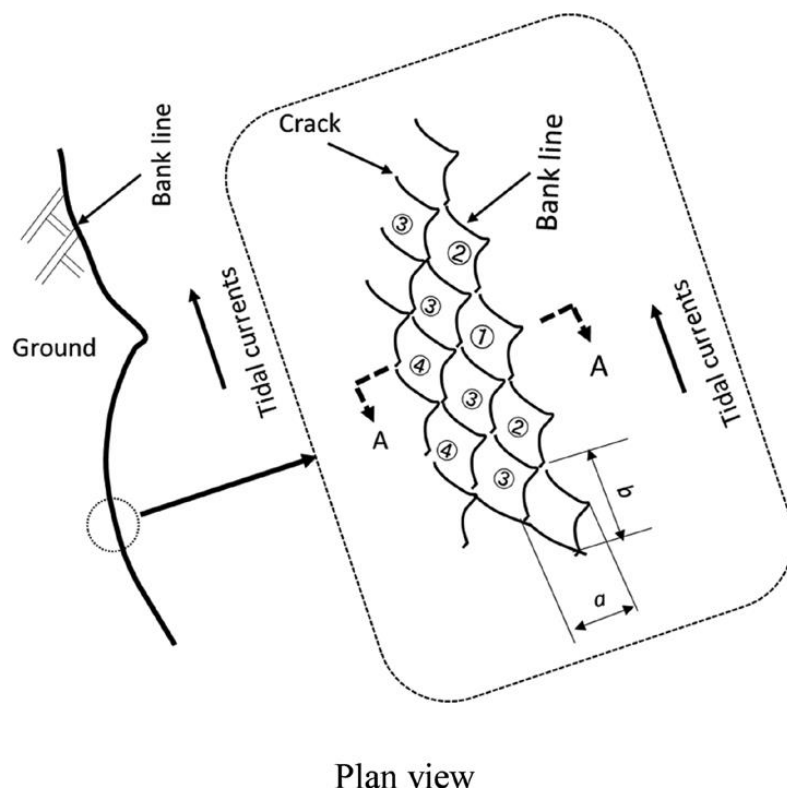


Figure 2.11a Bank erosion process due to tidal currents

Figures 2.11a,b illustrate a possible bank erosion process resulting from our observation and experiences associated with sediment transportation. Many crack lines appear in the ground surface before causing bank collapses and then, bank collapses take place in various places. Such collapses constitute a cycle of collapses. As shown in Figure 2.11a, the soil block designated by slides or rotates down first, then the block follows and

vice versa, owing to erosion of its base. Then, the block is exposed to currents, and it slides or falls rotationally due to the erosion of its base, resulting in exposure of block, which is one cycle of bank erosion.

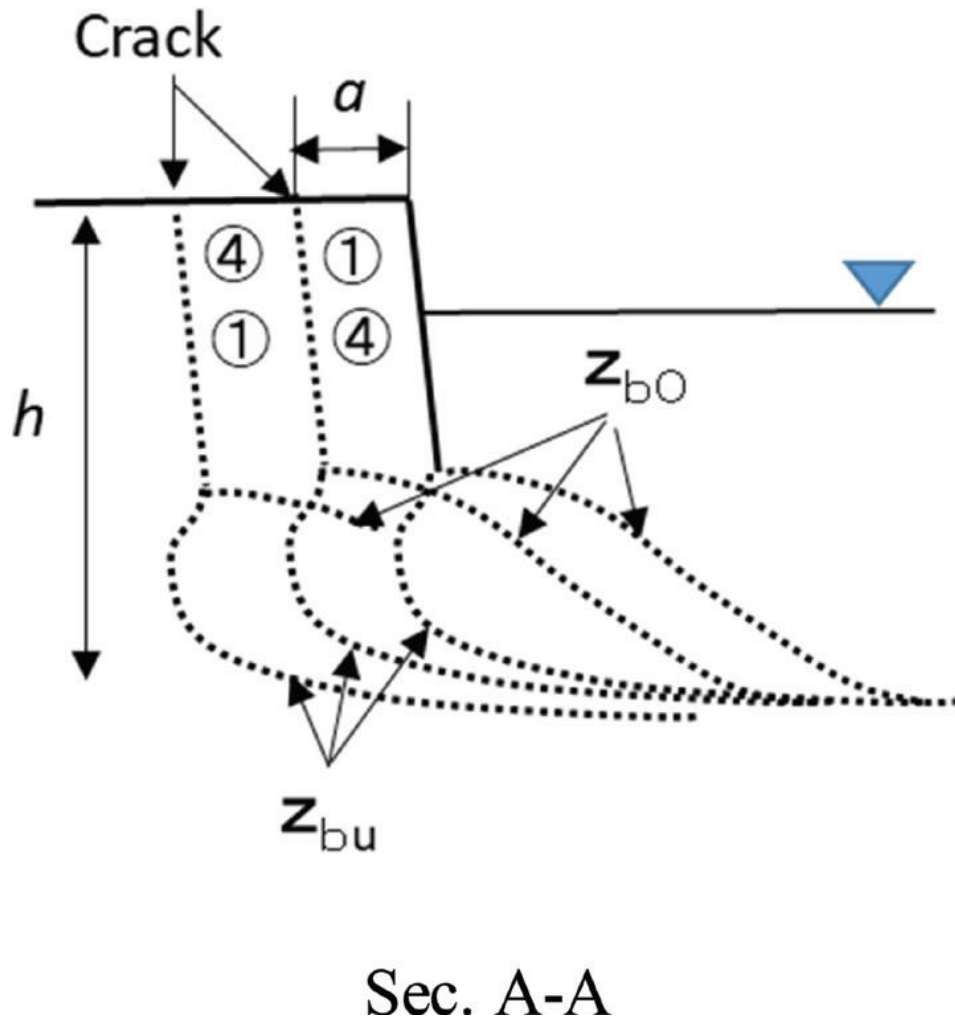


Figure 2.11b Bank erosion process due to tidal currents

The cross-sectional erosion process is illustrated in Figure 2.11b. Just after the bank collapses, the soil block released from the collapse deposits to its base and it forms the bed illustrated by z_{b0} . When the bed sediment is eroded to an unstable bed boundary designated by z_{bu} , the next bank collapse illustrated by the block or will take place. This is also one cycle in cross sectional change.

2.3 Hydrological characteristics and sediment sizes

Figure 2.12a,b show monthly maximum discharge along the Sittaung River at Madauk from 1991 to 2010 and Figure 2.13 illustrates discharge information in recent years. ‘There are 20 flood events with peak flow discharge over 4000 m³/s, 4 events over 4500 m³/s and no event over 5000 m³/s in latest 30 years’ (Ahmed et al., 2019). In the dry season, from January to May, the discharge remains around or less than 500 m³/s, whereas in the monsoon, the average flood discharge remains around 3000 m³/s.

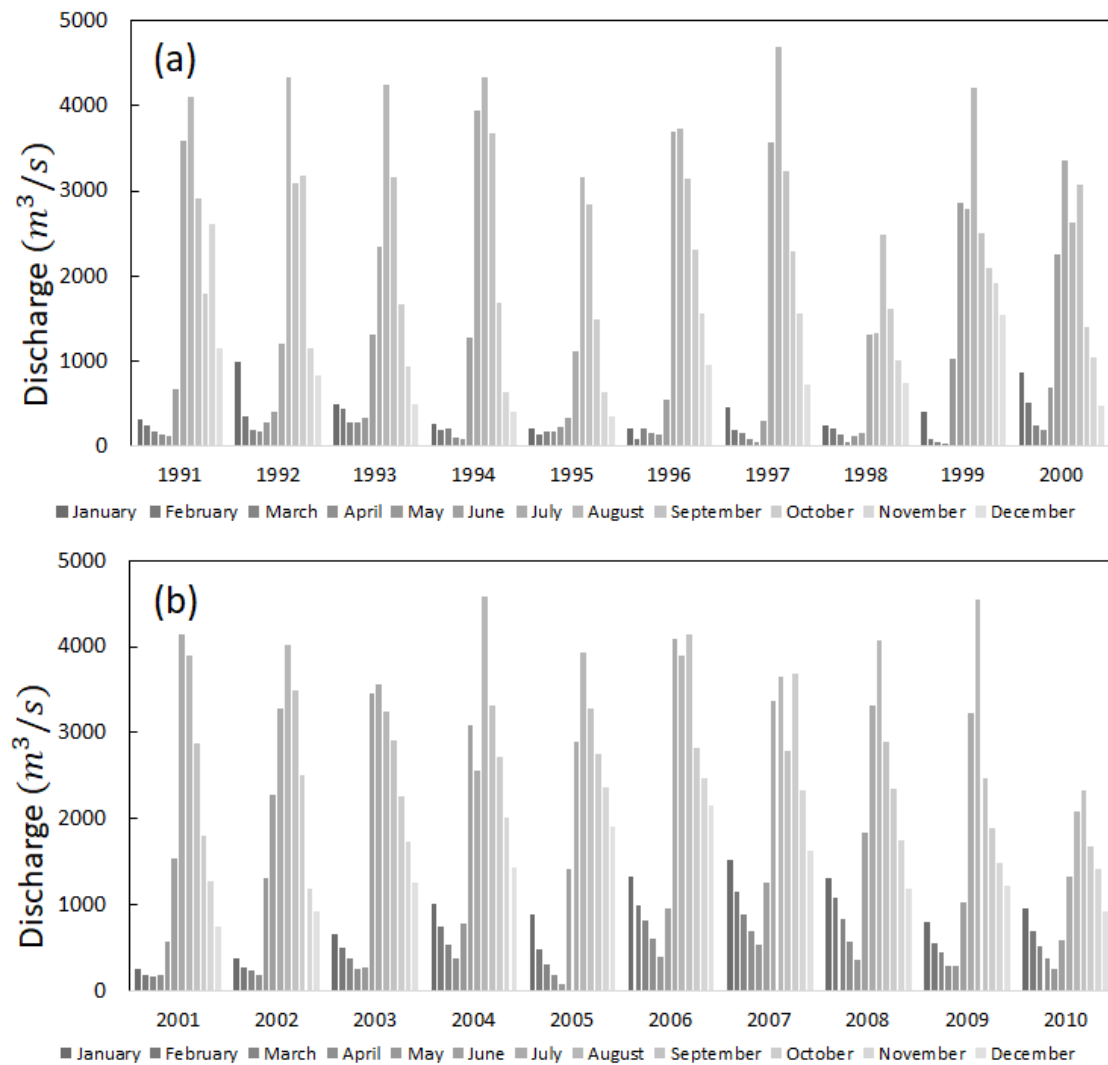


Figure 2.12 Data on monthly maximum discharge observed at Madauk from (a) 1991 to 2000 and (b) 2001 to 2010

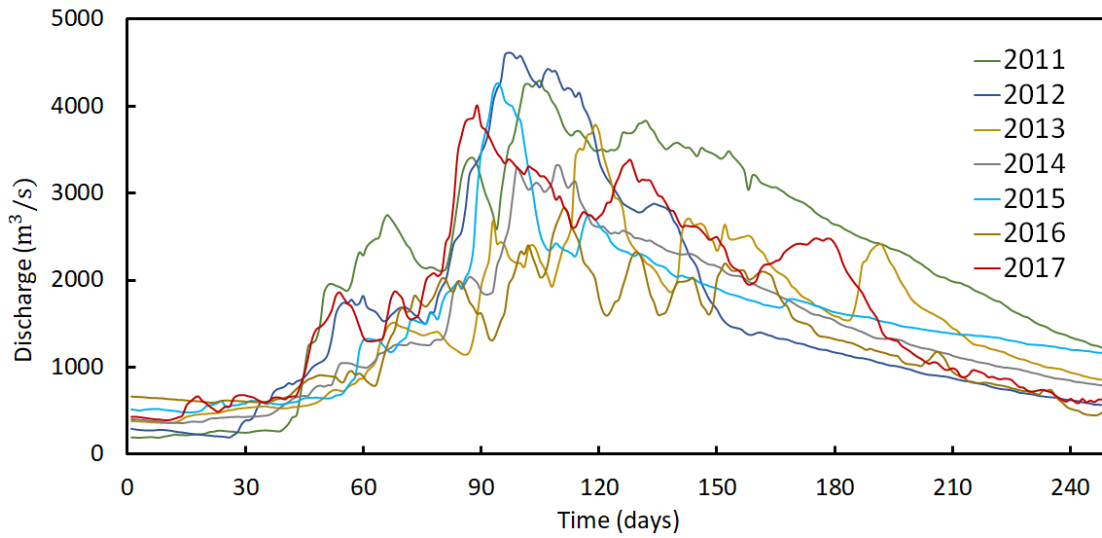


Figure 2.13 Hydrographs specified at Madauk in recent years

Tidal ranges in the Gulf of Martaban are summarized by Ramaswamy et al. (2004). Tidal water-level data at Mawlamyine in recent years were collected from the University of Hawaii Sea Level Centre (UHSLC) website. Figure 2.14 shows hourly tidal water-level data collected in 2019.

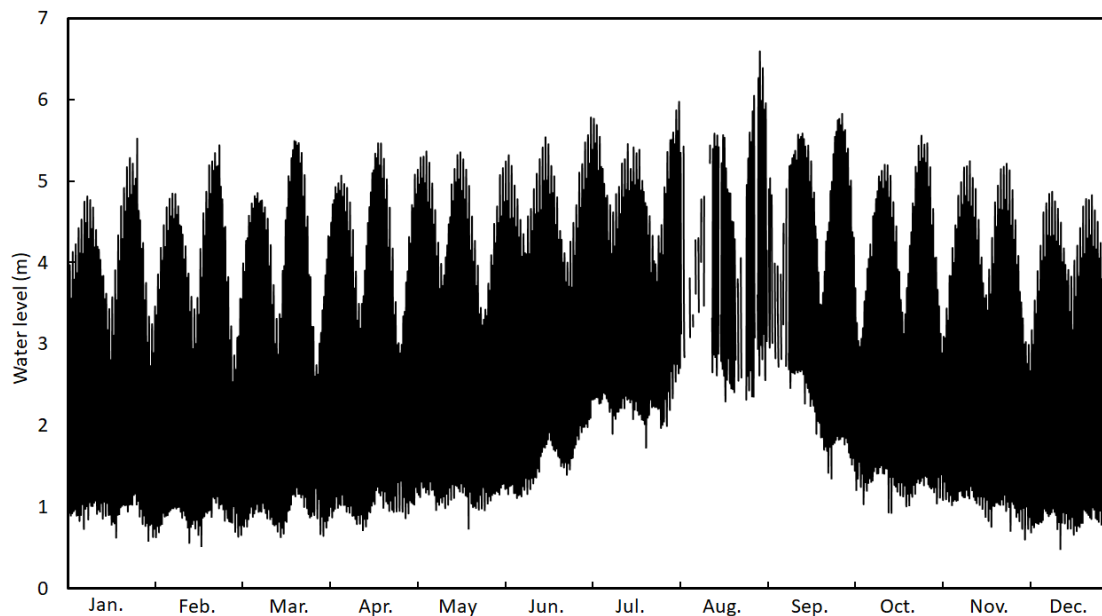


Figure 2.14 Tidal water level (hourly) measured by University of Hawaii Sea Level Center (UHSLC) at Mawlamyine in 2019

During the dry season, especially from January to March, the maximum tidal range remains more than 4 m, however during the monsoon, especially from July to September, the over-all water level rises and the maximum tidal range decreases to 3 m. Figure 2.15 illustrates temporal changes in water level observed in February- 2019. During the first fortnight in February- 2019, the maximum tidal range reaches a level slightly lower than 4 m, however on the second fortnight, especially after February 20, the maximum tidal range reaches up to 4.4 m. The tidal bore propagated landwards around this time.

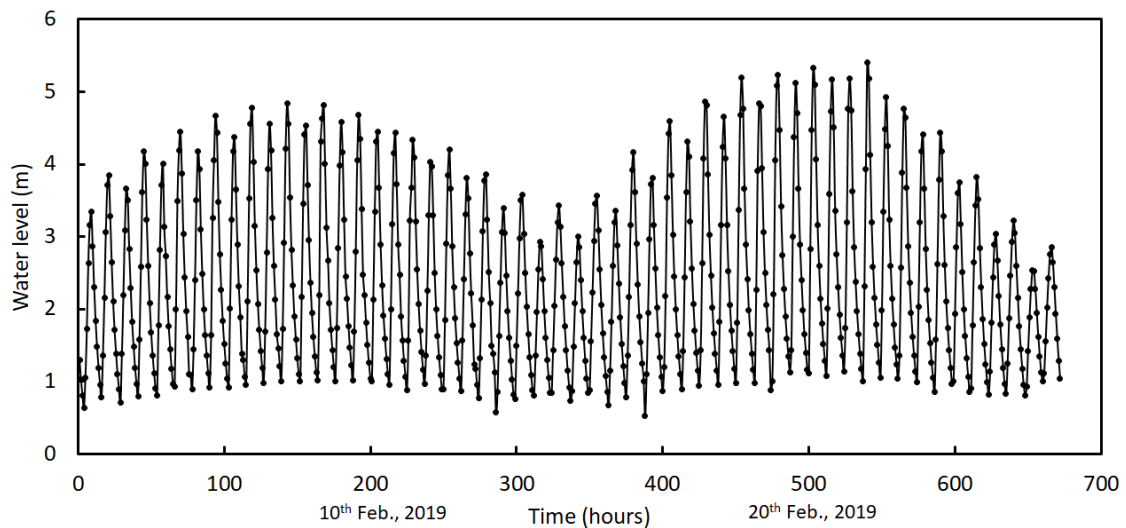


Figure 2.15 Temporal change of water level observed at Mawlamyine during February, 2019

Field surveys were conducted for investigating tidal currents, bed and bank materials, sediment transportation and channel changes in 2017, 2018, 2019 and 2020. One of the major purposes was to grasp a relationship between bank erosion and tidal currents, characteristics of bed and bank materials and associated sediment transportation in the estuary and river reach. Figure 2.16 illustrates the survey sites.

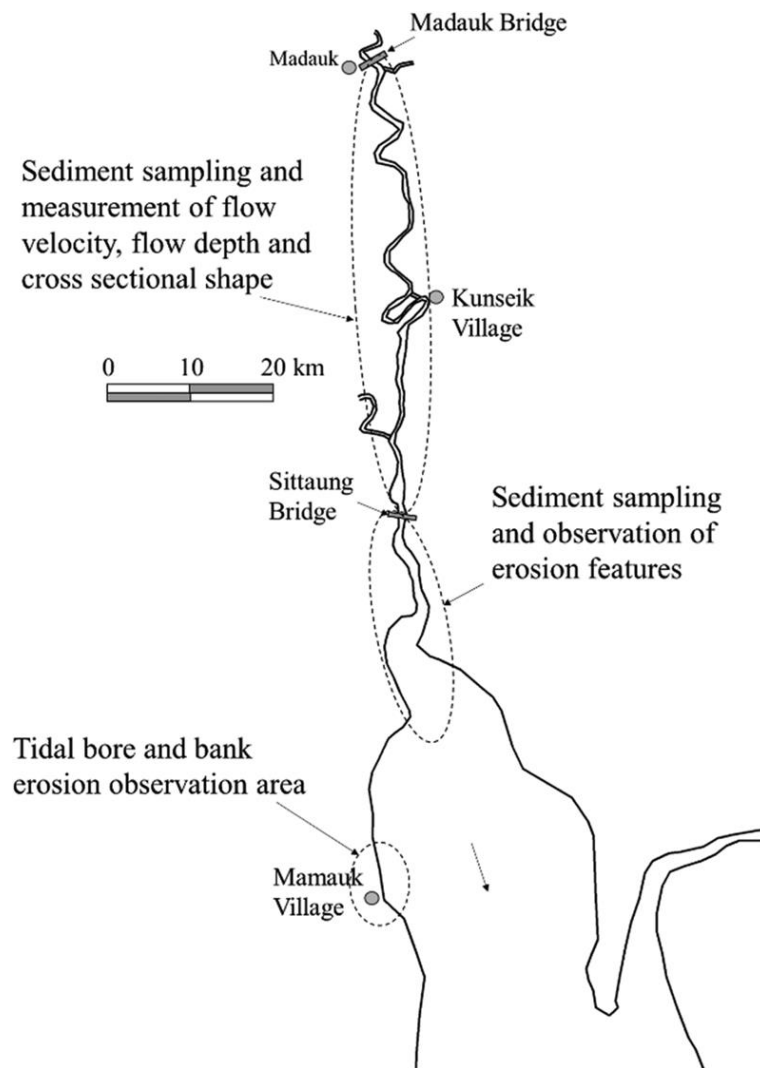


Figure 2.16 Survey sites in Sittaung river and estuary

Tidal bores and associated tidal currents were observed at and near Mamauk (see Figure 2.1), using UAV. Figure 2.17a shows the propagation of a tidal bore during the field survey in February- 2019 and Figure 2.17b shows temporal changes in water surface elevation measured at that time. In these observations, the advancing speed of the bore front and the tidal currents were measured by UAV, and temporal changes in water surface elevation by the Total Station Theodolite (TST) to obtain data for reviewing and completing numerical models described in later chapters for tidal currents. Temporal changes in water surface elevation were measured when the tidal bore took place. The

water level increased by 2 m in half an hour after the tidal bore passed. Analysis of the field data revealed that strong tidal currents with velocities of around 2.5 to 3 m/s formed along different stream channels after the propagation of the tidal bore. Such lateral distribution of tidal current velocity is influenced by tidal range, shallow morphology, channel pattern, convergence of flow along the stream channels, measuring sites and other factors.

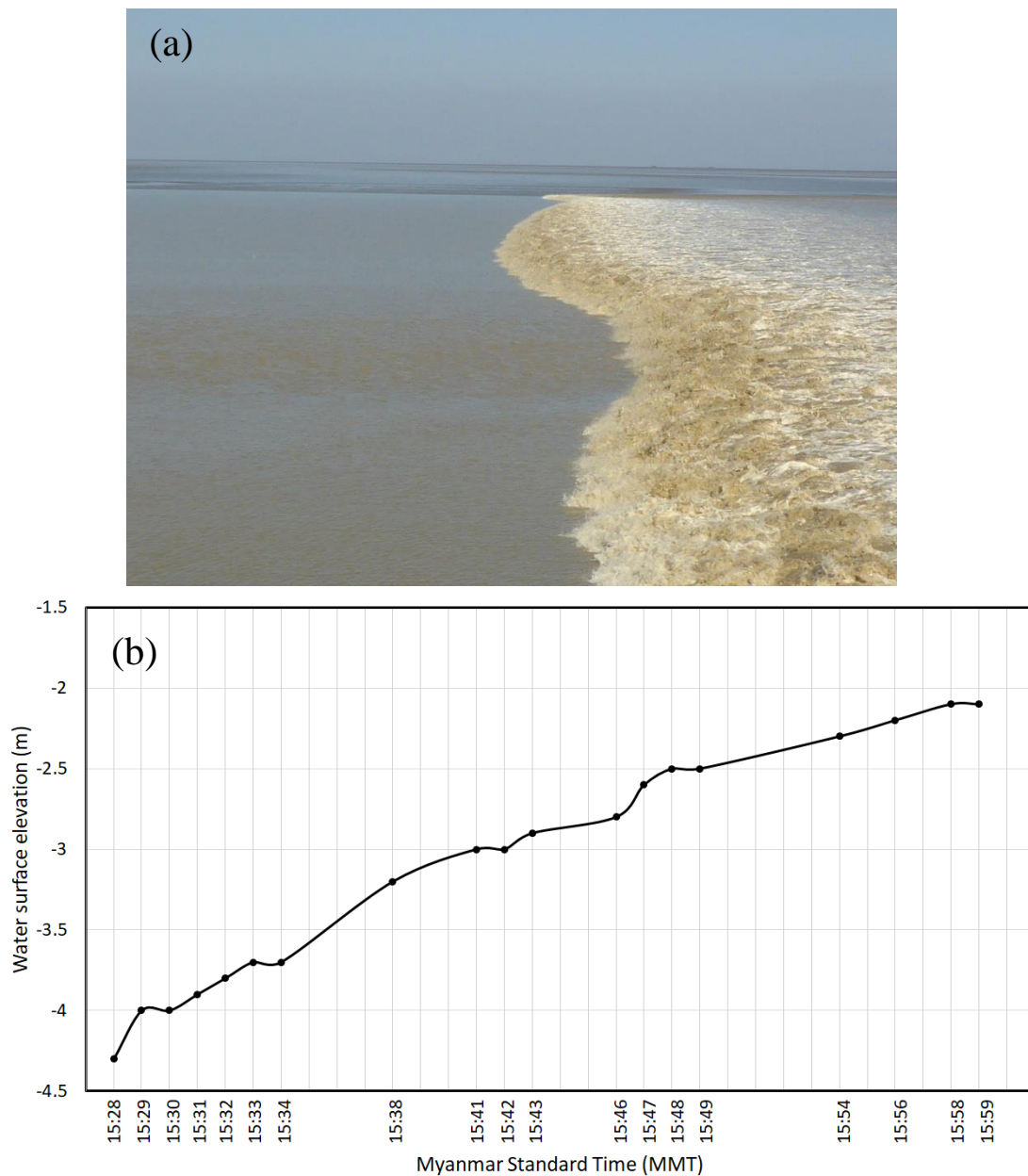


Figure 2.17 (a) Propagation of tidal bore and (b) temporal change of water surface elevation after passage of bore

An engine boat was used to travel along the Sittaung River reach, the Sittaung Bridge area, Alanbya and the estuary (see Figure 2.1 and 2.16) and investigate sediment transport processes focusing on sediment sizes. Many samples were collected from the river and estuary beds as well as from their banks. Bank materials were collected directly using scoop-type samplers, and bed materials were collected using dredge-type samplers. The size distributions of the collected materials were analyzed by sieve tests and their fine particles were investigated by the Laser Diffraction Particle Size Analyzer (Partica LA-960, Horiba).

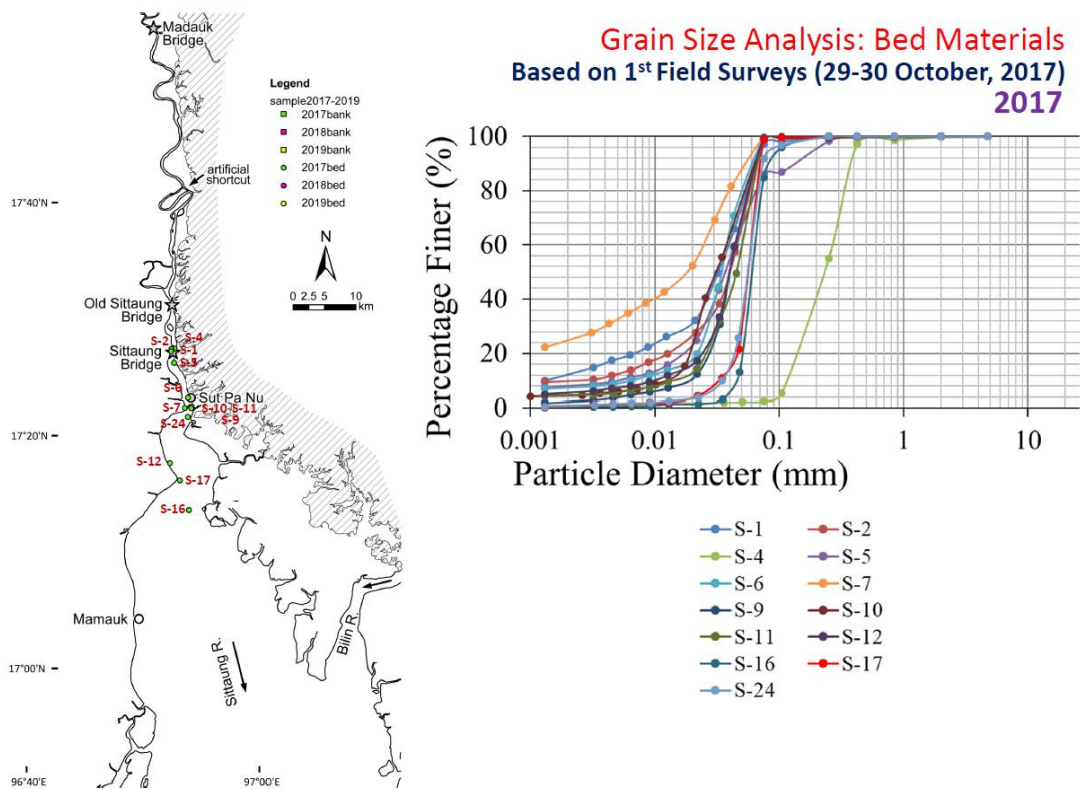


Figure 2.18 Locations of bed materials collected during first field survey in 2017 and their grain size distribution

Figure 2.18 and Figure 2.19 illustrate locations where bed and bank materials were collected during the first field investigation conducted during October 29-30, 2017. Bed and bank materials were collected in the area from Sittaung Bridge to approximately 10

km downstream where Alanbya village faced severe bank erosion and disappeared from the map. Grain size analysis of the collected bed and bank materials showed the presence of very fine particles with mean diameter ranging 0.02 to 0.04 mm.

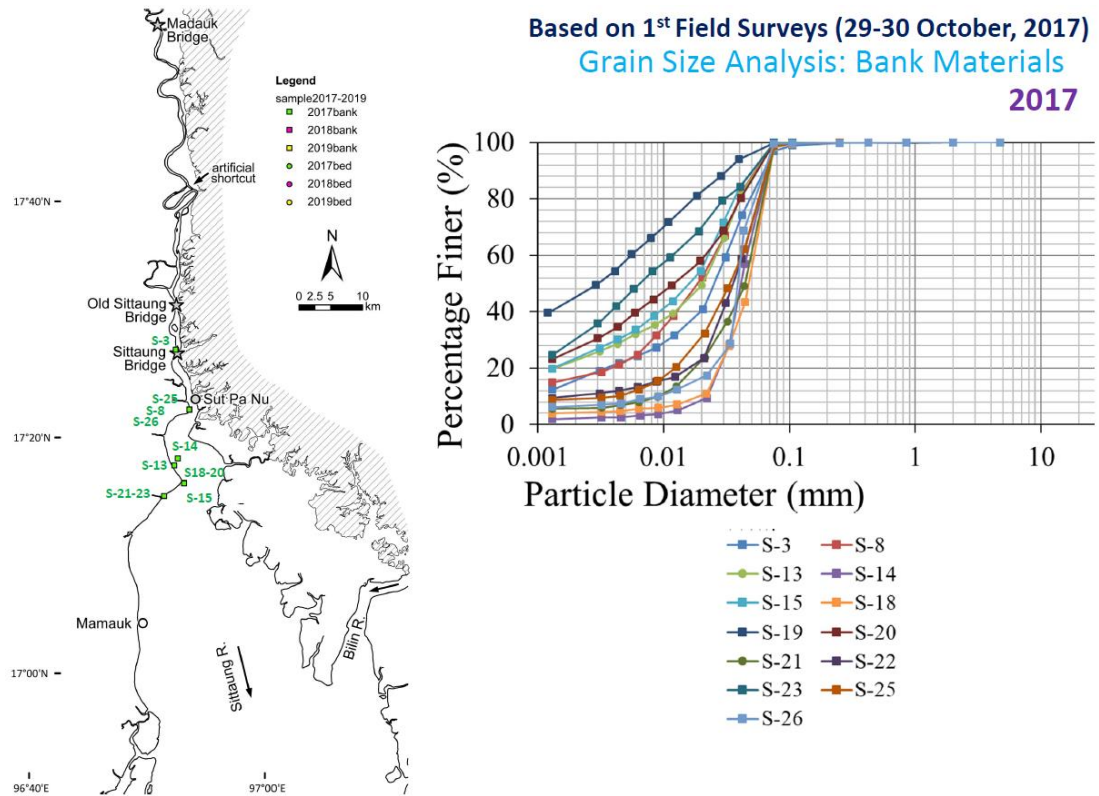


Figure 2.19 Locations of bank materials collected during first field survey in 2017 and their grain size distribution

Figure 2.20 and 2.21 show the locations where bed and bank materials were collected along the Sittaung River reach during the second field survey conducted on February 6-18, 2018. The very important nature of particle sizes was observed. At the lower reach of the river, very fine particles were found in both bed and bank materials, however along the upper reach, much coarser particles were dominant.

Bed and bank materials were collected from Mamauk and some other locations along the Sittaung River during the field investigation on February 21-24, 2019. Figure 2.22 shows the locations of sediment sample collection and Figure 2.23 shows the results

of particle sizes distribution analysis. Very fine particles are found in the erosion prone zone near Mamauk. Similar particle sizes were also found in an area downstream of an artificial shortcut along the Sittaung reach.

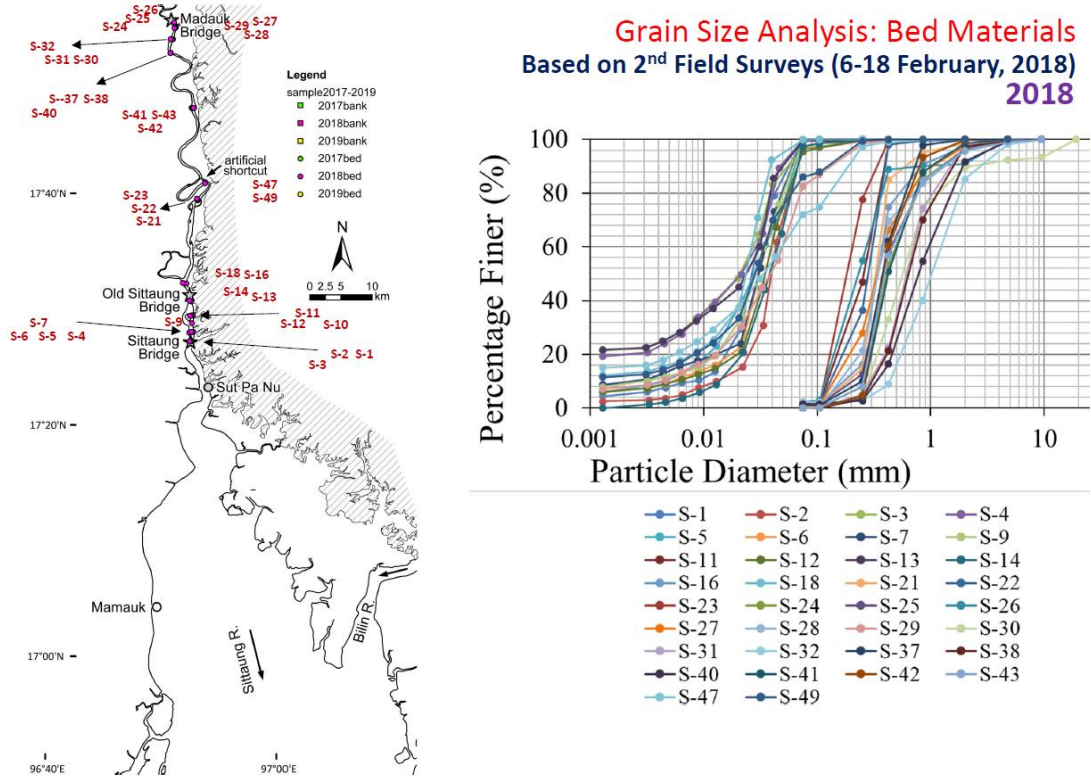
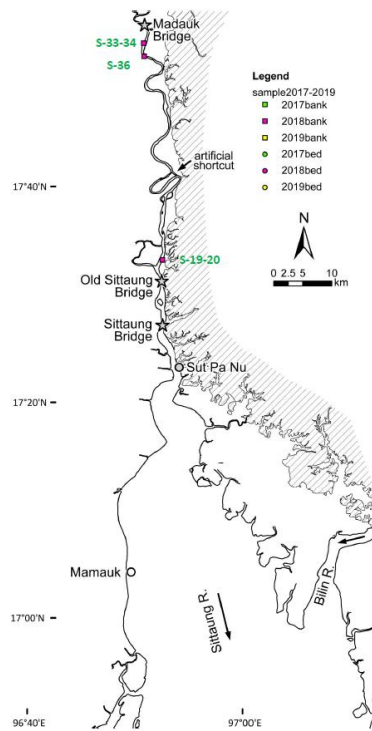


Figure 2.20 Locations of bed materials collected during second field survey in 2018 and their grain size distribution

Figure 2.24 shows the particle size distributions of sediment collected in beds and banks, in which sediment sizes along the river reach are illustrated in the upper two figures and those of the estuary’s sediment are in the bottom two figures. Silt and clay particles are dominant in the bank material according to the results illustrated in Fig. 2.24. The sediment particle sizes of the bed material, ranging from 0.1 mm to 3 mm, in the upper reach from Madauk to Kunseik are coarser than those of the bed material collected in the other locations, and such material was rarely found in the other locations.



Based on 2nd Field Surveys (6-18 February, 2018)
Grain Size Analysis: Bank Materials 2018

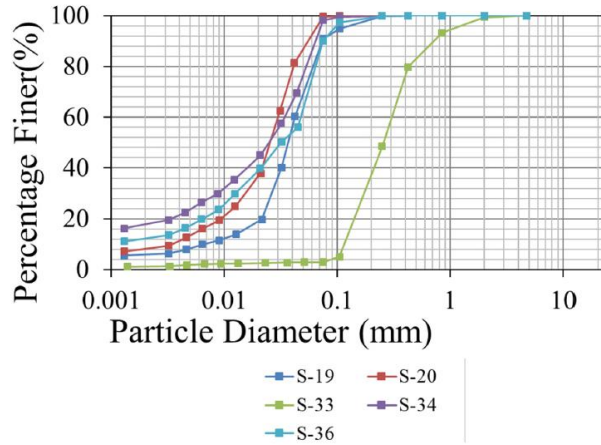
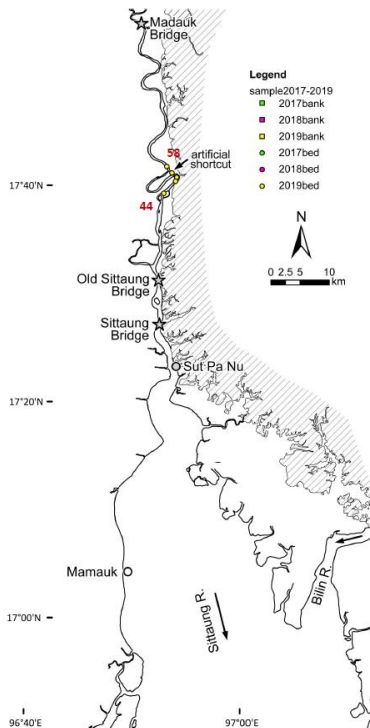


Figure 2.21 Locations of bank materials collected during second field survey in 2018 and their grain size distribution



Based on 3rd Field Surveys (21-24 February, 2019)
Grain Size Analysis: Bed Materials 2019

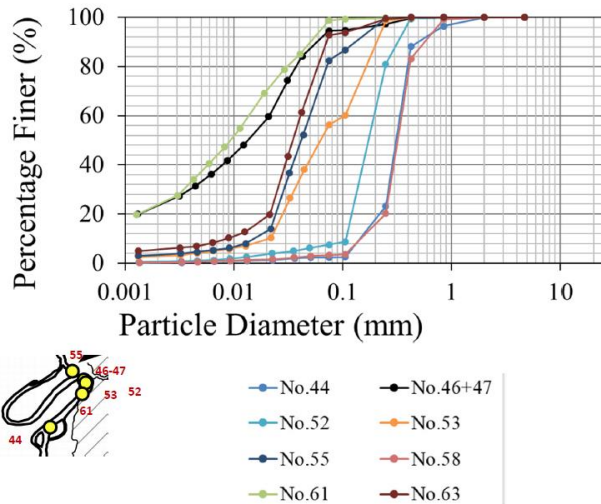


Figure 2.22 Locations of bed materials collected during second field survey in 2019 and their grain size distribution

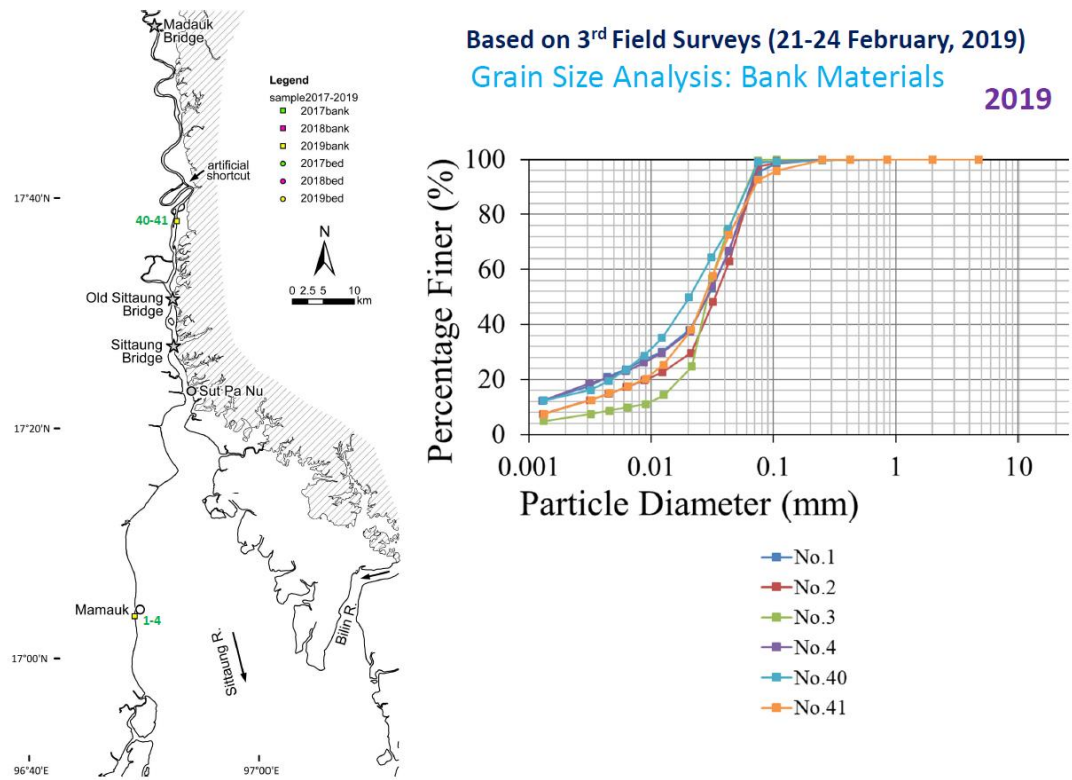


Figure 2.23 Locations of bank materials collected during second field survey in 2019 and their grain size distribution

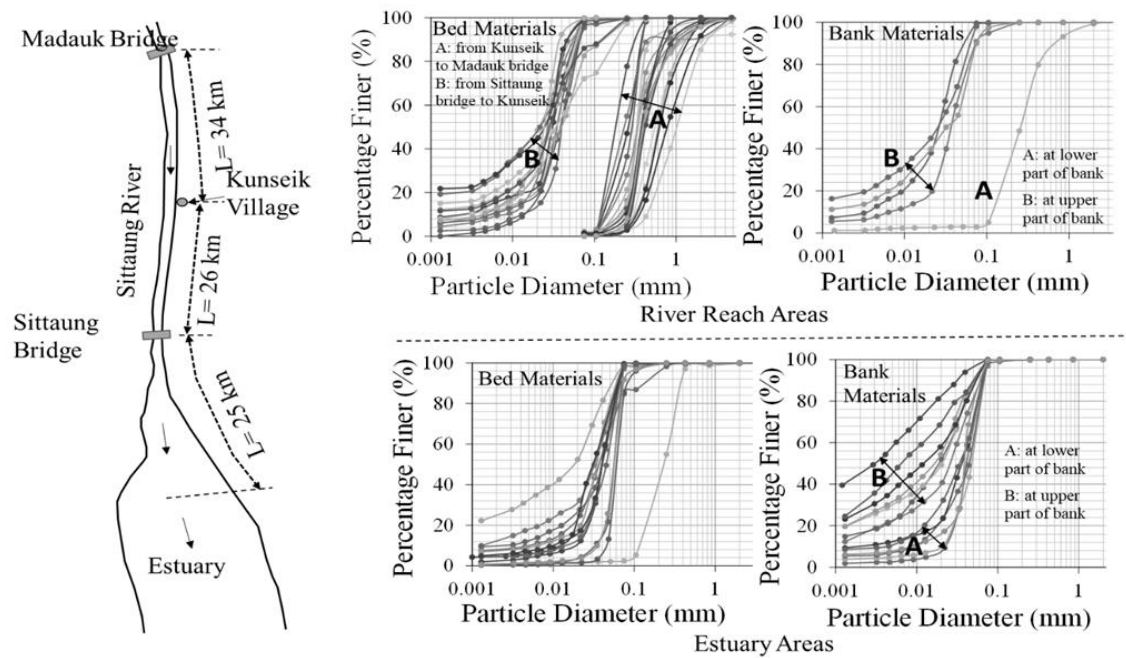


Figure 2.24 Summary of sediment particle sizes measured in the estuary

In addition, the bed sediment sizes in the reach from Kunseik to Sittaung Bridge as well as in the estuary are almost the same as those collected in the river and estuary banks. Such results on sediment sizes suggest that the bed material in the lower river reach and the estuary is supplied from bank regions owing to erosion (Ahmed et al., 2019). In addition, the particle size distribution analysis of the bed material and suspended sediment shows the dominance of very fine particles with average diameters ranging 0.02 to 0.04 mm. Such bed and bank materials exhibit high sediment erodibility and transportability of sediment particles at the study area resulting in rigorous changes in stream channel pattern with sand bars and bank lines. To investigate why such sediment size discrepancy takes place, the sediment transport capacity of the upper reach was computed using the conditions as follows; the flow discharge of 4000 m³/s referring to Figure 2.13, the flow width of 400 m, the water surface slope of 1/20000 obtained from the field survey, Manning's roughness of 0.02, and the sediment size classes of d = 0.2 mm (30%), d = 0.4 mm (40%) and d = 1.0 mm (30%) referring to the upper left in Figure 2.24. Bed load was computed by means of Ashida and Michiue's formula (1972) and suspended load was computed by Lane and Kalinske's formula (1939). Such computations suggest that the bed load rate is 1800 m³/day, and the suspended is 15000 m³/day and the sum of the bed load and the suspended load is 16800 m³/day. According to the flood hydrographs illustrated in Figure 2.13, such a sediment transport capacity of the upper reach is maintained for 30 to 60 days a year. Based on such computations, the volume of sediment transported for 10 years can be estimated as 1 × 10⁶ m³ order of magnitude even without the transportation of suspended sediment. Sediment of the grain sizes illustrated in upper left of Figure 2.24 does not exist in the downstream reach, despite that a large amount of such sediment must be supplied from the upstream reach.

Leuven et al. (2018) described that ‘estuaries typically show converging planforms from the sea into the land. Nevertheless, their planform is rarely perfectly exponential and often shows curvature and the presence of embayments’. They investigated ‘the degree to which the shapes and dimensions of tidal sandbars depend on estuary planform’. Their output implied that ‘Sandbars mainly form where the estuary is wider than expected from an ideal exponentially converging planform between the mouth and the upstream river. At these locations, local flow expansion causes a reduction of the shear stress, which can result in the deposition of sediment’. ‘Excess width is defined as the local width minus the ideal width, which is given as follows.

$$W_{ideal(x)} = W_m e^{-x/L_w} \quad (1)$$

In which x is the distance from the mouth, W_m is the width of the mouth and L_w is the width convergence length (Davies and Woodroffe, 2010) which can be obtained conservatively from a fit on the width of the mouth and the landward river width (Leuven et al., 2018) as follows.

$$L_w = -S \frac{1}{\ln(W_s/W_m)} \quad (2)$$

In which W_m is the local width measured at the mouth of the estuary, W_s is the width measured at the landward side of the estuary and S is the distance between these locations measured along the centerline. This practical method makes the convergence length somewhat sensitive to the selected position of the seaward and landward limit’.

Figure 2.25 shows the Sittaung River estuary area with the local width of approximately 40 km at the mouth, the width of the Sittaung River around 800 m and also the distance between these locations approximately 68 km. According to the exponential

fits discussed above, the ideal width as well as the width of the estuary were evaluated and are shown in Figure 2.26. The evaluation found it inevitable that sand bars would form in the estuary because of its width wider than the ideal estuary. Even from satellite images, the deposition tendency is observed at the center of the estuary where one main channel bifurcates into several smaller channels and longitudinal-shaped sand bars form as described by Dalrymple and Choi (2007).

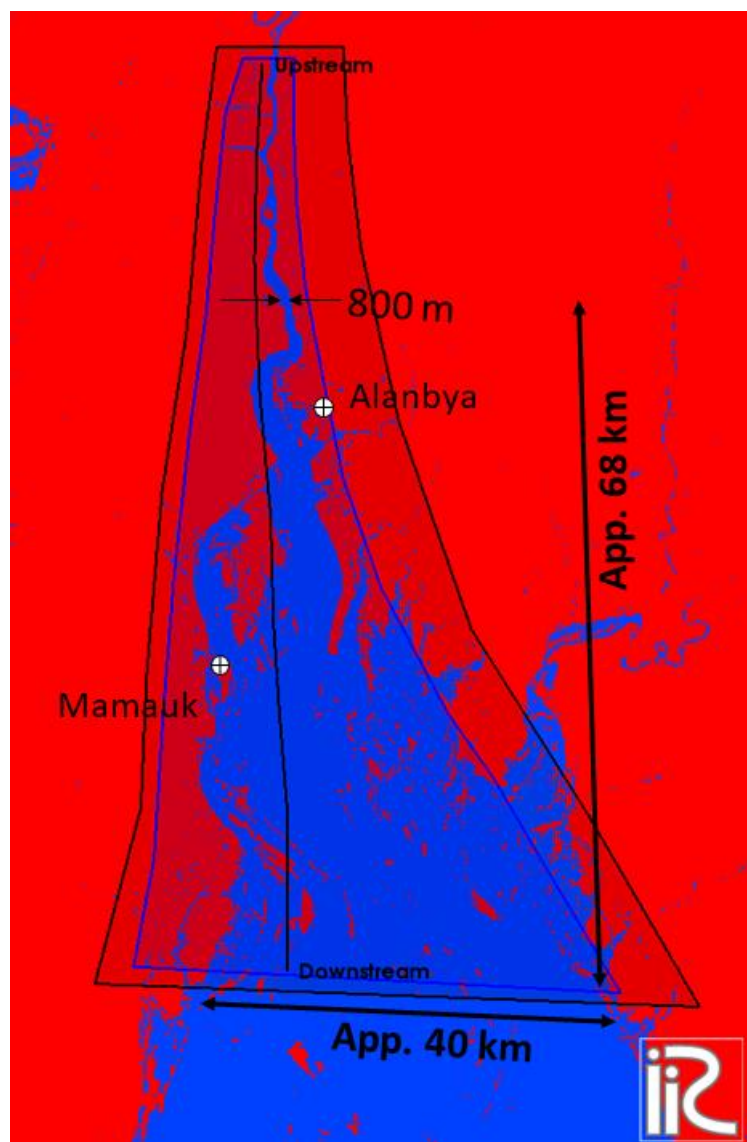


Figure 2.25 Sittaung river estuary for analysis of excess width and the ideal width

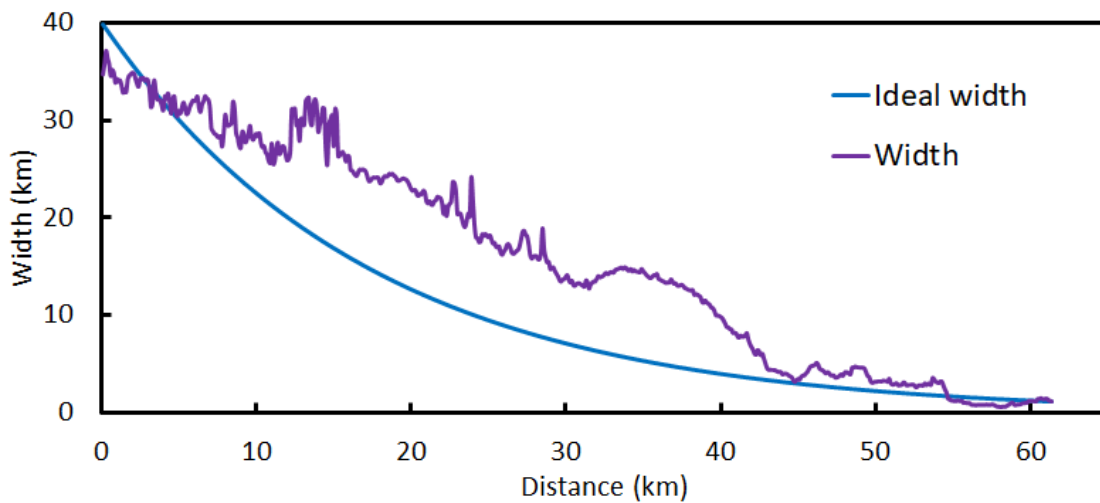


Figure 2.26 Analyzed results of Ideal as well as Excess width

2.4 Summary

This chapter summarizes the characteristics of the study area focusing on the morphological information acquired from historical Landsat satellite images, analyzed data collected during the field investigations and hydrological data collected from secondary sources. Analysis of satellite images clearly identified very active movements of the stream channel and sand bars leading to severe bank erosion with a periodicity of decadal to multi-decadal time-scale. Field investigations revealed that the dominance of very fine particles with median diameter of 0.02 to 0.04 mm in bank and bed materials in the lower reach of the Sittaung River as well as in the estuary must be a reason of rigorous channel changes, sand bar deformation and bank erosion. Historical discharges were observed along the lower reach of the Sittaung River at Madauk and tidal water levels were observed at Mawlamyine. Such data are key to setting up initial and boundary conditions for numerical simulation.

Chapter 3: Numerical model for tidal currents and sediment transportation

3.1 Introduction

The river bed of an estuary or a dam reservoir is often composed of very fine sediment particles measuring tens of micrometers. Such fine materials are easily eroded and transported by the flow, and these phenomena cause morphological changes. For example, as described in the previous chapter, in the Sittaung River estuary, the bed material is composed of particles with d_{50} of around 0.02 to 0.04 mm; hence active sediment transportation occurs, resulting in severe morphological changes, including active bank erosion. To evaluate bed evolution in the region where suspended sediment dominates, mass conservation equations are employed for flow body and bed sediment in addition to the governing equations of water flow. A dispersion equation is used usually for the mass conservation equation of suspended sediment in the flow body, in which the erosion rate plays an important role.

The erosion rate formula has been studied since the beginning of sediment hydraulic research, and many formulas were proposed in relation to the reference sediment concentration. They can be classified into three groups based on the difference in their treatment of the kinematics of bed sediment.

The first group discusses the reference sediment concentration focusing on the mechanism of bed load (Einstein, 1953; Rijn, 1986). Rijn (1984) discussed particles' motion trajectories by means of the mass point system in a logarithmic velocity field over the rigid bed and proposed the following relation.

$$E = 0.015 \frac{D_{50}}{a} \frac{T^{1.5}}{D_*^{0.3}} w_0 \quad (3)$$

In which D_{50} is the median size of bed sediment, a is the reference height, T is the transport stage parameter that has the same meaning as, $T = \frac{\tau_* - \tau_{*c}}{\tau_{*c}}$, D_* is the particle parameter defined as $D_* = D_{50} \left(\frac{(s-1)g}{v^2} \right)^{1/3}$, w_0 is the settling velocity, τ_* is the effective shear velocity, τ_{*c} is the critical shear velocity for initiating bed load motion, s is the specific gravity of the sediment particles, g is the acceleration due to gravity and v is the kinematic viscosity'. He concluded that 'the proposed function for the reference concentration yields good results for predicting the sediment transport for fine particles in the range 100 to 500 micrometers'.

The second group studies the reference sediment concentration based on the statistics of turbulent kinematics and the fall velocity of sediment particles e.g. Ashida and Michiue (1970). The third group discusses the vertical suspension of sediment particles based on the equation of motion for the mass point system. Itakura and Kishi (1980) introduced 'a stochastic nature of fluid force acting on bed sediment into the equation of motion for bed particles in order to evaluate sediment suspension and proposed the following formula.

$$E = K w_0 \left(\alpha_* \frac{\sigma - \rho}{\sigma} \frac{gd}{u_* w_0} \Omega - 1 \right) \quad (4)$$

In which $K = 0.008$, $\alpha_* = 0.14$, σ is the mass density of sediment particles, ρ is the mass density of water, u_* is the shear velocity. Ω is described as follows.

$$\Omega = \frac{\bar{\tau}_* \int_{a'}^{\infty} \xi \frac{1}{\sqrt{\pi}} \exp(-\xi^2) d\xi}{B_* \int_{a'}^{\infty} \frac{1}{\sqrt{\pi}} \exp(-\xi^2) d\xi} + \frac{\bar{\tau}_*}{B_* \eta_0} - 1, a' = \frac{B_*}{\bar{\tau}_*} - \frac{1}{\eta_0} \quad (5)$$

In which $\bar{\tau}_*$ is the time average of the non-dimensional shear stress, $B_* = 0.143, \eta_0 = 0.5$.'

Thereafter, Fujita and Ashida (1986) conducted study on sediment suspension by introducing the coherent structure of turbulence to evaluate fluid forces acting on sediment particles and proposed a formula. In addition to such analytical studies, Garcia and Parker (1991) proposed the following relation involving the effect of density gradient on sediment suspension, based on dimensional analysis.

$$E = w_0 \frac{aZ_*}{1 + \frac{a}{0.3}Z_*} \quad (6)$$

'In which $a = 1.37 \times 10^{-7}, Z_* = \left(\frac{u_*}{w_0}\right)^5 R_{ep}^3, R_{ep} = \frac{\sqrt{\left(\frac{\sigma}{\rho}-1\right)gd^3}}{\nu}$. But this study might focus on non-cohesive nature of sediment particles because the authors introduced that a phenomenon of considerable interest in river mechanics is the erosion, transport, and deposition of non-cohesive material by turbulent open-channel flow. A key feature of this phenomenon is the description of entrainment of sediment into suspension at the solid-fluid interface, i.e., the bed'.

Engelund and Fredsoe (1976) 'presented a simple mathematical model for sediment transport in straight alluvial channels'. It was based on physical ideas related to those introduced by Bagnold (1954), which was originally developed in two steps, the first to describe the bed load transport (Engelund, 1975) and the second step to account for the suspended load (Fredsoe and Engelund, 1976). The model is assumed to have two

advantages as compared with empirical models, first, it is based on a description of physical processes and second, it gives some information about the quantity and size of sand particles in suspension and bed particles.

There are many phenomenological, numerical studies on tidal currents and associated sediment transport processes. Several numerical studies are conducted for simulating tidal bores (Madsen et al., 2005; Pan et al., 2007; Bonneton et al., 2015). However, their models lacked discussion on sediment transportation due to the formation and propagation of tidal bores. Dalrymple, Zaitlin and Boyd (1992) identified the dominance of fluvial and marine processes on the upstream and downstream parts of estuaries. Dalrymple and Choi (2007) proposed ‘schematic map of tide dominated estuary where they showed longitudinal variation of the intensity of the three main physical processes, river currents, tidal currents and waves, the resulting directions of net sediment transport through a tide dominated estuary and longitudinal variation of grain size of the sand fraction, the suspended sediment concentration and bulk grain size of the resulting deposits’. These studies provide qualitative information about the influence of tidal currents and sediment transport in different parts of the estuary. Yu et al. (2012) ‘carried out two-dimensional depth-averaged process-based morpho-dynamic modelling on a schematized funnel-shaped domain in order to investigate the physical processes governing the formation of large sand bar in Qiantangjiang estuary China’. Riddler (2017) set up a two-dimensional numerical model for the tidal bore. He used the model to analyze the effect of the bottom friction, bathymetry, tidal range and river discharge on the propagation of the tidal bore. However, he expressed the limitations of the study; due to lack of data, it was hard to give a solid conclusion about the erosion in the estuary.

Although such rigorous studies have been done, little attention has been paid to develop formulas for treating the sediment transport process in regions where bed material consists of very fine sediment ranging from fine sand to clay-silt grains. Most existing formulas overestimate the sediment concentration when computing suspended sediment in river reaches composed of such material. To find a solution to this problem, this study introduces erosion rate formulas. An erosion rate formula is proposed for the erosion process of bed sediment composed of very fine sediment based on the results of flume tests. The erosion rate formula employs the entrainment velocity to evaluate the mixing process occurring in density stratified flows.

3.2 Governing equations

Tidal bores and associated tidal currents are described by means of depth-averaged two dimensional mass and momentum conservation equations for the flow body. These are illustrated as follows.

$$\frac{\partial h}{\partial t} + \frac{\partial uh}{\partial x} + \frac{\partial vh}{\partial y} = 0 \quad (7)$$

$$\frac{\partial uh}{\partial t} + \frac{\partial uuh}{\partial x} + \frac{\partial uvh}{\partial y} = -gh \frac{\partial(h + z_b)}{\partial x} - \frac{\tau_x}{\rho} + \frac{1}{\rho} \left(\frac{\partial h \tau_{xx}}{\partial x} + \frac{\partial h \tau_{yx}}{\partial y} \right) \quad (8)$$

$$\frac{\partial vh}{\partial t} + \frac{\partial vuh}{\partial x} + \frac{\partial vvh}{\partial y} = -gh \frac{\partial(h + z_b)}{\partial y} - \frac{\tau_y}{\rho} + \frac{1}{\rho} \left(\frac{\partial h \tau_{yy}}{\partial y} + \frac{\partial h \tau_{xy}}{\partial x} \right) \quad (9)$$

In which h is the flow depth, t is the time, u and v are the x and y components of depth-averaged velocity, g is gravitational acceleration, ρ is the mass density of water, τ_{xx} , τ_{yy} , τ_{xy} and τ_{yx} are the depth-averaged Reynolds stresses, τ_x and τ_y are the x and y components of the bed shear stress which are expressed.

$$\frac{\tau_x}{\rho} = C_f u \sqrt{u^2 + v^2}; \frac{\tau_y}{\rho} = C_f v \sqrt{u^2 + v^2}; \quad (10)$$

In which C_f is the friction co-efficient. Using Manning's roughness co-efficient, it is defined as

$$C_f = \frac{gn_m^2}{h^{1/3}} \quad (11)$$

In which n_m is Manning's roughness coefficient and g is gravitational acceleration.

In the present estuary, fine sediment transportation is dominated, thus the mass conservation equations for bed sediment and flow body are described, respectively.

$$\frac{\partial z_b}{\partial t} + \frac{1}{c_s} \left(\frac{\partial q_{bx}}{\partial x} + \frac{\partial q_{by}}{\partial y} + E - D \right) = 0 \quad (12)$$

$$\frac{\partial ch}{\partial t} + \frac{\partial cuh}{\partial x} + \frac{\partial cvh}{\partial y} = \frac{\partial}{\partial x} \left(h \varepsilon_x \frac{\partial c}{\partial x} \right) + \frac{\partial}{\partial y} \left(h \varepsilon_y \frac{\partial c}{\partial y} \right) + E - D \quad (13)$$

In which z_b is the bed elevation, q_{bx} and q_{by} are the x and y components of bed load transport rate, E and D are the erosion and deposition rates of the suspended sediment respectively, c is the depth-averaged sediment concentration and ε_x and ε_y are the dispersion coefficients and at this moment are estimated as follows.

$$\varepsilon_x = \varepsilon_y = \frac{k}{6} u_* h \quad (14)$$

In which k is the Karman's constant ($k = 0.4$) and u_* is the shear velocity.

3.3 Formulas for erosion and deposition rates

As shown in the previous chapter, the estuary is composed of very fine materials, therefore it is difficult to employ existing methods for evaluating an erosion rate of bed

sediment. Instead, this study formulates the erosion rate using an entrainment coefficient or entrainment velocity which is employed for evaluating the mixing process of density stratified flow. In the present treatment, fine sediment assumed to be entrained from a loose bed into the flow body and also the bed surface layer is shearing parallel to the water flow (Ashida & Egashira, 1980). Figure 3.1 is a schematic diagram to formulate the flow velocity in the bed surface layer as well as the erosion velocity (Harada et al., 2019).

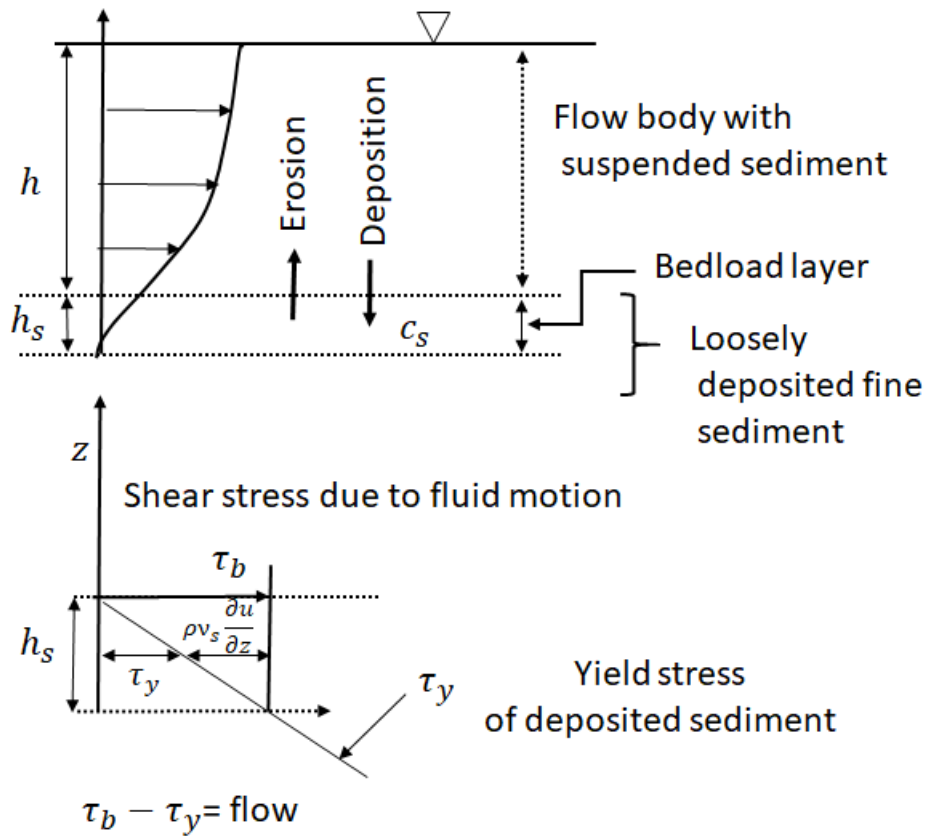


Figure 3.1 Schematic diagram of flow velocity at bed load layer and erosion velocity

According to Egashira et al. (1997), the yield stress can be evaluated using the effective normal stress and the apparent internal friction angle.

$$\tau_y = \rho \left(\frac{\sigma}{\rho} - 1 \right) c_s g (h_s - z) \tan \phi \quad (15)$$

In which τ_y is the yield stress, σ is the mass density of sediment particles, ρ is the mass density of ambient fluid, c_s is the sediment concentration of bed surface layer, g is the gravitational acceleration, h_s is the thickness of bed load layer, z is the bed-normal co-ordinate and ϕ is the apparent internal friction angle. According to Figure 3.1, shear stress τ_b is equal to τ_y at $z = 0$. Thus, the moving thickness of the bed surface layer due to the river bed shear force can be evaluated as follows.

$$h_s = \frac{u_*^2}{\left(\frac{\sigma}{\rho} - 1\right) c_s g \tan \phi} \quad (16)$$

Here, $\tau_b = \rho g h_i e$ and i_e is the energy slope. Supposing that the flow in the bed load layer ($0 < z < h_s$) is laminar flow,

$$\rho \nu_s \frac{\partial u_s}{\partial z} = \tau_b - \tau_y \quad (17)$$

Where ν_s and u_s are the kinematic viscosity co-efficient and the velocity in the bed load layer ($0 < z < h_s$), respectively. Equation 17 is transformed into the following shape.

$$\frac{\partial u_s}{\partial z} = \frac{u_*^2}{\nu_s} \left\{ 1 - \frac{\left(\frac{\sigma}{\rho} - 1\right) c_s h_s}{i_e h} \left(1 - \frac{z}{h_s}\right) \tan \phi \right\} \quad (18)$$

Substitution of Equation 16 to Equation 18 yields the following formula.

$$\frac{\partial u_s}{\partial z} = \frac{u_*^2}{\nu_s} \frac{z}{h_s} \quad (19)$$

Vertical velocity distribution, $u_s(z)$ and mean flow velocity, V are formulated as follows.

$$u_s(z) = \frac{1}{2} \frac{u_*^2 z^2}{\nu_s h_s} \quad (20)$$

$$V = \frac{1}{6} \frac{u_*^2 h_s}{\nu_s} \quad (21)$$

Bed load transport rate is formulated as follows using the relationships of $q_b = c_s V h_s$.

$$\frac{q_b}{u_* h_s} = \frac{1}{6} c_s \frac{u_* h_s}{\nu_s} \quad (22)$$

In which ν_s is the kinematic viscosity of bed load layer and q_b is the bed load transport rate. Equation 22 is employed together with Equation 12 for the numerical model.

E is the erosion velocity of the bed sediment and D is the deposition rate of sediment from the flow body. E and D play important role in present topics; D can be evaluated by means of a general method.

$$D = \alpha w_0 c \quad (23)$$

In which w_0 is the fall velocity and in case of fully mixed sediment particles α takes $\alpha > 1$. Here α is modified as follows.

$$\alpha = \frac{\beta}{1 - e^{-\beta}} \quad (24)$$

$$\beta = \frac{k w_0}{6 u_*} \quad (25)$$

In the present flow field, one of the main issues is to specify the erosion rate, E . It is assumed that the erosion rate can be described using entrainment velocity that is similar to density stratified flow.

$$E = W_e c_s \quad (26)$$

In which W_e is the entrainment velocity at the interface between the bed load layer and the upper flow layer.

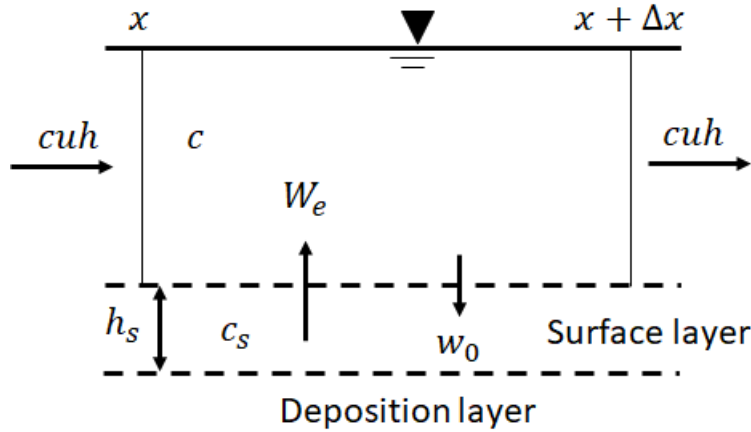


Figure 3.2 Control volume for mass conservation equation of very fine sediment

Figure 3.2 shows a schematic diagram to formulate the mass conservation of very fine sediment in water in a one-dimensional field. The bed sediment is entrained into the flow body following Equation 26 and fine sediment in water deposits following Equation 23. Therefore, the mass conservation of fine sediment in water is described as the following advection-dispersion equation.

$$\frac{\partial ch}{\partial t} + \frac{\partial cuh}{\partial x} = \frac{\partial}{\partial x} \left(\varepsilon h \frac{\partial c}{\partial x} \right) + W_e c_s - \alpha w_0 c \quad (27)$$

In which c is the concentration of fine sediment particle in the water, u is the mean velocity, and ε is the dispersion coefficient.

The continuity equation of water is described as follows.

$$\frac{\partial h}{\partial t} + \frac{\partial uh}{\partial x} = W_e - \alpha w_0 \frac{c}{c_s} \quad (28)$$

From Equations 27 and 28, the suspended sediment concentration is described as follows.

$$\frac{\partial c}{\partial t} + u \frac{\partial c}{\partial x} = \frac{1}{h} \frac{\partial}{\partial x} \left(\varepsilon h \frac{\partial c}{\partial x} \right) + \frac{1}{h} \left(1 - \frac{c}{c_s} \right) (W_e c_s - \alpha w_0 c) \quad (29)$$

The entrainment phenomena have been studied to evaluate mixing processes in density currents such as density under flows, density horizontal jets etc. (Ellison and Turner, 1959). However, the entrainment velocity is evaluated using the result obtained from density stratified flow (Egashira & Ashida, 1980).

$$\frac{W_e}{\sqrt{u^2 + v^2}} = \frac{K}{R_{i*}} \quad (30)$$

In which K is the empirical constant specified as $K = 0.0015$ (Egashira & Ashida, 1980), R_{i*} is overall Richardson number defined as

$$R_{i*} = \frac{\frac{\Delta \rho}{\rho} g h}{u^2 + v^2}; \left(\frac{\Delta \rho}{\rho} = \left(\frac{\sigma}{\rho} - 1 \right) c_s \right) \quad (31)$$

Erosion rate formula and bed load rate formula are prepared now to complete governing equations for sediment transport processes in estuaries.

3.4 Tests of validity for simulating tidal currents

Tidal bores and associated tidal currents are reproduced numerically considering the entire Gulf of Martaban. Details of the computation domain and calculation conditions

Table 1 Calculation condition for tidal bore and associated tidal currents

Cases	Shape of estuary	Flow discharge at upstream end, Q (m ³ /s)	Tidal motion at downstream $r = \text{Amplitude (m)}$	Initial bed slope, i_b	Grid system $\Delta x = \text{longitudinal}$ $\Delta y = \text{lateral}$
1	Observed in February, 2019	500	$T = 12$ hours $r = 0.8 \text{ m}, 1 \text{ m}, 1.2 \text{ m}, 1.4 \text{ m}, 1.6 \text{ m}, 1.8 \text{ m}, 2 \text{ m}$	$\frac{1}{20000}$	$\Delta x \approx 200 \text{ m}$ $\Delta y = 30 \sim 100 \text{ m}$ (in middle) $\Delta y = 100 \sim 1200 \text{ m}$ (in downstream)
2	Observed in February, 2020		$T = 12$ hours $r = 3.5 \text{ m}$	$\frac{1}{10000}$	

are summarized in Table 1. The computation time step is one second and flow pattern is surveyed every five seconds to catch discontinuous changes in water surface configuration representing the tidal bore. Case 1 is to investigate the occurrence conditions of tidal bores in the Sittaung estuary. In this case, the characteristics of tidal bores are investigated numerically by means of different tidal amplitudes, focusing on the water surface configuration. In case 2, computation is conducted to survey temporal changes in water surface elevation immediately after the passage of the tidal front near Mamuk as well as to compare them with observed data. To test the validity of numerical model, several specified sites are employed to compare the computed results and observed data. Figure 3.3 illustrates such specified sites.

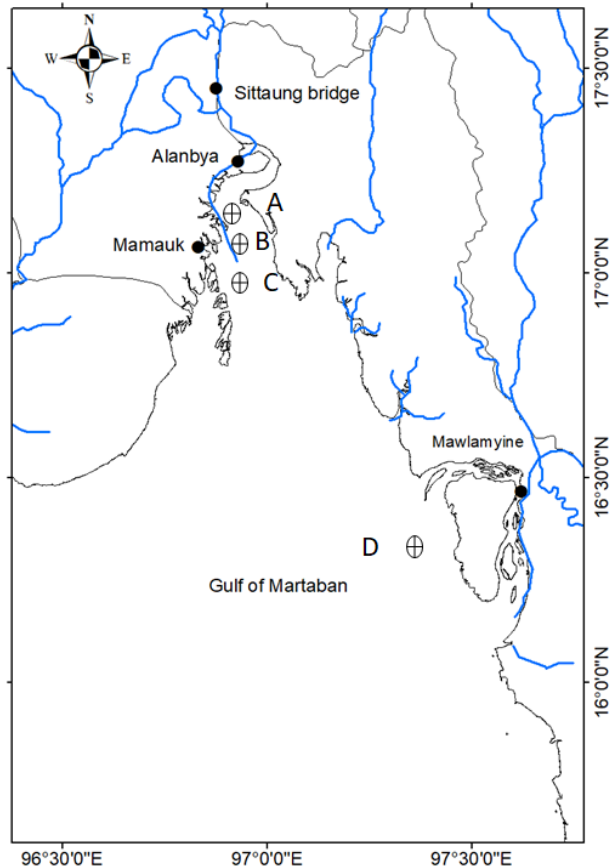


Figure 3.3 Specified locations for comparison of computed results and observed data

To test the performance of the model in simulating tidal currents, computed velocity and suspended sediment concentration are compared with observed data and illustrated here. Figure 3.4 shows temporal changes in computed and observed velocities at the Alanbya village location. Velocity measurements were conducted after the propagation of the tidal bore and during the ebb current. The results show that the computed and observed velocities agree well with each other.

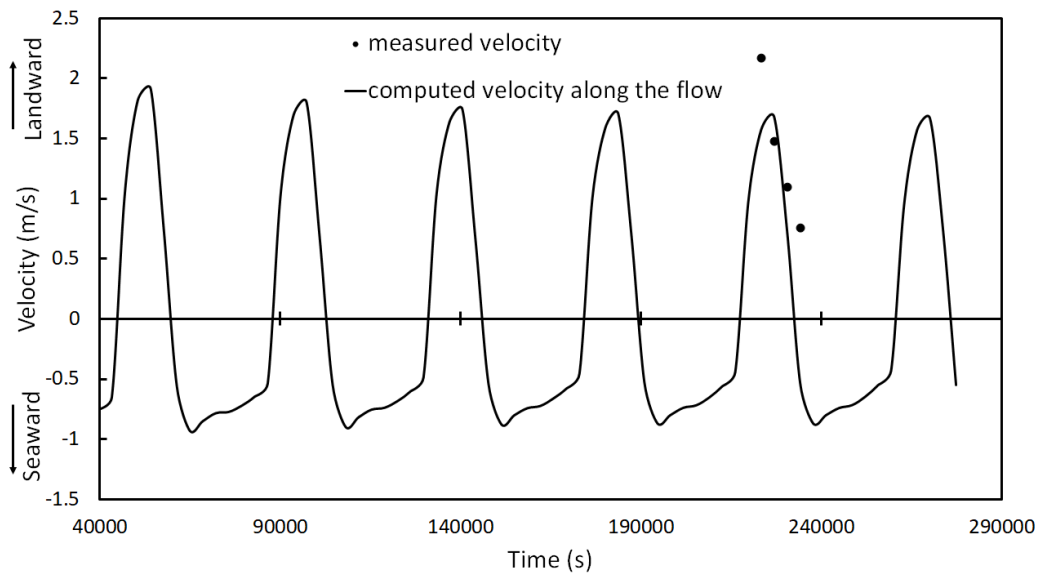


Figure 3.4 Computed and measured velocities at Alanbya

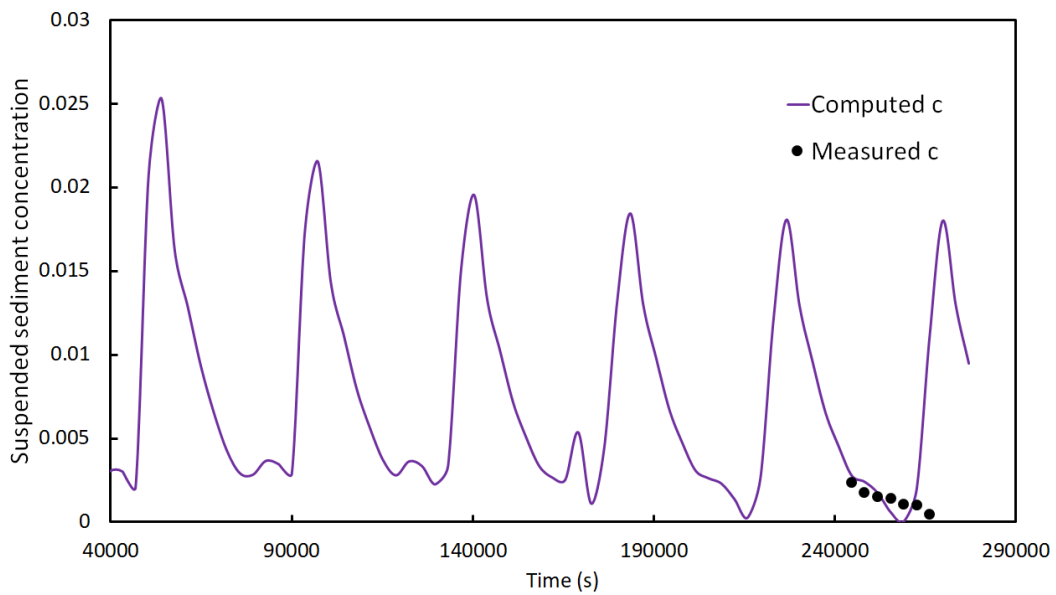


Figure 3.5 Computed and measured suspended sediment concentration at Alanbya

Figure 3.5 shows computed temporal changes in suspended sediment concentration at the Alabya village location. It was difficult to conduct measurements during a flood tide due to the formation of a tidal bore. For this reason, velocity and sediment concentration were measured during the ebb tide only. Measured and computed sediment concentrations show an impressive agreement with each other. The computed sediment concentrations show that it changes corresponding to the strength of tidal currents. This means that tidal bores and associated strong currents bring sediment flux towards the estuary.

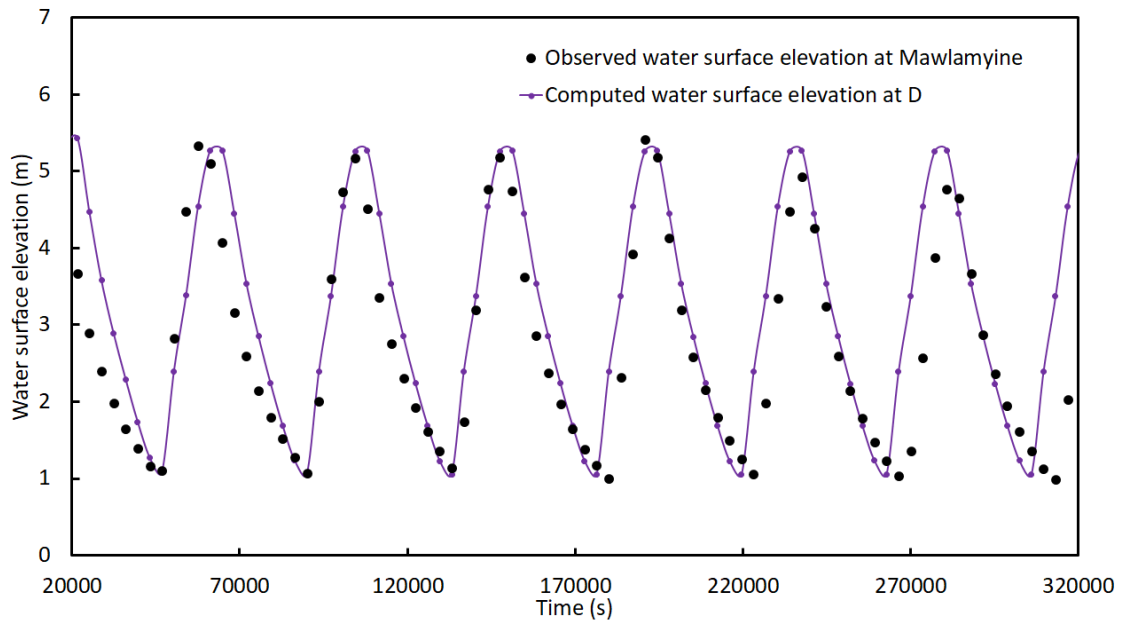


Figure 3.6 Comparison of computed results on water surface elevation at D (see Figure 3.3) with observed data

Figure 3.6 shows the computed results on temporal changes in water surface elevation at site-D together with observed values. The computed results coincide with the observed values at site-D. The water surface configurations with different tidal amplitudes are computed in order to investigate the occurrence condition in the Sittaung estuary. Figure 3.7 shows the computed results at Mamauk for this purpose. The

computed results show that some discontinuous changes, like a bore head, takes place clearly at the longitudinal profile, and that they decrease as the amplitude decreases. However, it is difficult to identify the occurrence condition using the present computational results.

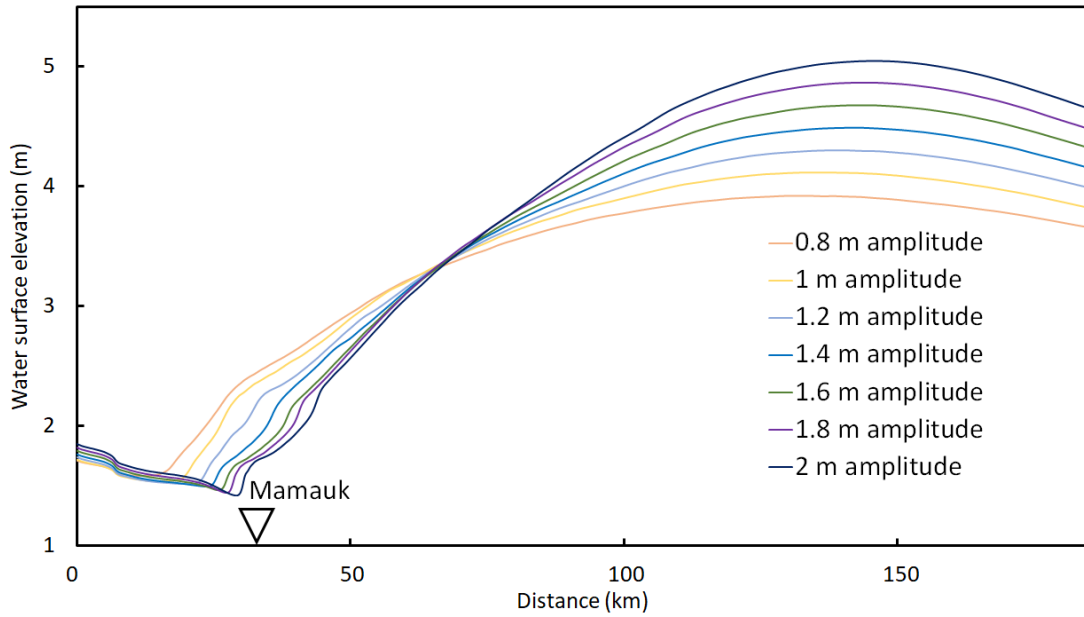


Figure 3.7 Computed water surface configurations for case 1

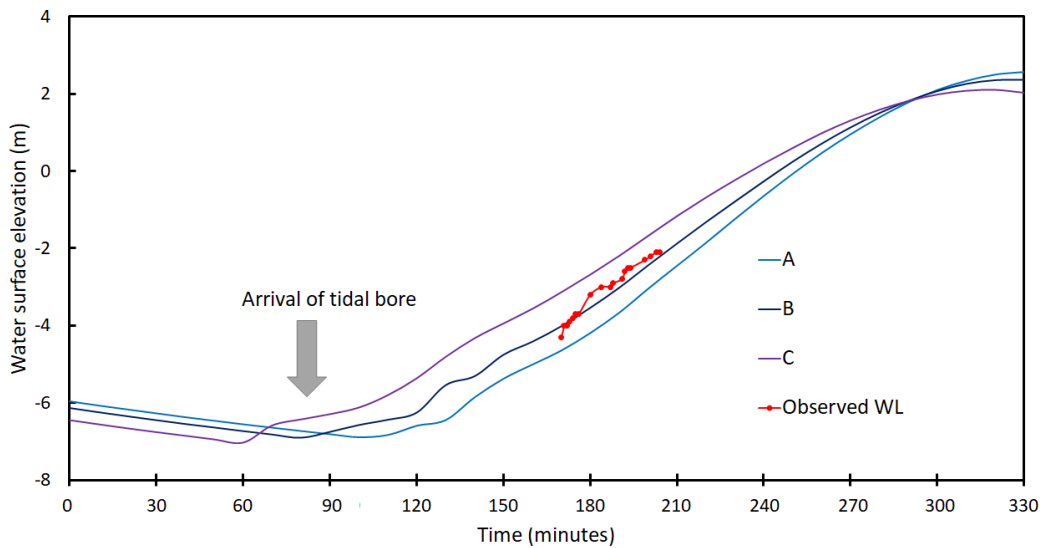


Figure 3.8 Temporal changes of computed water surface elevations at sites near Mamauk and comparison with observed data

Case 2 is to check capability of numerical model through comparing computed temporal change of water surface elevation with the observed data. Figure 3.8 shows temporal changes in water surface elevation which are computed at sites A, B and C (see Figure 3.3). Site-B is near Mamauk where temporal changes in water surface elevation were observed during the passage of the tidal bore. The results illustrated in this figure show that the computed profile agrees very well with the observed values.

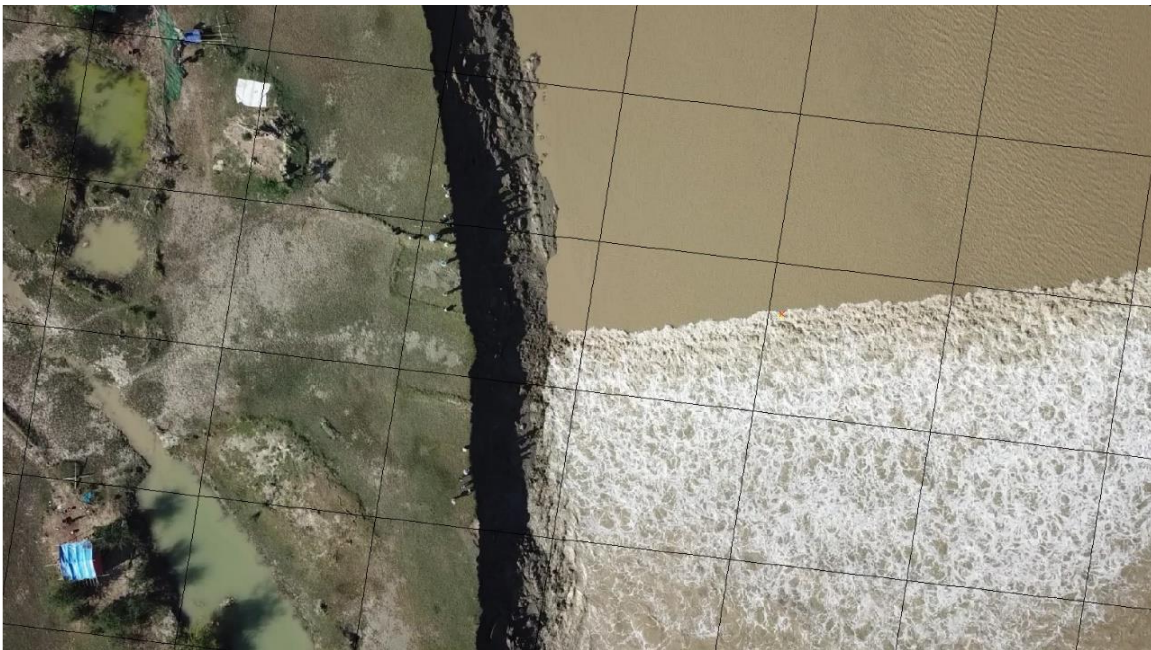


Figure 3.9a Tidal bore front captured using Unmanned Aerial Vehicle (UAV) during the field observation

Figure 3.9a shows a still picture of the propagation of a tidal bore near Mamauk taken using UAV during the field observation of February, 2019. Figure 3.9b illustrates the computed velocity field that reproduces the tidal bore near Mamauk. Two opposing velocity vectors in two consecutive grids represent the propagation of the tidal bore followed by strong tidal currents which are illustrated as red colored fringes. The top view of the bore and the computed velocity vectors using the model show similar tendency of propagation. Comparison of computed results with observed data and images

show that tidal bore and associated tidal currents can be computed well using the proposed model.

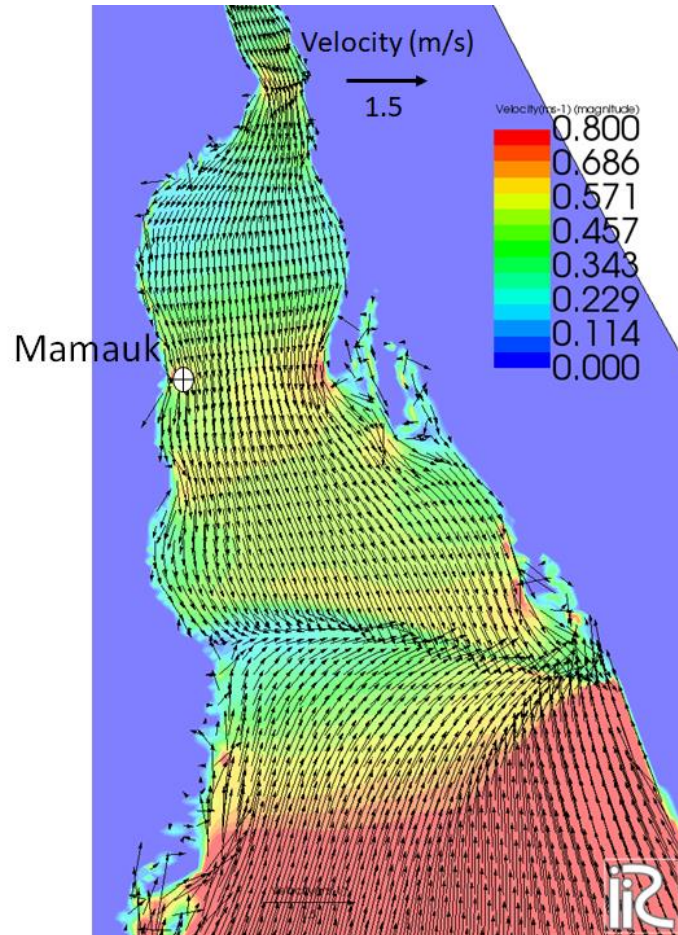


Figure 3.9b Computed velocity field reproducing the tidal bore near Mamauk

3.5 Tests of validity for prediction of particle sizes distribution

Assuming an equilibrium state of suspended sediment transportation, Equation 13 is simplified as follows.

$$E = D \tag{32}$$

Substituting Equations 23, 26 and 30 into Equation 32, a formula for equilibrium sediment concentration is obtained.

$$c_e = \frac{K}{R_{i*}} \frac{v}{\alpha w_0} c_s \quad (33)$$

In which c_e is the equilibrium concentration of suspended sediment and c_s is sediment concentration in the bed surface layer. The erosion and deposition rates are specified already by Equations 26 and 23. Using Equations 23, 26 and 32, the sediment concentration of the flow body can be written as follows.

$$c = \frac{W_e}{\alpha w_0} c_s \quad (34)$$

This is the equilibrium sediment concentration described by particle fall velocity and entrainment velocity.

In extending Equation 34 to heterogeneous sediment particles, Equation 34 can be described as follows.

$$c_i = \frac{W_e}{\alpha w_{0i}} c_{si} \quad (35)$$

In which c_i is the suspended sediment concentration of size-class d_i and c_{si} is the sediment concentration of size-class d_i in the bed surface layer. Particle size distribution p_{si} for size-class d_i is defined as follows.

$$p_{si} = \frac{c_i}{\sum_i c_i} \quad (36)$$

Substitution of Equation 35 into 36 yields,

$$p_{si} = \frac{\frac{c_{si}}{w_{0i}}}{\sum_i \frac{c_{si}}{w_{0i}}} \quad (37)$$

Equation 35 shows that sediment size fraction of suspended sediment is determined only by the sediment size fraction of the bed surface layer.

In case that sediment concentration cannot be assumed to be uniform due to an increase in sediment size, the deposition rate should be modified as follows.

$$D_i = \alpha_i w_{0i} c_i \quad (38)$$

For each size-class d_i , Equation 32 can be re-written as follows.

$$E_i = D_i \quad (39)$$

Using Equations 38 and 39, the sediment concentration of the flow body for each sediment size class can be evaluated as follows.

$$c_i = \frac{W_e c_{si}}{w_{0i} \alpha_i} \quad (40)$$

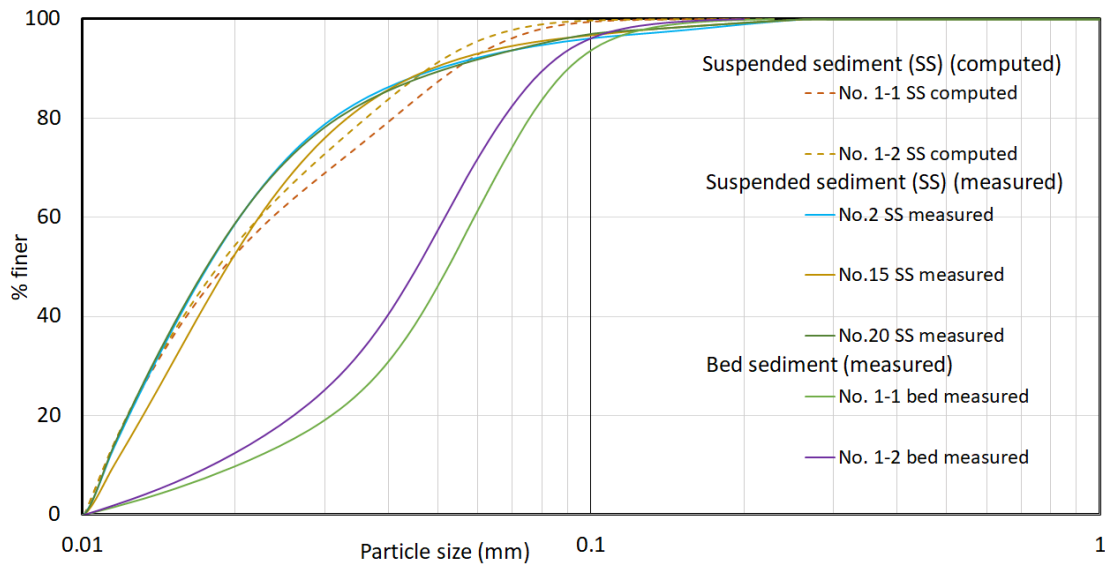
Similarly in derivation of Equation 37, we obtain

$$p_{si} = \frac{\frac{c_{si}}{\alpha_i w_{0i}}}{\sum_i \frac{c_{si}}{\alpha_i w_{0i}}}; \alpha_i > 1, \alpha_i < \alpha_{i+1} \quad (41)$$

Generally, sediment concentration decreases towards the free surface, α_i takes a value larger than unity.

Several samples of bed material and suspended sediment were collected during the field survey conducted in February, 2020 in order to test the validity of Equation 27 which evaluates the particle size distribution using bed sediment. Figure 3.10 shows computed results of particle size distributions of suspended sediment, together with size distribution curves for the collected material. Very fine material composed of clay-particles finer than 0.01 mm in diameter, hardly deposits, thus it does not obey the

erosion-deposition principle for the present treatment. For this reason, such fine material was eliminated for the present computation. The computed suspended sediment size distributions were compared with observed data and they show good agreement with each other. This suggests that the proposed method to evaluate the particle size distribution of suspended sediment using bed sediment only seems to be a reasonable tool.



Note: No. 1-1, No. 1-2, No. 2, No. 15 and No. 20 were collected at about 10 km downstream of the Sittaung Bridge.

Figure 3.10 Computed size distribution curves of suspended sediment together with measured suspended and bed sediment

3.6 Rule of channel bifurcation and lifetime of channels

In reality, when a new channel is formed, the discharge is high initially and the corresponding suspended sediment discharge is also high along that particular channel. Transported sediment deposit along the channel or at the frontal area. Gradually the sediment transport capacity of the channel reduces and then channel closing occurs leading to the bifurcation and formation of new channels. However, several studies have been conducted to show differences in delta formation processes and channel bifurcation characteristics based on particle sizes, tidal range, upstream discharge, winds, waves and many other governing factors (Endmonds and Singerland, 2009; Martin et al., 2009; N.

Geleynse et al., 2011; Rossi et al., 2016). In view of the past studies, channel bifurcation is explained based on bed shear stress, suspended sediment discharge and cumulative volume of suspended sediment discharge.

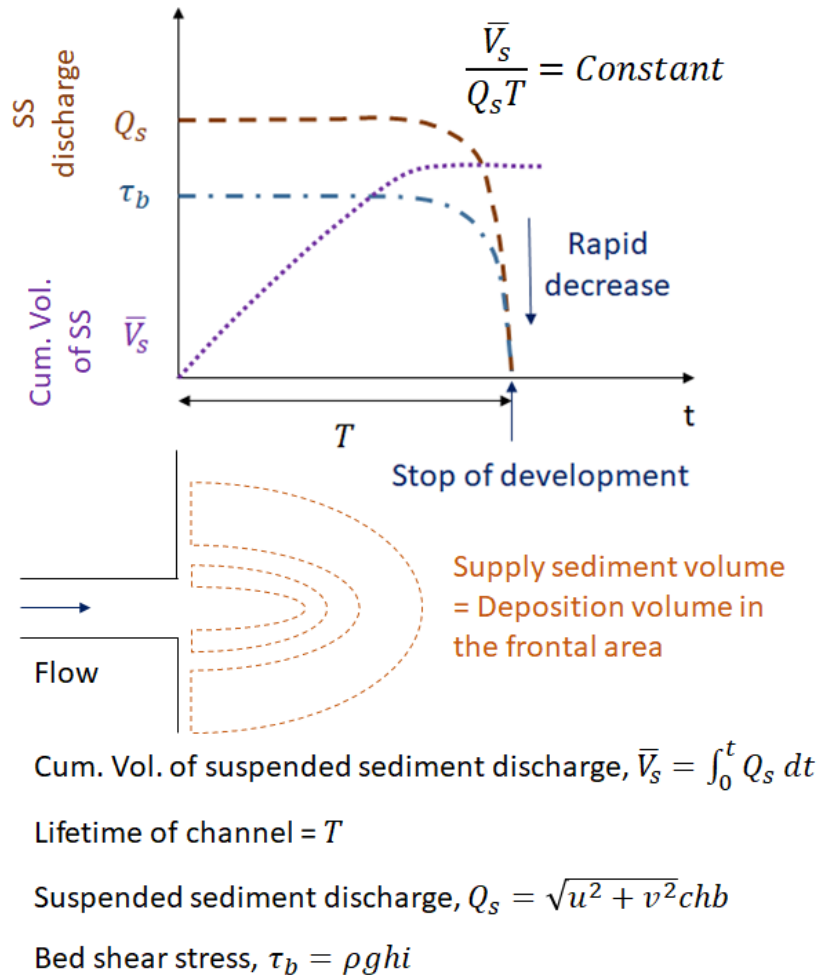


Figure 3.11 Schematic diagram for channel bifurcation and lifetime of channel

Figure 3.11 illustrates a schematic diagram of temporal changes in hydraulic parameters along a single channel. Along the channel, the supply sediment volume must be equal to the deposition volume in the frontal area. After deposition takes place, the sediment transport capacity along the channel would reduce drastically leading to a drop in suspended sediment discharge resulting in subsequent channel closing. Then the lifetime of the channel would be the product of a factor multiplied by the ratio of

cumulative volume of suspended sediment discharge and the suspended sediment discharge along the channel. The equations are as follows.

$$Q_s = \sqrt{u^2 + v^2} chb \quad (42)$$

$$\bar{V}_s = \int_0^t Q_s dt \quad (43)$$

$$\frac{\bar{V}_s}{Q_s T} = \text{Constant} \quad (44)$$

In which u and v are the x and y components of depth-averaged velocity, c is depth averaged suspended sediment concentration, h is the depth of flow, b is the width of channel, Q_s is suspended sediment discharge, \bar{V}_s is the cumulative volume of suspended sediment discharge and T is the lifetime of the channel.

3.7 Summary

As the bed of the study area is composed of very fine materials with mean diameters ranging 0.02 to 0.04 mm, existing methods over-estimates equilibrium sediment concentration. This study proposed a new method to evaluate the erosion rate of fine sediment particles by introducing the concept of entrainment for evaluating a mixing process of density stratified flow. The applicability of the proposed method was investigated based on results of flume experiment, suspended sediment concentration in the equilibrium sediment and prediction of particle size distributions of suspended sediment. Tidal bores and associated tidal currents are simulated using the proposed model and computed results are compared with observed data. Lifetime of channel is discussed in terms of discharge and volume of suspended sediment and rule for channel bifurcation is proposed.

Chapter 4: Numerical simulations on sand bar evolution, bank erosion and decadal periodicity of channel change

4.1 Introduction

Numerical model was tested through simulating tidal bore, tidal currents and predicting particle sizes of suspended sediment in the previous chapter. This chapter aims to investigate sand bar evolution, bank erosion and possible countermeasure for bank erosion, channel bifurcation and the decadal periodicity of channel change. The computation domain was specified by considering the computation facility focusing on the geometrical characteristics of river-estuary system in the target area. Computed results on stream channel pattern and sand bars were discussed and compared with available satellite images. An existing bank erosion model is employed to compute bank erosion and findings are illustrated. In addition, performance of spur dykes is tested as probable solution in treating bank erosion. Moreover, using the experimental domain, channel bifurcations and lifetime of channels are discussed using numerical simulation. Such computed results are provided in this chapter.

4.2 Numerical simulation of sand bar evolution

Sediment transportation, sand bar evolution and corresponding channel changes are computed using the domain which is specified for computation time saving as approximately 115 km long from the upstream boundary at Sittaung bridge and approximately 115 km wide at the downstream boundary. Due to lack of cross-sectional information, the bed elevation was assumed flat at initial stage. The calculation conditions are summarized in Table 2. Case 3 is to investigate temporal and spatial changes of bed morphology and flow pattern as well as to reproduce the bed morphology identified in

February, 2019. Similarly, Case 4 is to reproduce the pattern of bed geomorphology observed in November, 2017.

Table 2 Calculation conditions for creation of bed morphology

Cases	Shape of estuary	Upstream condition		Downstream condition		Initial bed slope, i_b	Grid system
		Flow, Q (m^3/s)	Sediment supply	Tidal motion $r =$ Amplitude (m)	Sediment supply		
3	Observed in February, 2019					$\frac{1}{20000}$	$\Delta x \approx 100 m$ $\Delta y = 40\sim 550 m$ (in downstream)
4	Observed in February, 2017	3000	Equilibrium	$T = 12$ hours $r = 2$ m	Equilibrium		

Parameters employed in computations: Reference particle size, $d = 0.03$ mm, Computation time-step, $\Delta t = 0.2$ s, Kinematic viscosity, $\nu = 0.01$ cm^2/s

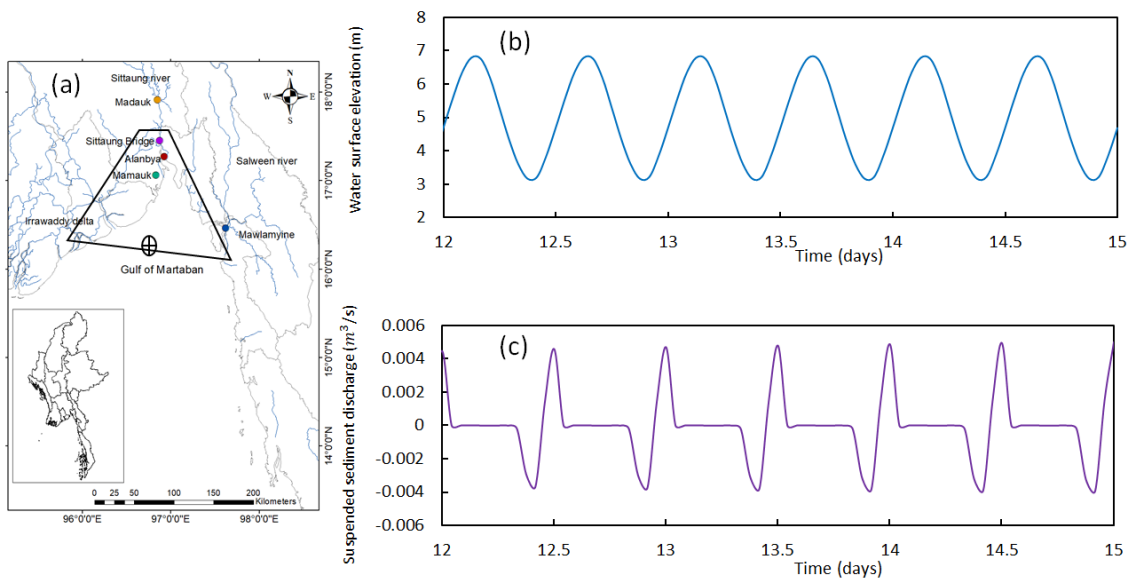


Figure 4.1 (a) The computation domain for computing bed evolution in the estuary, temporal changes of (b) computed water surface elevation and (c) suspended sediment discharge at the downstream boundary

Figure 4.1 shows the computation domain, tidal motion and suspended sediment discharge at the downstream boundary. The computation domain is shown using black lines in Figure 4.1a. Flood and ebb tides at one point on the downstream boundary is seen

in Figure 4.1b. Temporal change of suspended sediment discharge at the same point on downstream boundary is illustrated in Figure 4.1c. It shows that suspended sediment discharge along seaward and landward direction balances each other.

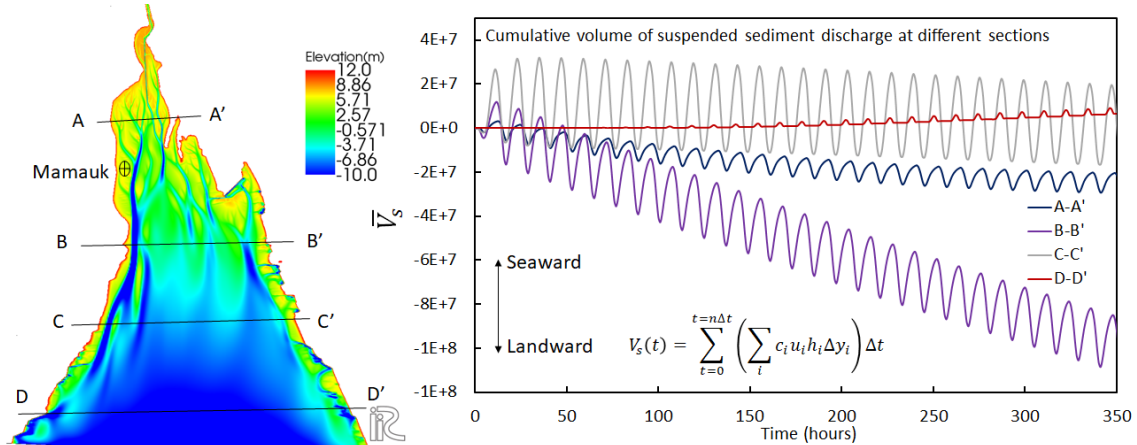


Figure 4.2 Cumulative volume of suspended sediment at different cross-sections

Temporal change of cumulative volume of suspended sediment discharge is investigated to understand movement of suspended sediment flux at different locations. Figure 4.2 illustrates the cumulative volumes of suspended sediment discharge at different cross-sections. At the A-A' cross-section, the cumulative volume of suspended sediment discharge is towards the landward direction and a very strong flux of suspended sediment discharge towards the landward direction is observed at B-B'. In addition, at C-C', it is directed seaward and near the boundary, at D-D', it is nearly balanced. The huge influx of suspended sediment at location B-B' may contribute largely to the delta formation process in the estuary.

Percent of bed load and suspended sediment in total sediment transport is understood through estimating ratio of bed load and suspended sediment. Figure 4.3 illustrates the ratio of bed load and suspended load at cross-sections A-A' and B-B' in which Q_b is defined as bed load discharge and Q_s is suspended sediment discharge. It is

seen from the values that the ratio is very negligible. Due to existence of very fine sediment, bed load discharge is very negligible compared to suspended sediment. That is why major discussion relating to sediment transport characteristics is done based on suspended sediment only.

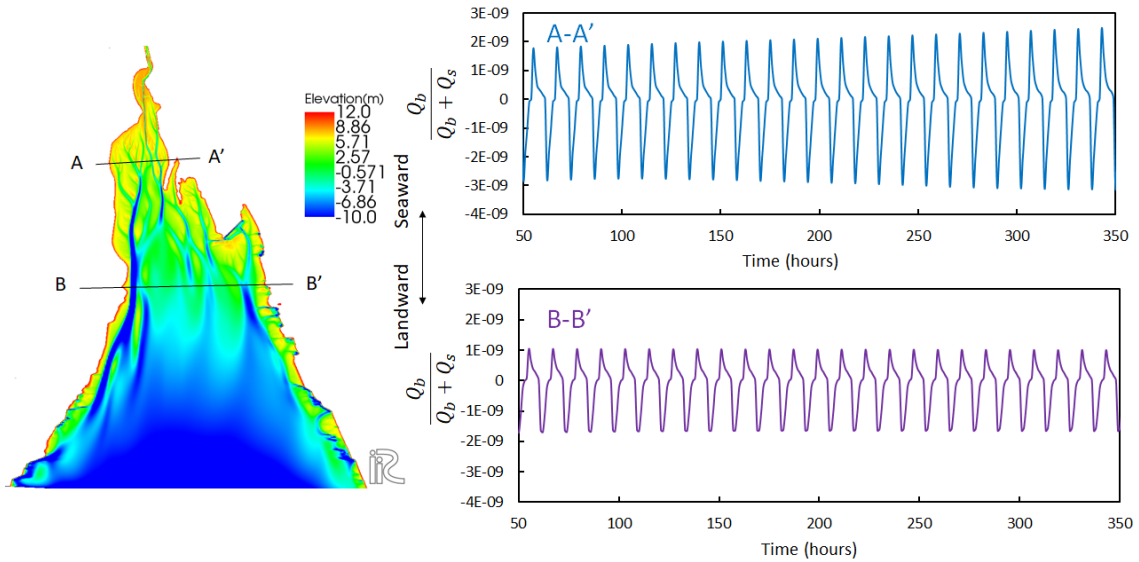


Figure 4.3 Ratio of bed load and suspended load at different cross-sections

Developing process of sand bars, stream channel pattern and channel bifurcations are investigated precisely. Figure 4.4a-c shows developing process of sand bars and stream channel pattern reproduced after the computations of five, ten and fifteen days for Case 3. Channel bifurcations are observed at upstream of Alanbya. Such characteristics cause change in stream channel pattern and movement of sand bars in the estuary. Figure 4.4d-f shows such developing process after the computations of twenty, twenty five and thirty days. It is seen that near and downstream of Alanbya, new channel is formed westwards (see in Figure 4.4d,e) which then bifurcates eastwards after thirty days of computation (see in Figure 4.4f).

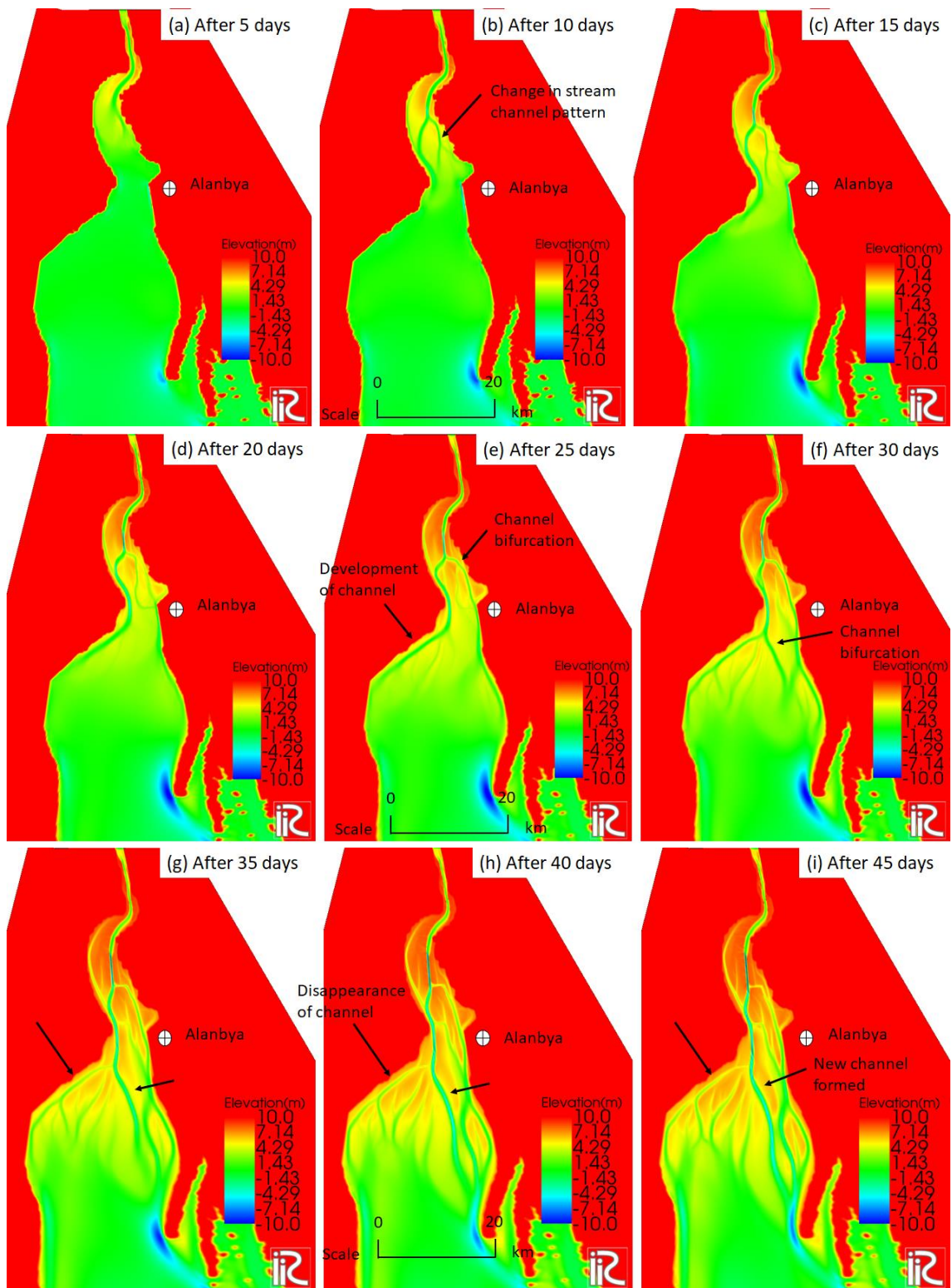


Figure 4.4 Developing process of sand bars and stream channel pattern after computations of 5, 10, 15, 20, 25, 30, 35, 40 and 45 days for Case 3

After bifurcation takes place, flow reduction takes place along old channel and flow is diverted towards the bifurcated channel as seen in Figure 4.4g-i. So it is clearly understood that channel bifurcations are reasons behind active channel change in the estuary. Figure 4.4j-l shows developing process of sand bars and stream channel pattern reproduced after thirty, sixty and ninety days of computation for case 3. Developing process of tree structure and channel combining process are seen in the figures. . Such channel merging process is very important configuration characteristic. Big sand bar develop towards the sea. Such tendency of bar formation process identifies deposition prone areas very clearly.

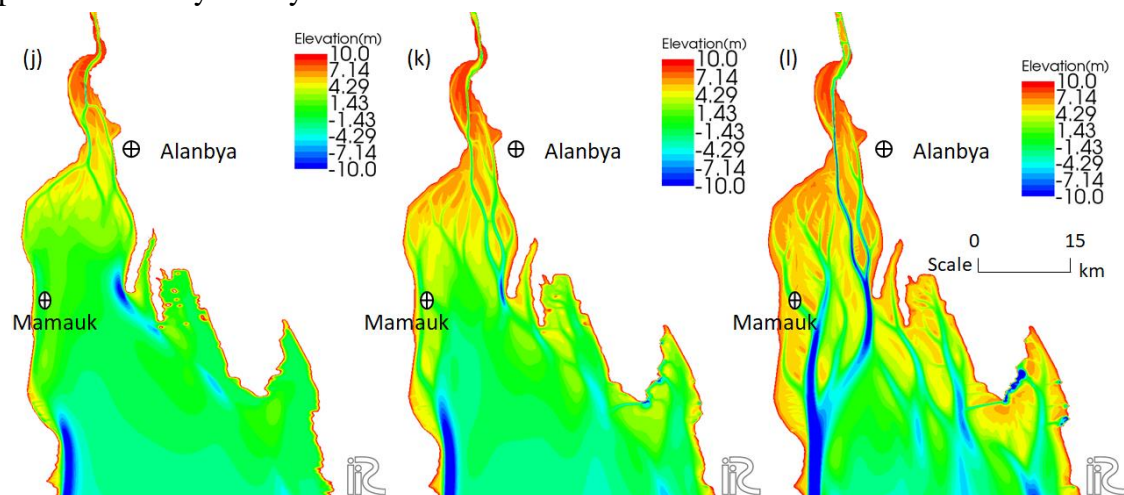


Figure 4.4 Developing process of sand bars and stream channel pattern after computations of 30, 60 and 90 days for Case 3

During bar formation, bifurcation, disappearance and closing of stream channels take place. It is suggested that elements of channel changes such as the stream channel bifurcation and channel closing are responsible for development of sand bars, and also suggested that an abrupt change of stream course must be caused by the channel bifurcation and it may cause sudden change of active eroding region. In figure 2.8 and 2.9 it is recognized that west bank of the estuary near Mamauk has been eroded severely in these 10 years and such an active erosion tends to decrease recently. In addition, it is

reported that the bank line shifting takes place cyclically from east to west and then from west to east. Such a cyclic change must be caused by the channel bifurcation.

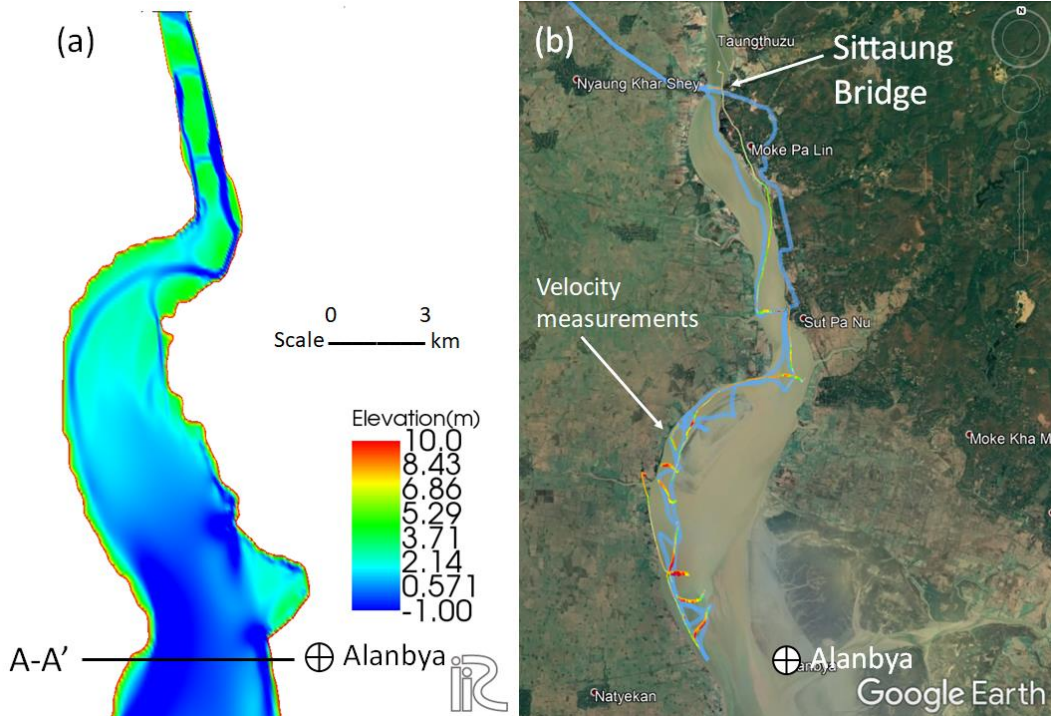


Figure 4.5 (a) Computed stream channel pattern from Sittaung Bridge to Alanbya and (b) boat tracks (travel paths) during ebb tide

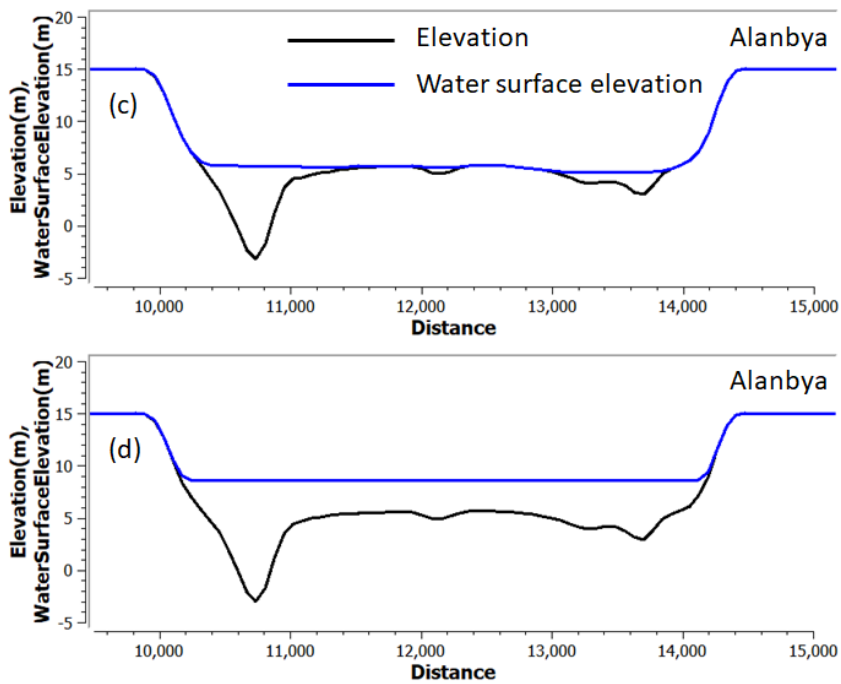


Figure 4.5 Computed water surface elevation at cross-section A-A' (shown in Figure 4.5a) near Alanbya (c) during ebb tide and (d) during flood tide

It was realized during field investigation that due to very shallow morphology, sand bars remain exposed and stream channels are narrow during ebb tide. During the field survey in 2019, the boat could not pass through the cross-section because of shallow water depth during the ebb tide. Figure 4.5 is illustrated to investigate if computed stream channels match with actual where stream channels are compared with boat tracks traveled during field investigation. Figure 4.5a shows computed stream channel pattern from Sittaung Bridge to Alanbya and Figure 4.5b illustrates the boat track and alignments for velocity measurements during field investigation. Due to very shallow depth and exposed sand bars during ebb tide, velocity and cross-sectional shape could not be measured across the whole cross-section. It is seen from Figure 4.5a,b that stream channel planform is reproduced well. In addition, computed results on bed elevation and water surface elevation during ebb and flood tides are illustrated in Figure 4.5c,d. It is seen that during ebb tide, the sand bar created near Alanbya area is exposed over the water surface, however, during the flood tide, the entire cross-section remains submerged.

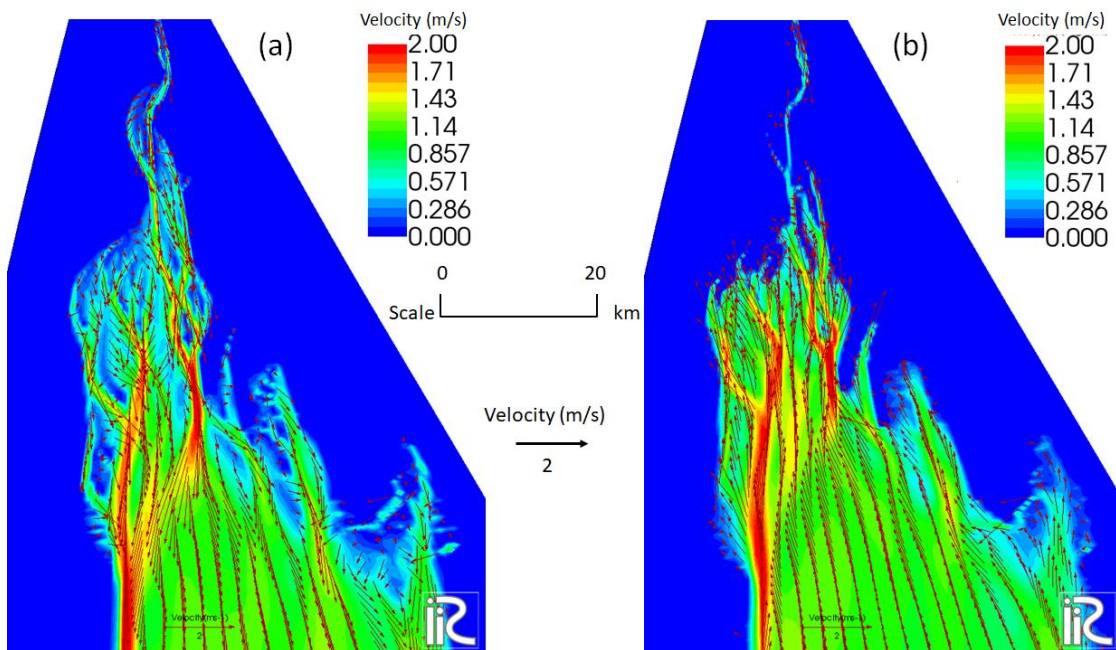


Figure 4.6 Spatial distribution of velocity at specified stages during (a) ebb tide and (b) flood tide for Case 3

Figure 4.6a,b illustrates velocity and vectors during ebb and flood tides for Case 3. Ebb and flood dominant stream channels are visible here. During ebb tide, flow is concentrated to the nearby channels. During high tide, higher velocities are observed along the channels.

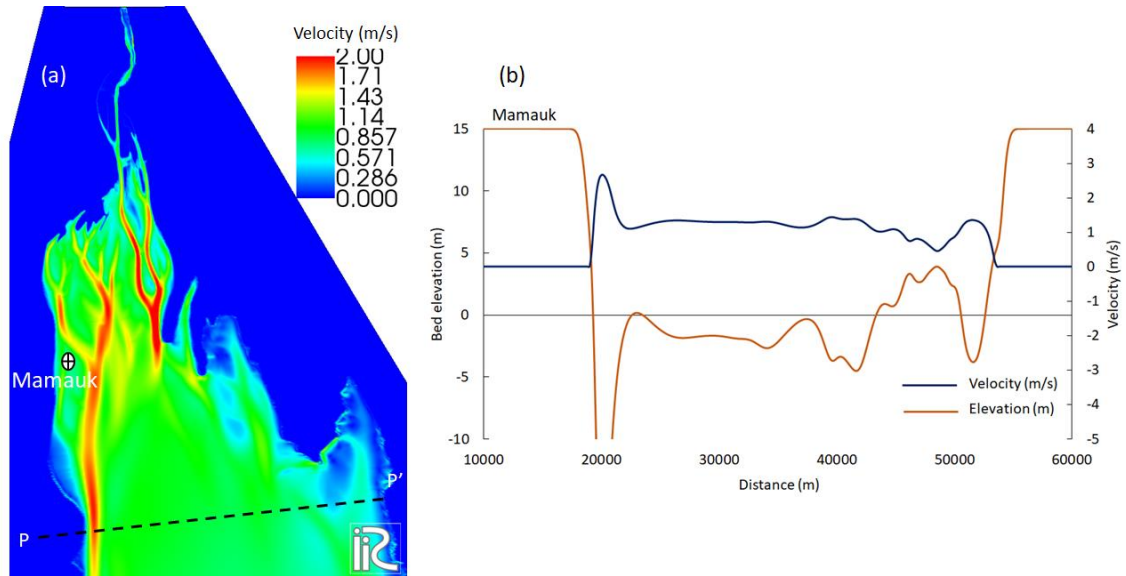


Figure 4.7 (a) Spatial distribution of velocity at specified stage during flood tide and (b) lateral velocity profile and bed elevation across the cross-section P-P' for case 3

Figure 4.7a shows velocity during flood tide and Figure 4.7b shows lateral bed configuration and the lateral velocity profile at the cross-section P-P' (see Figure 4.7a). The results show that velocity of around 3 m/s is reproduced along the deep channel, whereas smaller velocity is exhibited over the shallower parts. So, the created morphology influences flow pattern very much. Such flow pattern causes sediment transportation, sand bar migration and corresponding channel changes in the estuary.

Figure 4.8a shows numerical results of velocity at one specified stage of ebb tide, Figure 4.8b shows bed evolution for case 3 and Figure 4.8c extracts satellite image of April, 2019 during low tide. It is seen that high velocity areas appear in the deep zones of stream channel, and thus the spatial distribution of velocity is reflected by stream channel

pattern. The results illustrated in Figure 4.8a,b,c shows that the channel pattern is well reproduced numerically.

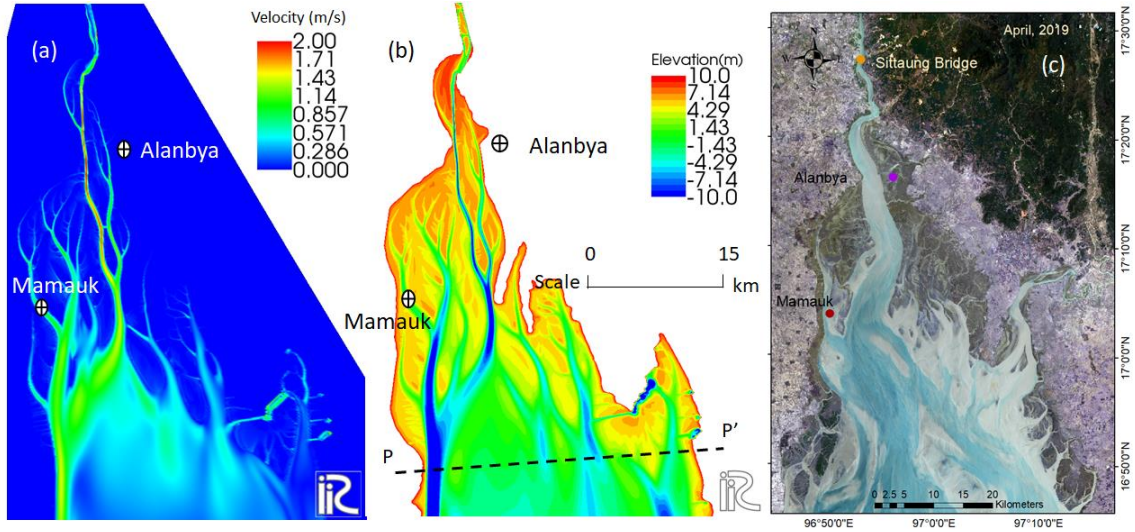


Figure 4.8 (a) Velocity distribution at one specified stage during ebb tide, (b) bed evolution for Case 3 and (c) Landsat 8 satellite image on April, 2019

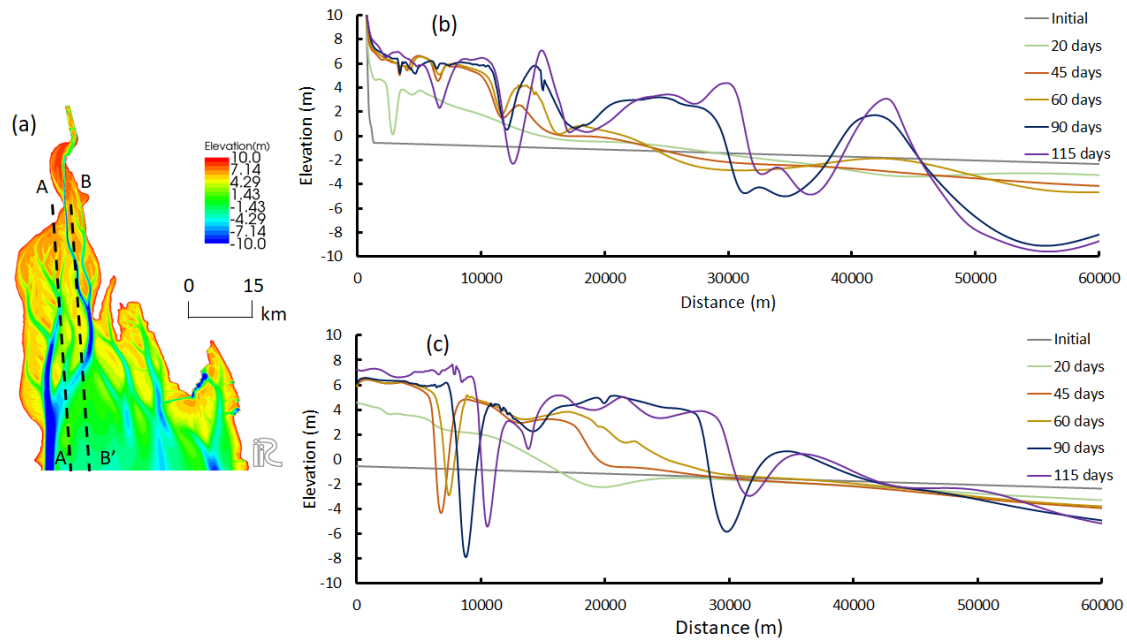


Figure 4.9 Temporal changes in bed elevation along the longitudinal sections denoted by A-A' and B-B' for Case 3

Changes in bed elevation are investigated to check equilibrium state of bed evolution and channel change in the computation domain. Temporal change in bed elevation along longitudinal direction at long sections A-A' and B-B' are illustrated in Figure 4.9. Figure

4.9a shows the locations of the long sections. Figures 4.9b,c shows computed results of change in bed elevation at A-A' and B-B' for Case 3. Change in bed elevation is computed from the flat bed condition at initial stage. It is seen that after 90 days of bed deformation analysis, bed elevation doesn't change so much along the long sections. The change is only at local scale due to channel shifting tendency. It can be said that after 90 days of bed deformation analysis, the computation domain reaches nearly dynamic equilibrium state where bed elevation along longitudinal direction doesn't change so much temporally.

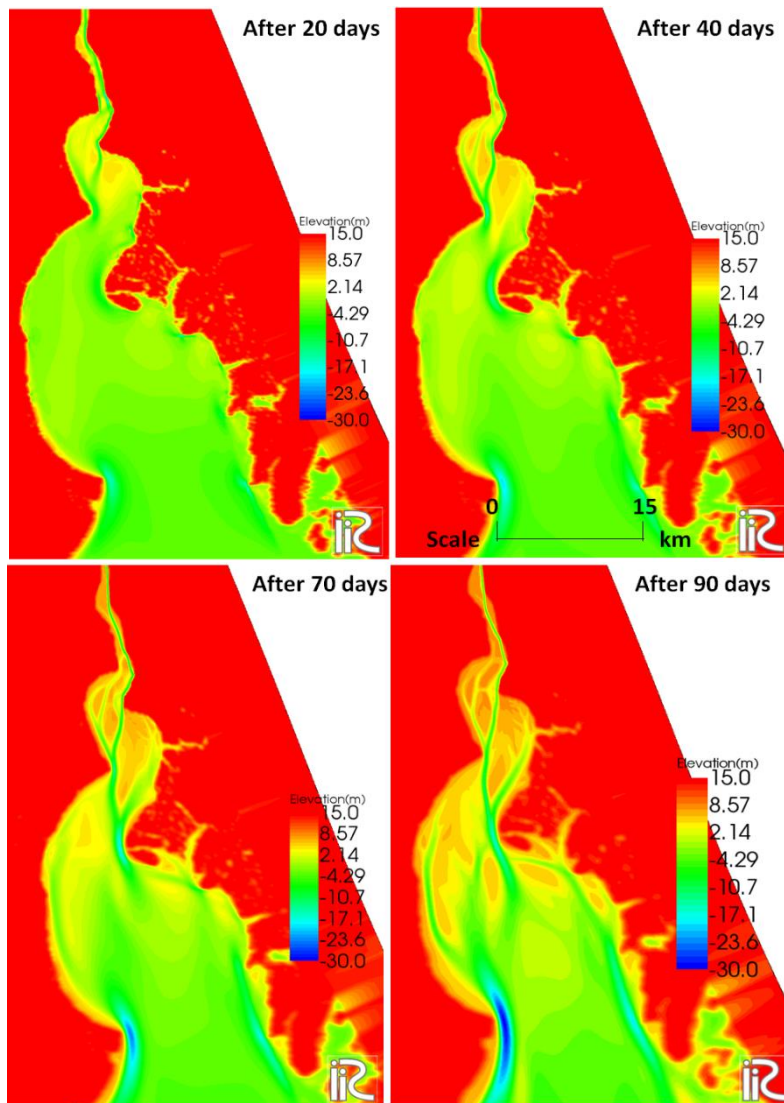


Figure 4.10 Developing process of sand bars and stream channel pattern after computations of 20 days, 40 days, 70 days and 90 days for Case 4

Figure 4.10a-d shows the numerical results on developing process of sand bars and stream channel pattern for Case 4 obtained from the computations of 20, 40, 70 and 90 days. It is recognized that the stream channel pattern and the bed morphology are created well in the estuary. Bank erosion took place actively towards the right bank till 2019 and such periodic changes are discussed in Figure 2.6 and Figure 2.7. Formation of sand bars and scour areas show similarity with the erosion and deposition prone areas on the satellite images.

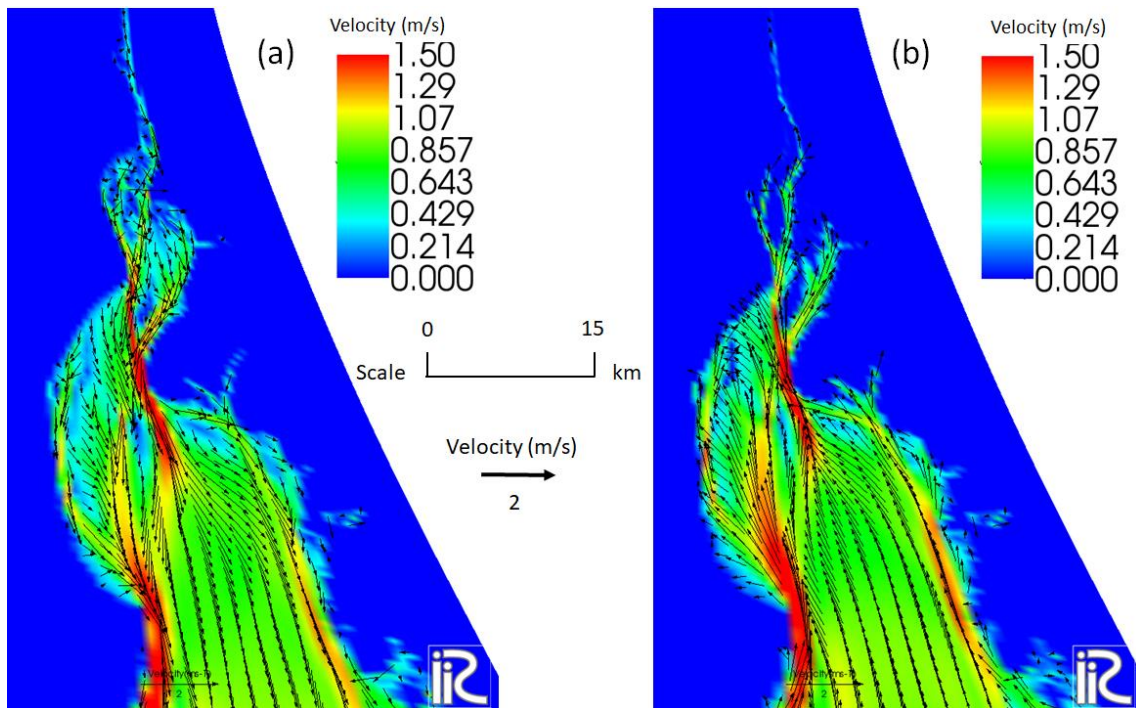


Figure 4.11 Spatial distributions of velocity at specified stages during (a) ebb tide and (b) flood tide for Case 4

Velocity and the vectors are investigated during ebb and flood tides for Case 4. Figure 4.11a,b illustrates velocity and vectors during ebb and flood tides respectively. It is seen that along the stream channels velocity vectors are stronger and high velocity is reproduced. As it is mentioned in Table 2 that Case 4 is made using the shape of estuary in February, 2017. Locations with high velocities faced severe erosion in that year, bank line retreat occurred and then the estuary took the shape in 2019 (Case 3). Now velocity

was investigated spatially and temporally for Case 4 at two different cross-sections and two different points. Locations of different cross-sections and points are illustrated in Figure 4.12.

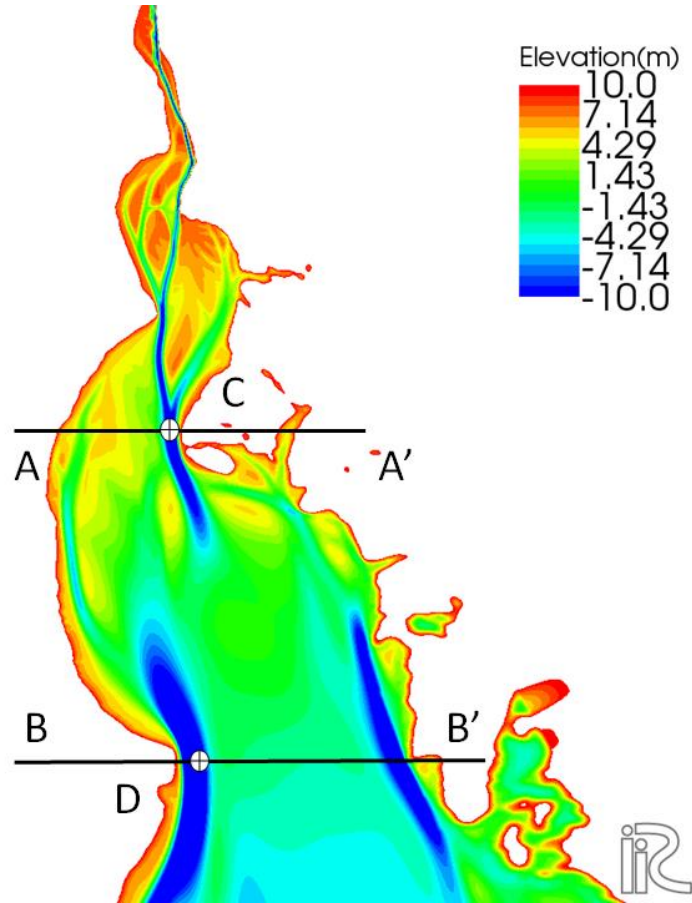


Figure 4.12 Locations of analysis of velocity at different points and cross-sections

Bed elevation and lateral distribution of velocity during ebb and flood tides at cross-section A-A' are shown in Figure 4.13a,b,c. Such lateral distribution of velocity during ebb and flood tides at cross-section B-B' are shown in Figure 4.14a,b,c. It is seen that higher velocity is reproduced along the main channels whereas lower velocity is observed at the shallow parts across the cross-sections. Two different points on these cross-sections are chosen to investigate temporal change in velocity.

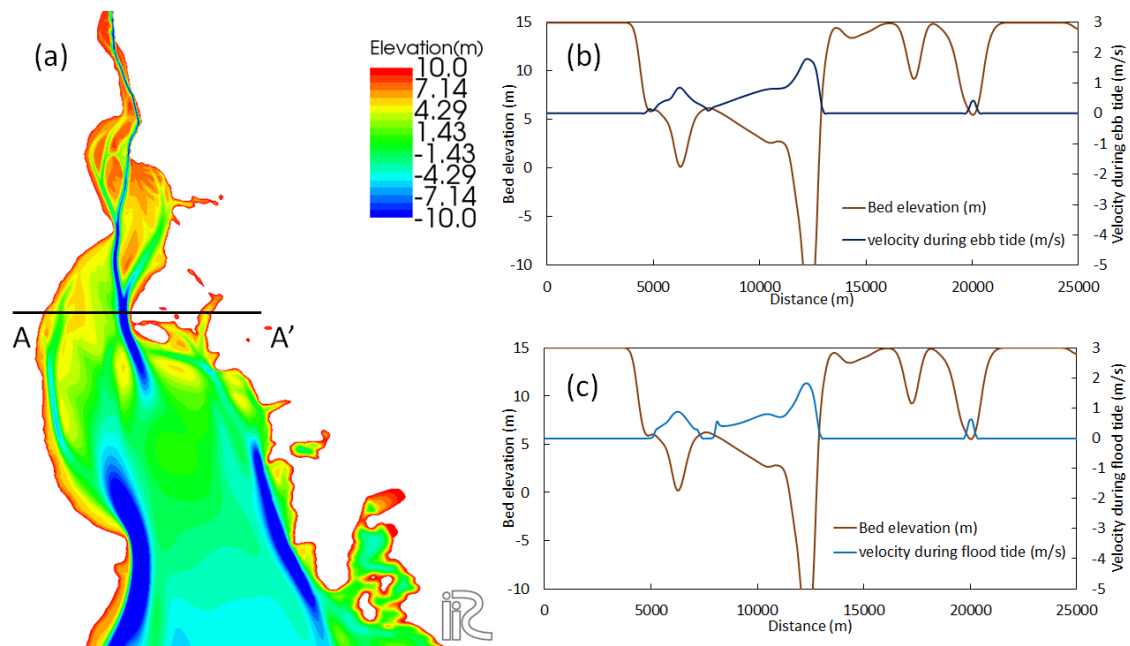


Figure 4.13 (a) Location of cross-section A-A', lateral velocity profile and bed elevation at specified stages during (b) ebb tide and (c) flood tide for case 4

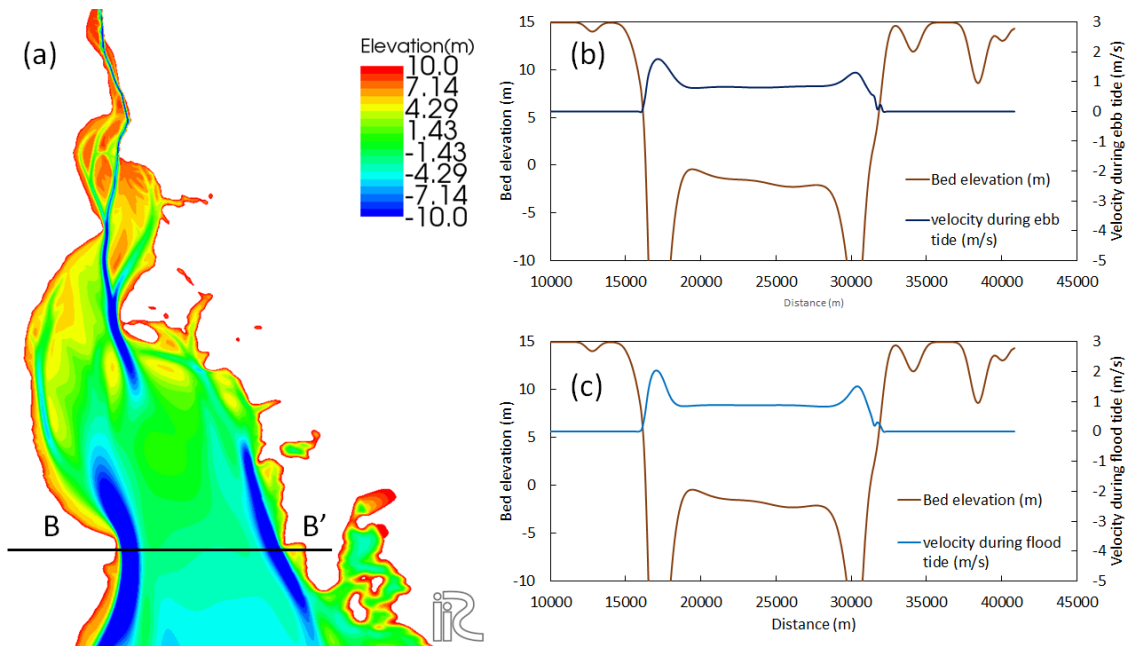


Figure 4.14 (a) Location of cross-section at B-B', lateral velocity profile and bed elevation at specified stages during (b) ebb tide and (c) flood tide for case 4

Figure 4.15a,b,c shows temporal change of velocity at points C and D. It is seen that at point C, maximum velocity reaches around 2 m/s during flood tide and around 1.8 m/s during ebb tide. However at point D, maximum velocity reaches more than 2 m/s

during flood tide and around 1.5 m/s during ebb tide. Such strong currents are observed during field investigation. Both these locations faced severe bank erosion leading to bank line retreat.

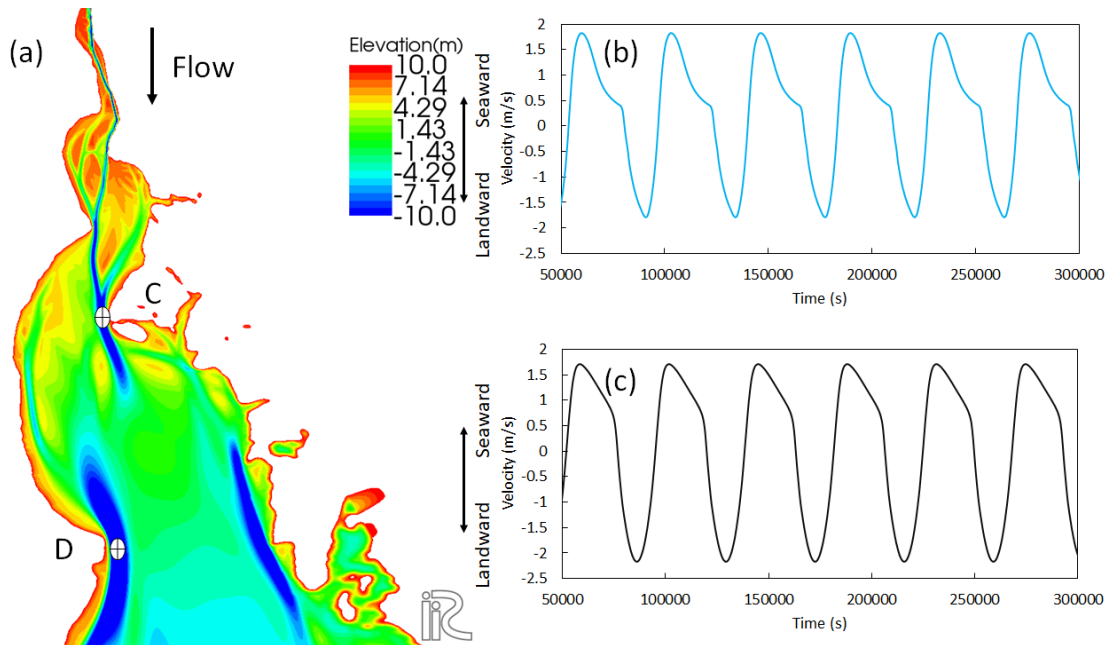


Figure 4.15 (a) Locations of points C and D; (b) Temporal change of velocity at Point C and (c) Temporal change of velocity at Point D for Case 4

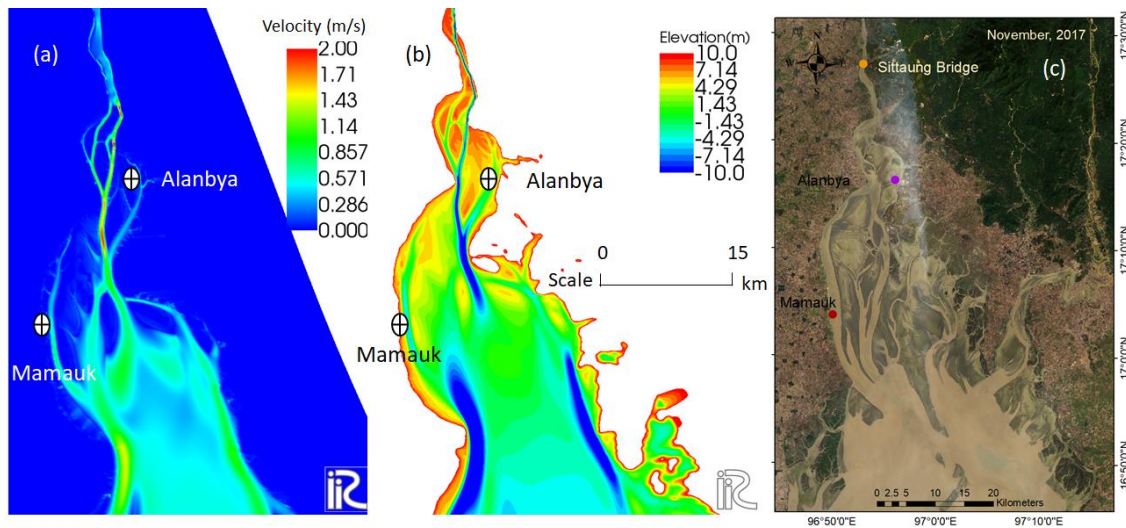


Figure 4.16 (a) Spatial distribution of velocity at one specified stage during ebb tide, (b) bed evolution for Case 4 and (c) Landsat 8 satellite image on November, 2017

Figure 4.16a illustrates velocity at one specified stage of ebb tide, Figure 4.16b,c shows bed elevation and the available satellite image during ebb tide identified on November, 2017 for Case 4. It is recognized that the velocity distribution pattern during ebb tide reflects the computed bed morphology together with stream channels in the estuary. Numerical results show that stream channel pattern and its changes are co-related to tidal currents and sediment transportation, and that the deep streams correspond to high velocity zones where sediment transportation takes place actively. Lateral velocity distribution and corresponding bed evolution results are compared with available satellite images to show that flow patterns and sand bar formation characteristics are reproduced well that agrees to the satellite images.

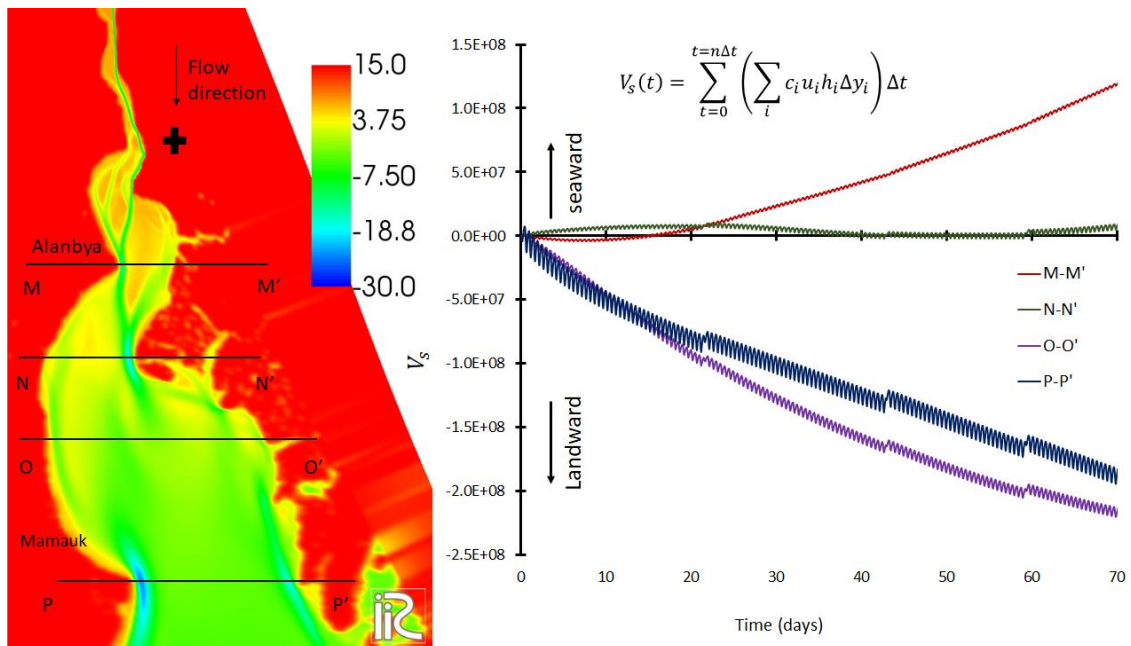


Figure 4.17 Computed cumulative volume of suspended sediment discharge at different cross-sections for case 4

Figure 4.17 shows computed cumulative volume of suspended sediment discharge at M-M', N-N', O-O' and P-P' cross-sections for case 4. The cross-sections are analyzed at the locations where severe bank erosion was observed in the last decade. It is suggested that at M-M', the cumulative volume of suspended sediment discharge is dominant

seawards and influences delta formation process in the estuary. However at N-N', suspended sediment flux both seaward and landward balance each other. At O-O' and P-P', judging from the sediment budget, sediment transportation directs landward causing accumulation and deposition of such very fine sediment at the estuary leading to formation and migration of sand bars.

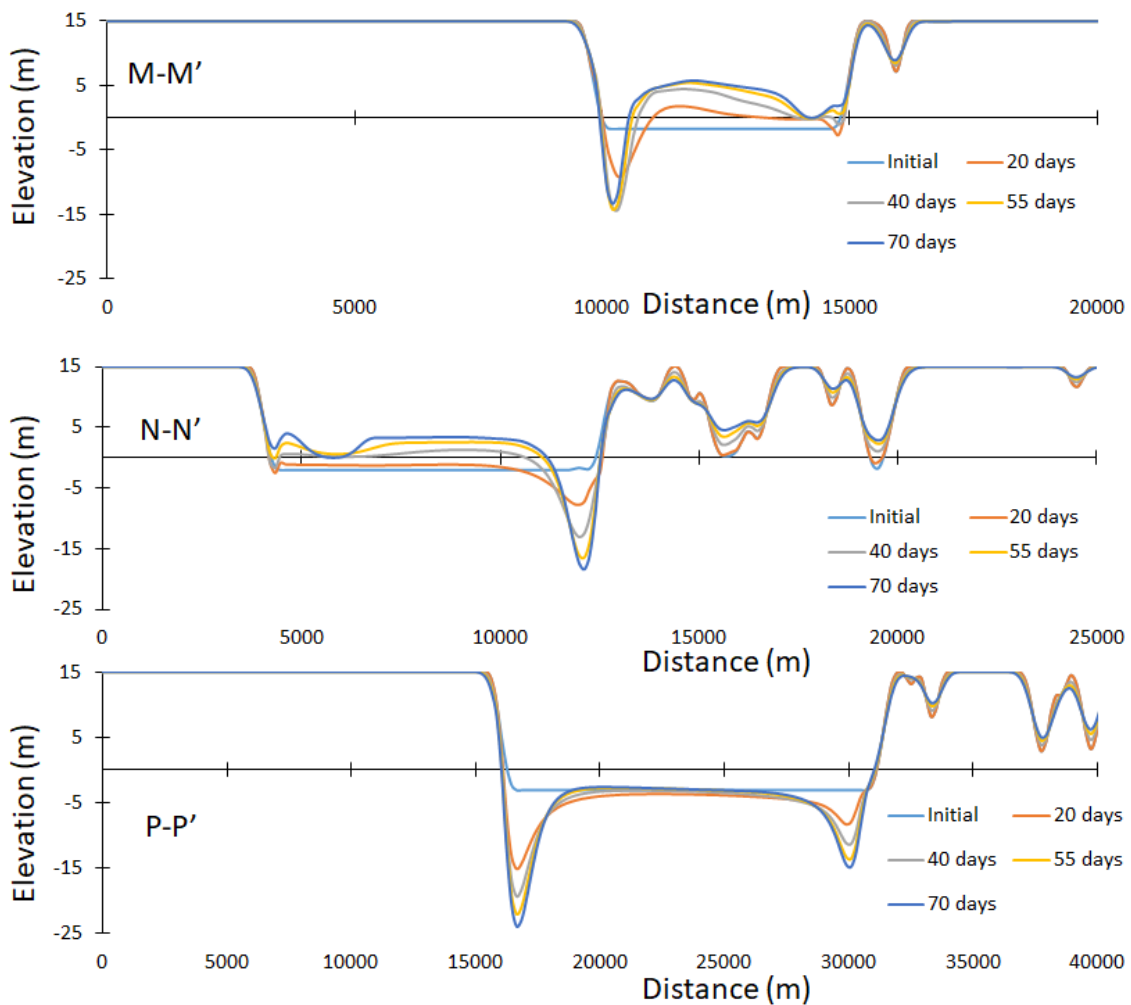


Figure 4.18 Temporal changes of lateral bed profiles different cross-sections for case 4

Figure 4.18 illustrates temporal changes of lateral bed profile at M-M', N-N', and P-P' (see Figure 4.17) cross-sections for case 4 to look at developing process of cross-sectional change in each stream. We can see most of cross-sections are deepening because lateral channel shifts don't take place according to the channel pattern shown in Figure

4.17. Figure 4.19 describes lateral distributions of unit discharge in specified stages of ebb and flood tides near Alanbya village location for Case 4. Two cross-sections named G-G' and H-H' are chosen for investigating whether there are some difference in sediment transport characteristics in between ebb and flood tides or aren't. After 70 days of computation, it is seen that at upstream of Alanbya village location, one channel is ebb dominated, however near Alanbya location, both flood and ebb dominated channels exist.

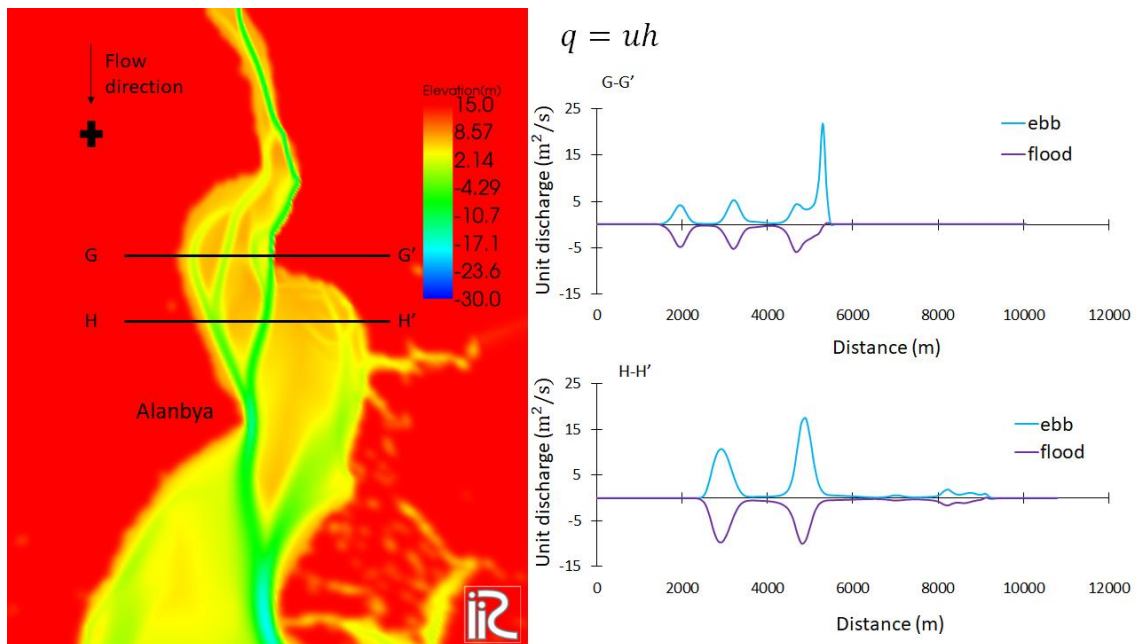


Figure 4.19 Lateral distribution of unit discharge near Alanbya at specified stages of flood and ebb tides after 70 days for case 4

Now, on the created morphology for case 3, two different types of downstream boundary conditions are employed to check the variability in sediment transport characteristics. Figure 4.20 shows two different kinds of boundary conditions; one is the constant amplitude and the other is the varied one. Temporal changes of suspended sediment discharge at different cross-sections on case 3 after employing different boundary conditions are illustrated in Figure 4.21. On the index map, the locations of cross-sections A-A', B'B' and C-C' are shown. The equation based on which suspended sediment discharge is calculated is also illustrated in the figure.

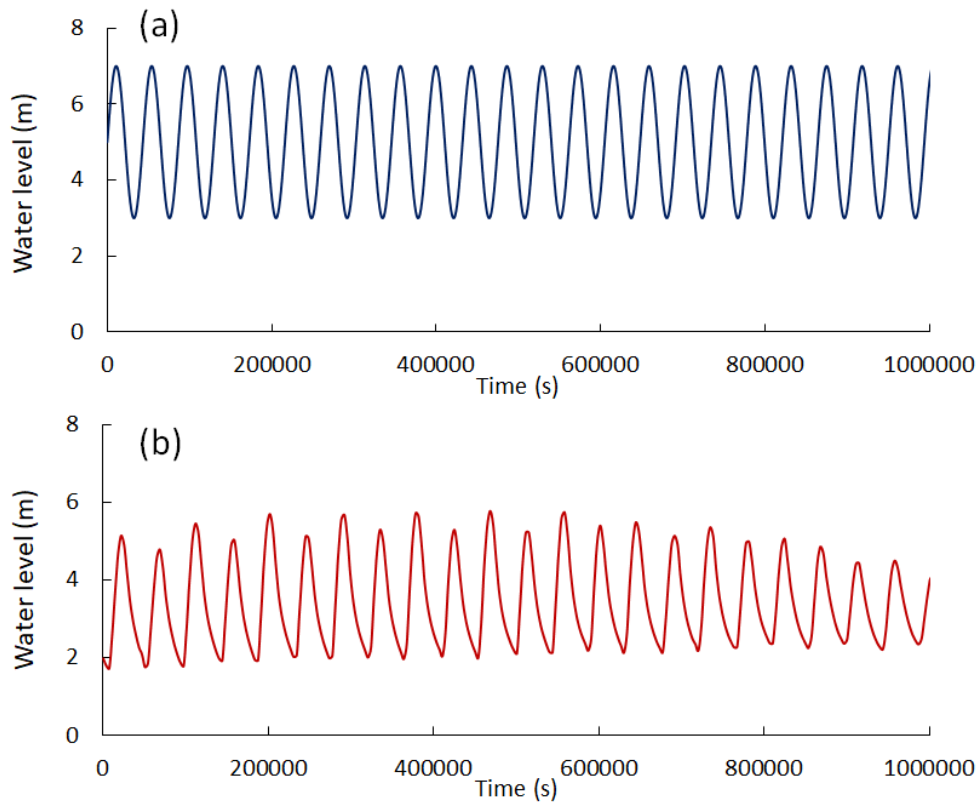


Figure 4.20 Downstream boundary employed as (a) constant amplitude and (b) varied amplitude

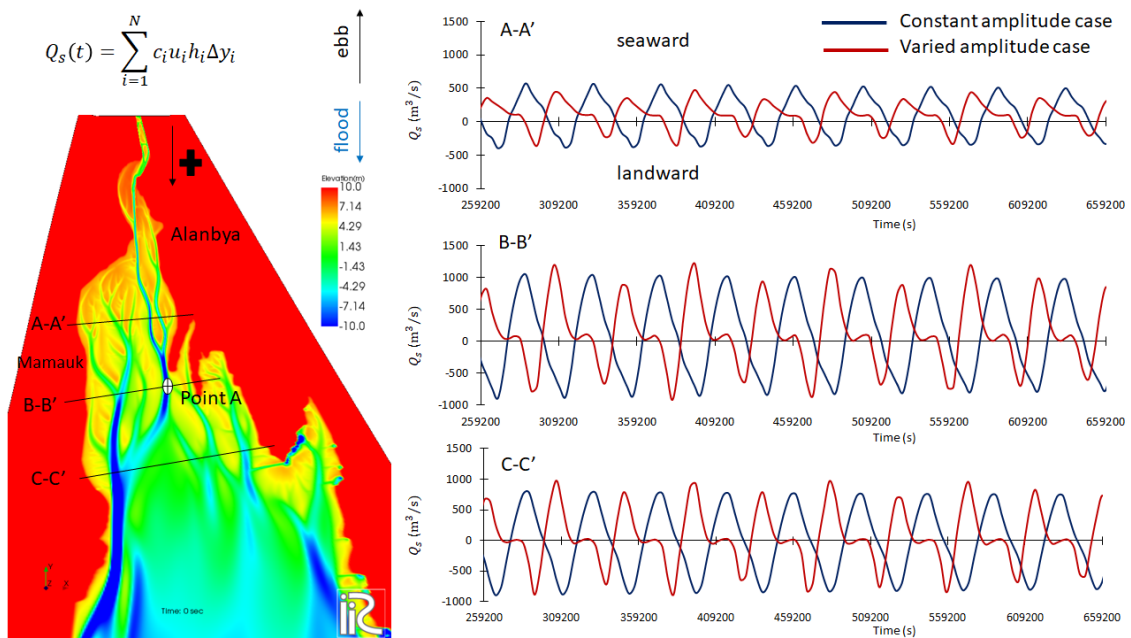


Figure 4.21 Temporal changes of suspended sediment discharge at different cross-sections

It is seen from the illustrations that across A-A', suspended sediment discharge is higher for boundary condition employed as constant amplitude compared the varied amplitude case (see Figure 4.20). However across B-B' and C-C', higher suspended sediment discharges towards ebb direction are observed. The higher peaks of suspended sediment discharge for varied amplitude case show such tendency.

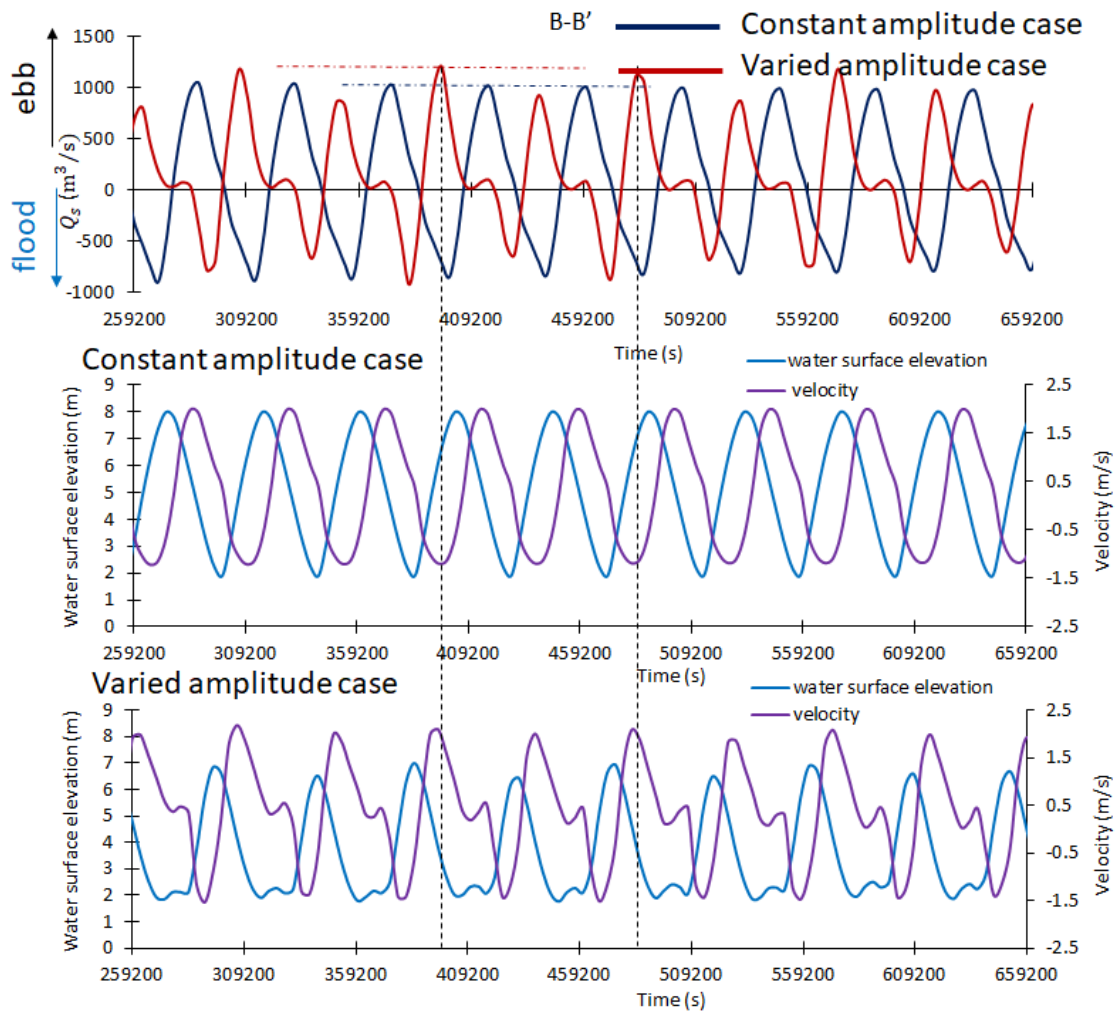


Figure 4.22 Temporal changes of suspended sediment discharge, velocity and water surface elevations at point A (see Figure 4.21)

To identify the reason behind such higher suspended sediment discharge across B-B', temporal change of computed velocity and water surface elevation are investigated at point A (shown in Figure 4.21) for cases, and illustrated the results in Figure 4.22. It is seen from the comparison of computed velocity and water surface elevation that, for

varied amplitude case, water surface elevation faces drawdown due to changes in downstream boundary and the computed velocity becomes higher. As the water surface elevation draws down, so water needs to pass through lesser cross-sectional area that produces higher velocity leading to higher suspended sediment discharge during ebb tide. So, it is realized that when varied amplitude is employed as downstream boundary condition, water surface elevation draws down for smaller tidal ranges that leads to higher velocities along the channels leading to higher suspended sediment discharge with ebb currents.

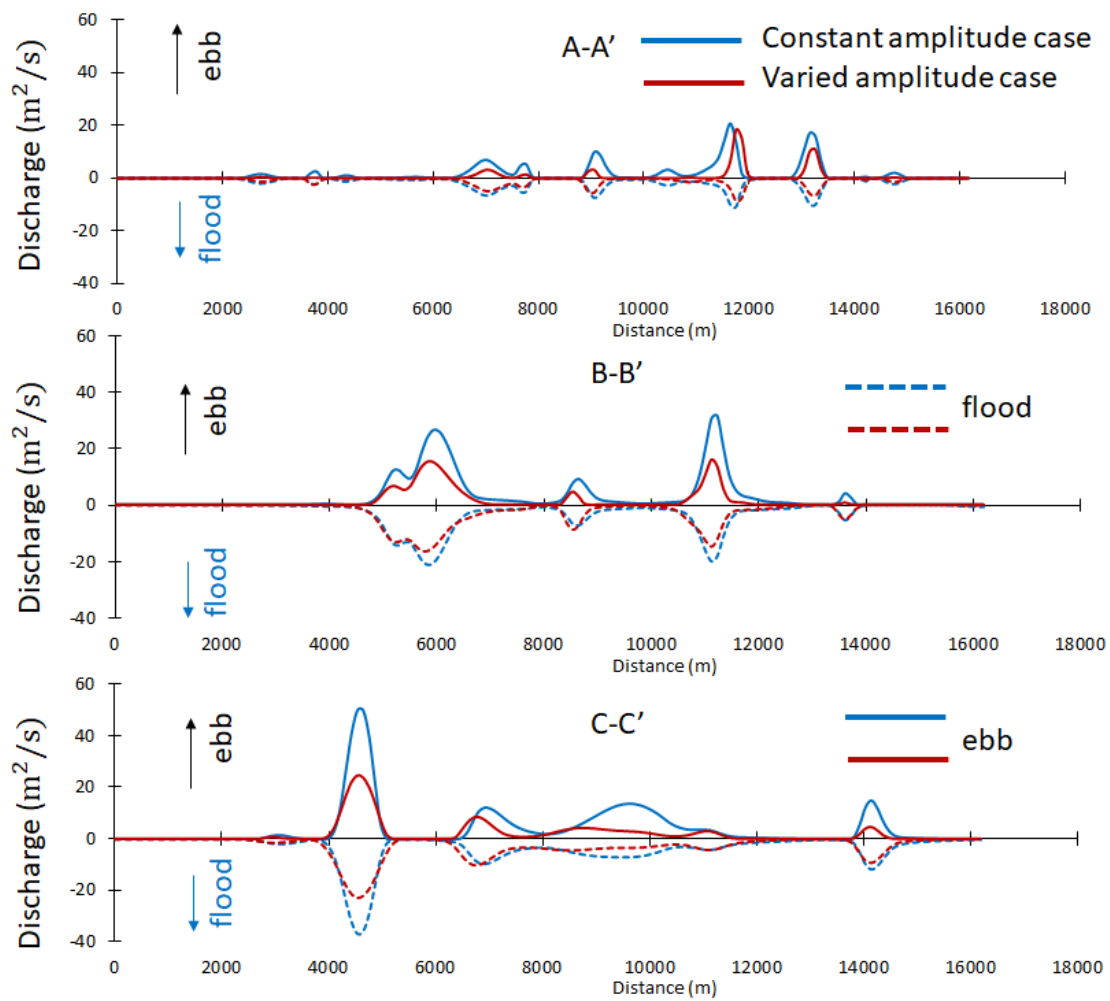


Figure 4.23 Lateral distribution of unit discharge at different cross-sections

Figure 4.23 illustrates lateral distributions of unit discharges at different cross-sections A-A', B-B' and C-C' shown in Figure 4.21. It is realized that at downstream across B-B' and C-C', for the boundary conditions of constant and varied amplitudes, both the flood and ebb flows dominate the channels. However across A-A', mostly the ebb flows dominate. It is suggested that stream channels near Mamauk are mostly influenced by both flood and ebb tidal currents.

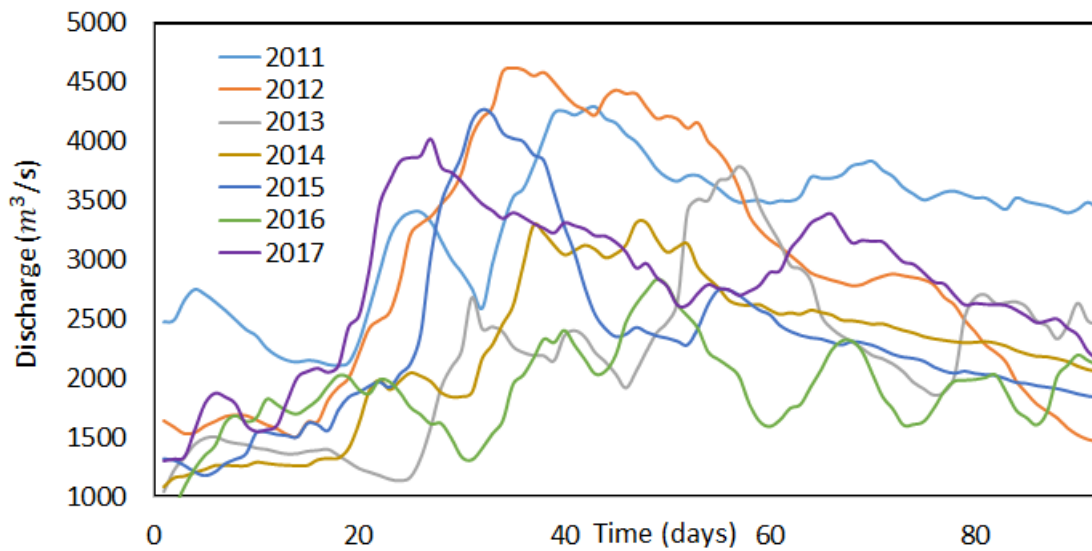


Figure 4.24 Daily discharge hydrograph from July to September in recent years

Numerical simulation of bed deformation is conducted for 90 days with constant flood discharge in the upstream boundary. The meaning of duration of computation with respect to the actual phenomena is quantified here. Figure 4.24 illustrates daily discharge hydrographs during the monsoon (July to September) in recent years. It is seen that average daily discharge increases from around 1000 m³/s to more than 4000 m³/s and again reduces to the dry season flow during this time period. Constant discharge of 3000 m³/s for 90 days was employed at the upstream boundary. This means total supply

discharge volume of $2.33 \times 10^{10} \text{ m}^3$ during the computation time period. Now the ratio of computed total discharge volume to observed ones from July to September in recent years are shown in Table 3. It is found that nearly similar volume of discharge passed from the upstream boundary. It is concluded that average one year flood is simulated with 90 days of constant flow discharge from the upstream boundary.

Table 3 Computed and observed volume of supply discharge at upstream boundary

Year	Discharge from Jul. to Sep. (m^3/s)	Volume (m^3)	Ratio of computed and observed volume
2017	254737	2.2×10^{10}	1.06
2016	174914	1.51×10^{10}	1.54
2015	213096	1.84×10^{10}	1.27
2014	205872	1.78×10^{10}	1.31
2013	200194	1.73×10^{10}	1.35
2012	267273	2.31×10^{10}	1.01
2011	303516	2.62×10^{10}	0.88

4.3 Numerical simulation of bank erosion

Numerical simulation is conducted to reproduce bank erosion phenomena in the estuary. The bed morphology created for Case 4 is employed as the initial condition for bank erosion. Upstream and downstream boundary conditions are the same as those in Case 2, which is shown in Table 1. Bank erosion model proposed by Biswas et al. (2016) is employed here. The method focuses on the influence of lateral bed slope on the erosion and deposition rate of suspended sediment, as well as on the profile of lateral bed load transport, assuming that geometric similarity holds in the bank region. In the proposed

model, the erosion and deposition rates can be evaluated using either the bed shear stress at a reference location or the average bed shear stress in the bank region. In order to simulate bank erosion and associated bank shifting with a depth-integrated-base treatment, stretchable grids were added to the conventional coarse grid system near the bank (Biswas et al., 2016).

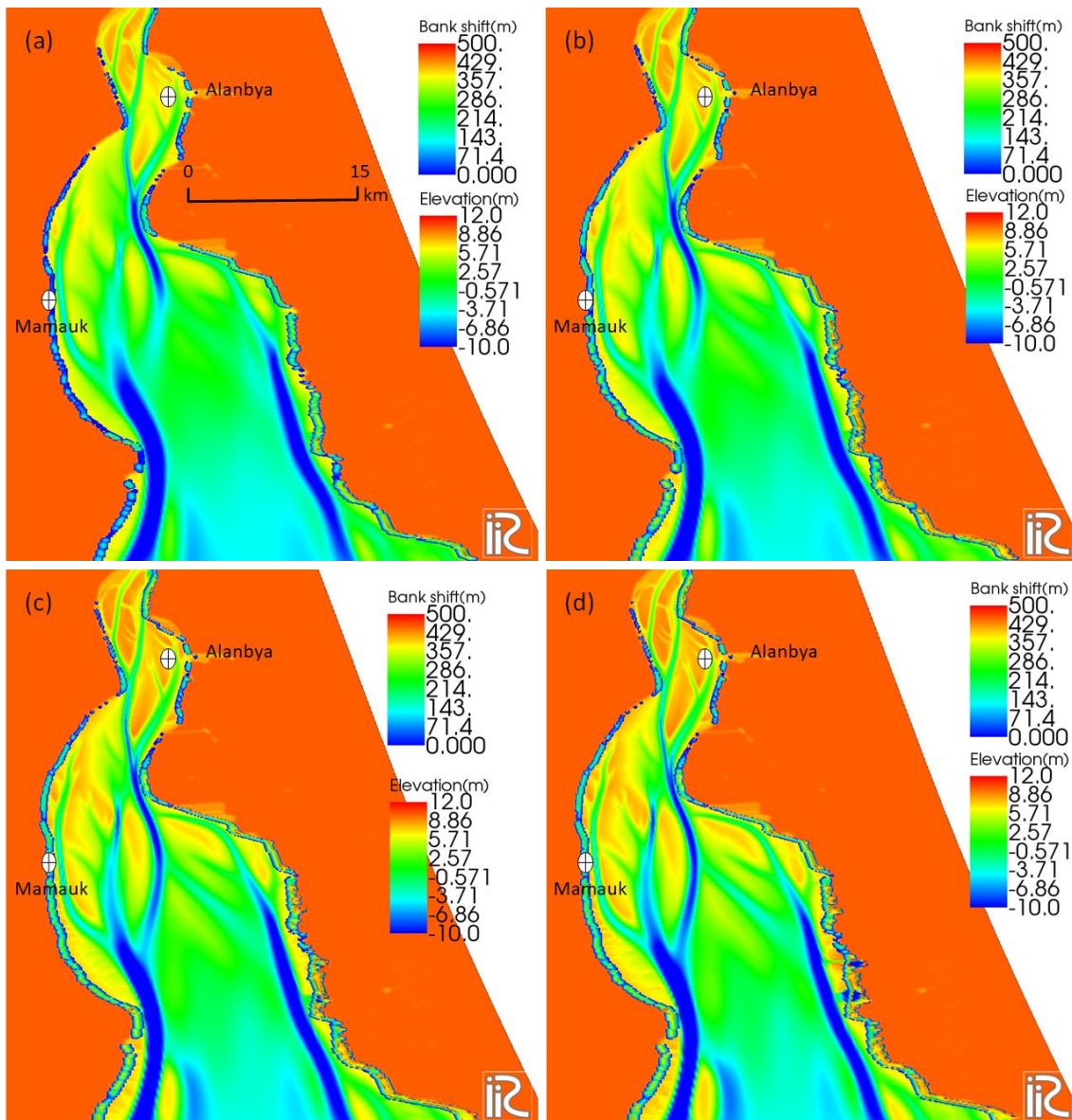


Figure 4.25 Bank line shift and bed elevation after computations of 4 days, 10 days, 18 days and 23 days

Tidal currents, sediment transportation, sand bar evolution and bank erosion are computed up to 23 days. The purpose was to check if the model can or cannot simulate the bank erosion phenomena in the estuary. As described in Chapter 3, bank erosion rate at the most active region was investigated through satellite image analysis and field investigation. Based on such analysis, it was found that bank line retreat occurs at a rate of 100 m per month whole year. Such rate of bank line shift is employed in Equations 24, 28 and 29 and for approximate values of erosion rate, $E = 100 \text{ m/month}$ or $3.86 \times 10^{-5} \text{ m/s}$, velocity, $v = 1.5 \text{ m/s}$, average depth of flow, $h = 5 \text{ m}$, mass density of sediment particles and ambient fluid as $\sigma = 2.65 \text{ kg/m}^3$ and $\rho = 1.0 \text{ kg/m}^3$, the constant K is estimated as 0.00093. Now putting such value of K , the rate of bank line shift is modified in the source code. Such modification in the parameter setting was required to address the cohesion characteristics of bank materials.

Figure 4.25 illustrates bank line shifts and bed elevations after 4 days, 10 days, 18 days and 23 days of computation. As maximum amplitude of tide was employed at the downstream boundary, such tides occur around 6 days per month. The rest of the month has smaller tidal range. During maximum tidal ranges, bank erosion takes place more actively. Compared to the water level hydrograph illustrated in Figure 2.15, it might be said that 23 days of simulation can be representative of 3 to 4 months of actual bank erosion phenomena. Computed results show that bank line retreat of around 300 m is occurred near Mamauk after 18 days of simulation. In addition, severe depositions and deepening of channels are observed. Flow is concentrated at the downstream of Mamauk which area faced erosion and disappeared from the map in 2019. In addition, a shallow

channel is produced just adjacent to the bank near Mamauk which shows good agreement with actual channel pattern and bank erosion rate.

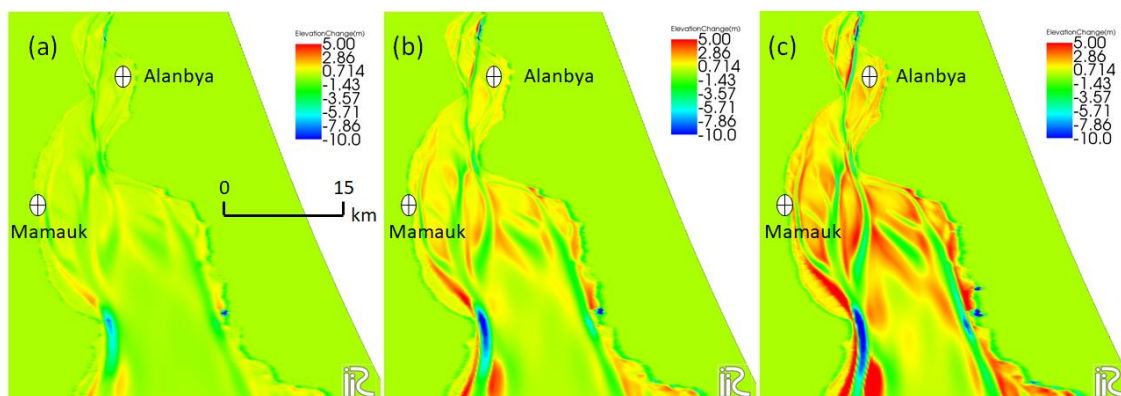


Figure 4.26 Change in bed elevation after computations of 4, 10 and 18 days with employment of bank erosion model

Figure 4.26 shows change in bed elevation after 4 days, 10 days and 18 days of computation. It is seen that stream channels are flowing westwards from Alanbya as same as actual. After bank erosion occurred, sediment transportation took place and the sand bars formation became dominant at the center of the estuary. Stream channel pattern is very clearly visible that agrees well with the satellite image illustrated in Figure 4.16c. However, several discrepancies are observed that did not match with the actual phenomena. At downstream of Mamauk, breakage of the extended part was expected, however in simulation, such breakage did not occur. In addition, bank erosion occurred at both banks, but in actual scenario bank erosion occurs only eastwards or westwards and for this particular Case 4, bank erosion was observed mainly westwards. To investigate the reason behind such severe deposition tendency near the bank at downstream of Mamauk, flow pattern and velocity vectors at flood tides and ebb tides are investigated. Figure 4.27a,b illustrate flow pattern, velocity magnitude and vectors during flood tide and ebb tide respectively. It is seen that curvature type flow is generated at downstream of Mamuk, where secondary currents are generated and such secondary

currents might have supplied sediment towards the bank region. In addition, when the flood tide reaches its peak, dead water zones are created at such corner, leading to deposition tendency near the bank.

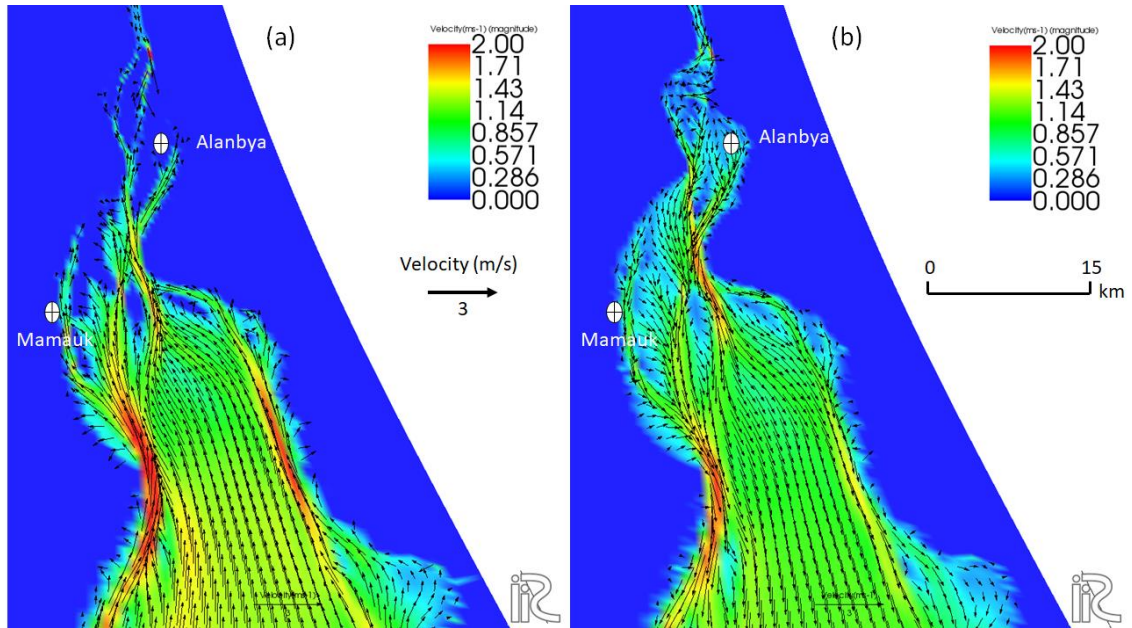


Figure 4.27 Spatial distribution of velocity at specified stages of (a) flood tide and (b) ebb tide with employment of bank erosion

4.4 Impact of spur dykes on estuary morphology

Many estuaries around the World were treated with structural interventions to attain socio-economic benefits like protection from bank erosion, improved navigability, and suitability for establishment of ports and harbors. Formation of tidal bore is a unique natural feature that is mostly influenced by the natural funnel shape of the estuary. Structural interventions influenced the characteristics of tidal bore in many estuaries around the World, too. However, putting spur dykes are considered as an option for treating bank erosion problem in the study area.

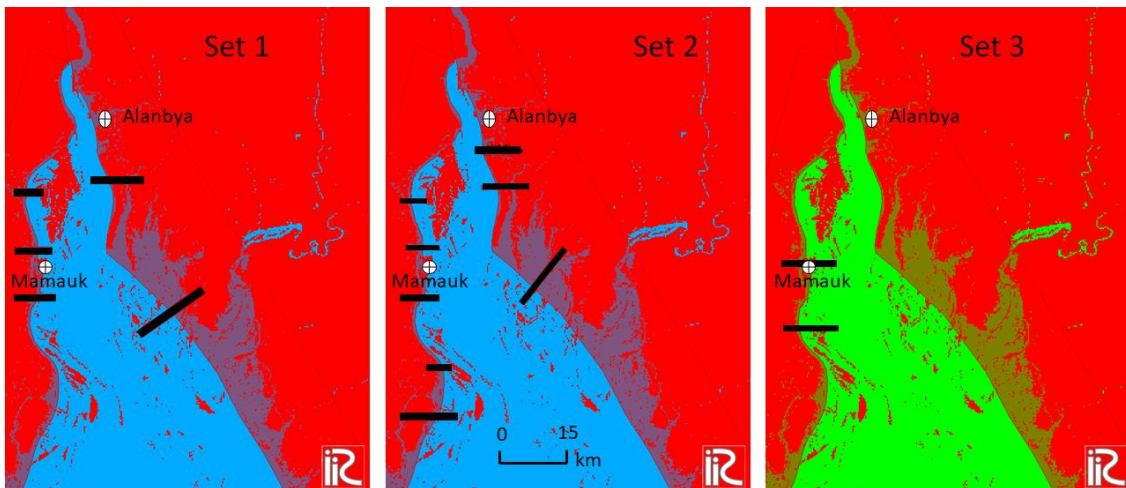


Figure 4.28 Different sets of spur dykes employed to test their influences on bed morphology

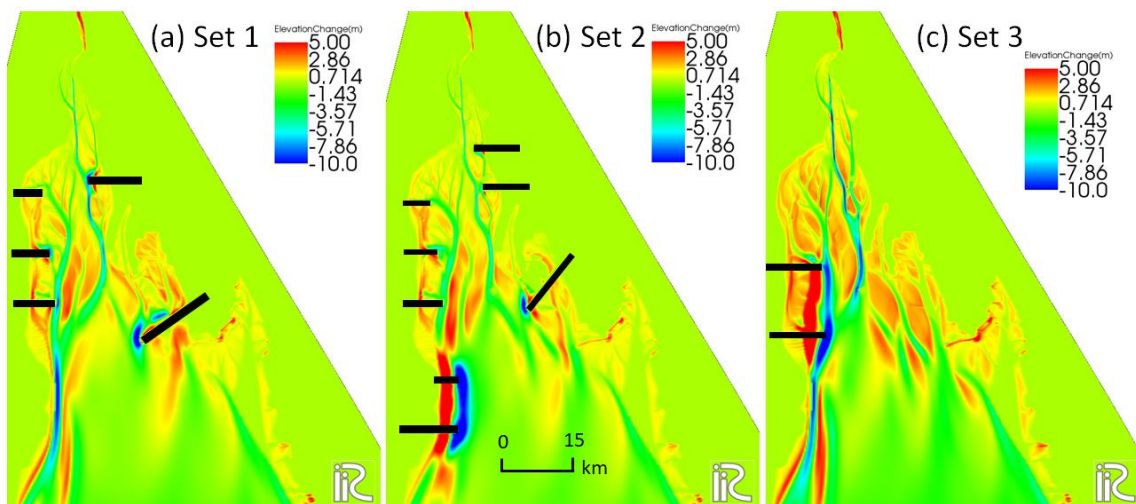


Figure 4.29 Change in bed elevation after computations of 10 days for set 1, set 2 and set 3 spur dykes

In view of the above, three sets of spur dykes are prepared for numerical simulation of tidal currents and sand bar evolution. Figure 4.28a,b,c illustrates these three sets of spur dykes. Set 1 and 2 constitute spur dykes at both banks, however Set 3 constitutes two large spur dykes at west bank only near Mamauk. The computed results of sand bar formation characteristics are discussed here. Figure 4.29 shows developed sand bars, stream channels and over-all changes in bed elevation after 10 days of bed

deformation analysis for different sets of spur dykes. Figure 4.30 illustrates the computed bed elevations from initial stage to after employment of different sets of spur dykes.

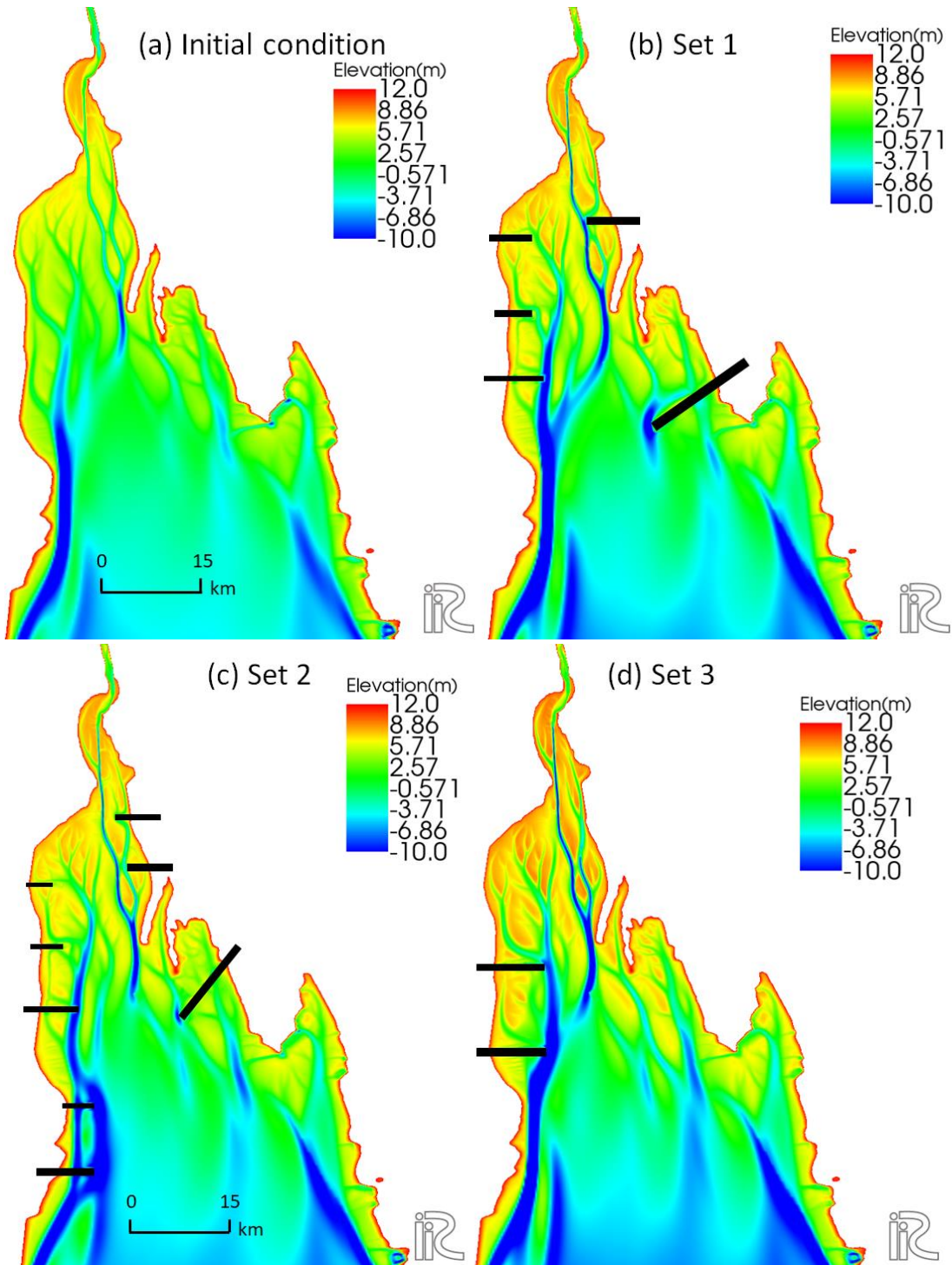


Figure 4.30 Bed elevations at initial stage, after computations of 10 days for set 1, set 2 and set 3 of spur dykes

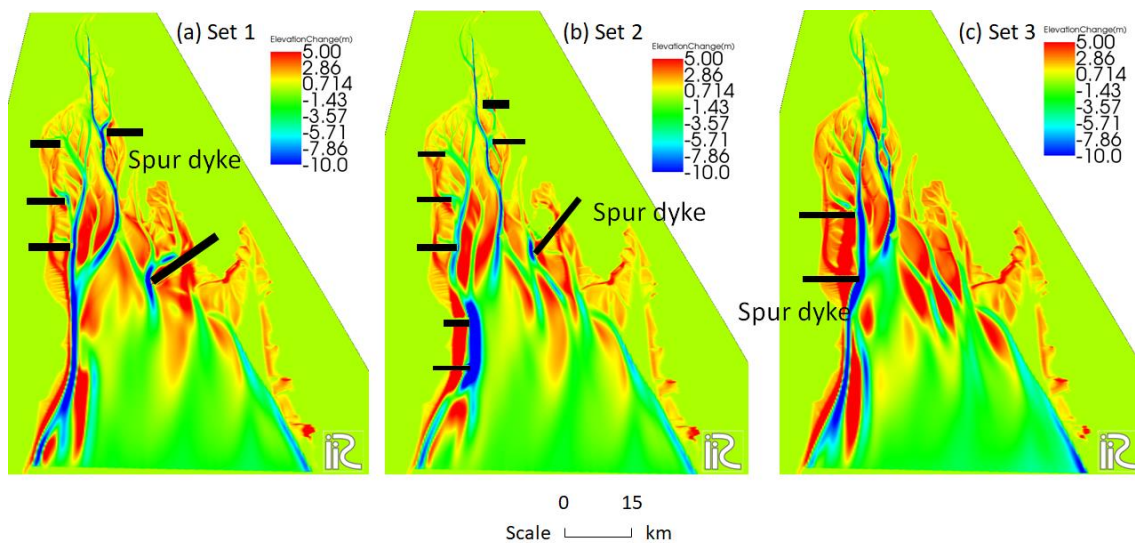


Figure 4.31 Changes in bed elevation after computation of 25 days for set 1, set 2 and set 3 spur dykes

Elongated types of sand bars are seen which are influenced by the tides and contribute to the delta formation process. Set 1 and 2 constituted spurs of smaller lengths compared to the large spurs in Set 3. It is observed that severe deposition characteristics around Mamauk are attained for Set 3. Channel deepening characters are also observed around the center of the estuary. When such analyses are continued, then deposition zones near the banks get prominent as well as deepening of channels occur along the center of the estuary. Such results are illustrated in Figure 4.31 where change in bed elevation after 25 days of bed deformation analyses are shown. It is clear that Set 3 spur might check erosion along west bank which faced severe bank erosion in recent years.

4.5 Sand bar formation processes with channel bifurcations

Analysis of satellite images in Chapter 2 displayed periodicity of bank line change on decadal to multi-decadal scale. It was also realized that such variability in channel planform was constituted by channel bifurcations. Simulation of such long term change would require very long computation hours in the existing set-up. Symmetric and asymmetric funnel shaped experimental domains are employed to investigate channel

bifurcations and lifetime of channels with and without tidal influences. Suspended sediment discharges along channels, changes in bed elevation and channel planform are investigated temporally.

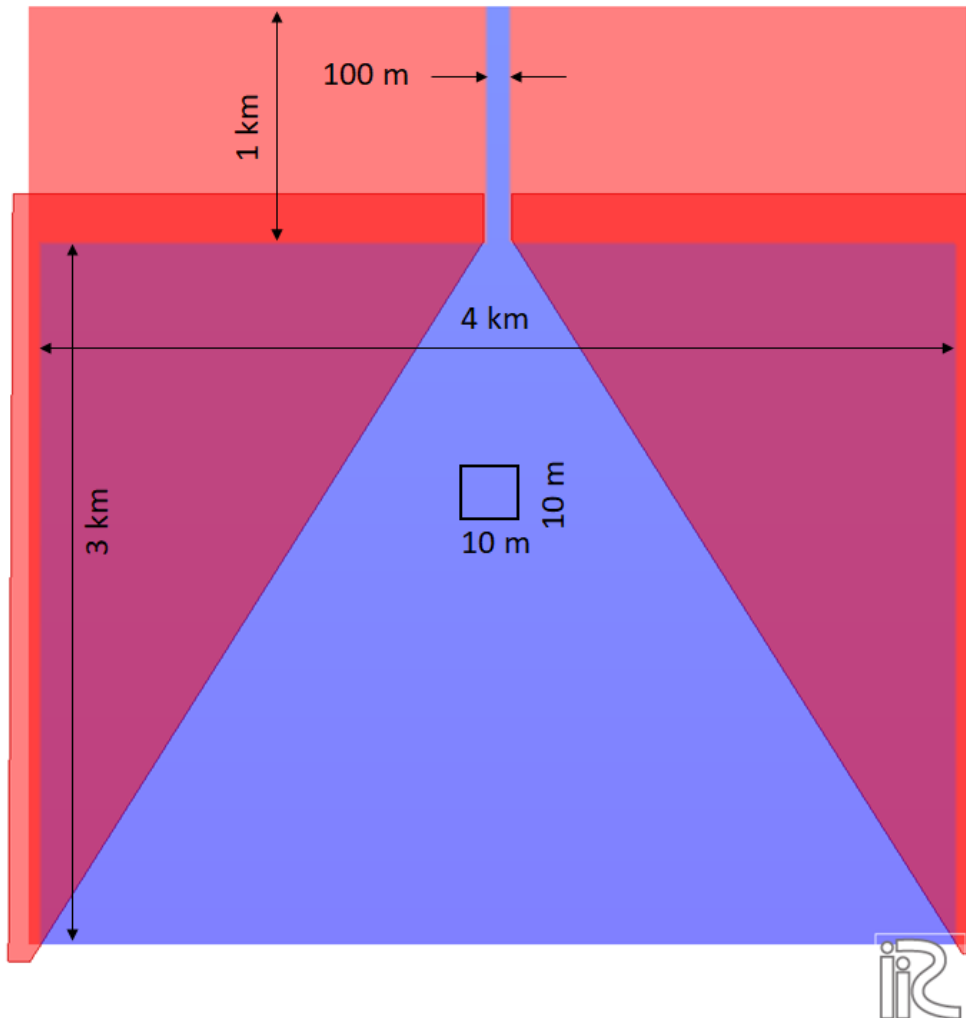


Figure 4.32 Experimental channel (symmetric shape) to simulate channel bifurcations and lifetime of channels

Figure 4.32 illustrates physical properties of the symmetric funnel shaped experimental domain. Here it is seen that the inflow channel is 1 km long and 100 m wide which empties to the funnel shaped basin which is 4 km wide at the outer boundary and 3 km long from the outfall of intake channel. Square grid size is employed with Δx and Δy as 10 m both. The initial and boundary conditions are specified in Table 4.

Table 4 Calculation conditions for symmetrical funnel shaped experimental domain

Cases	Shape of estuary	Flow discharge at upstream end, Q (m ³ /s)	Tidal motion at downstream $r = \text{Amplitude (m)}$	Initial bed slope, i_b	Grid system $\Delta x = \text{longitudinal}$ $\Delta y = \text{lateral}$
1	Symmetric funnel shaped	500	No tidal motion	$\frac{1}{10000}$	$\Delta x = 10 \text{ m}$ $\Delta y = 10 \text{ m}$
2			$T = 12 \text{ hours}$ $r = 3.5 \text{ m}$	$\frac{1}{10000}$	

Uniform flow discharge from the upstream boundary is employed with no tidal motion at the downstream boundary for Case 1, whereas uniform flow from upstream and tidal motion with 3.5 m amplitude is employed at the downstream boundary in case 2. Morphological acceleration factor is employed as 10.

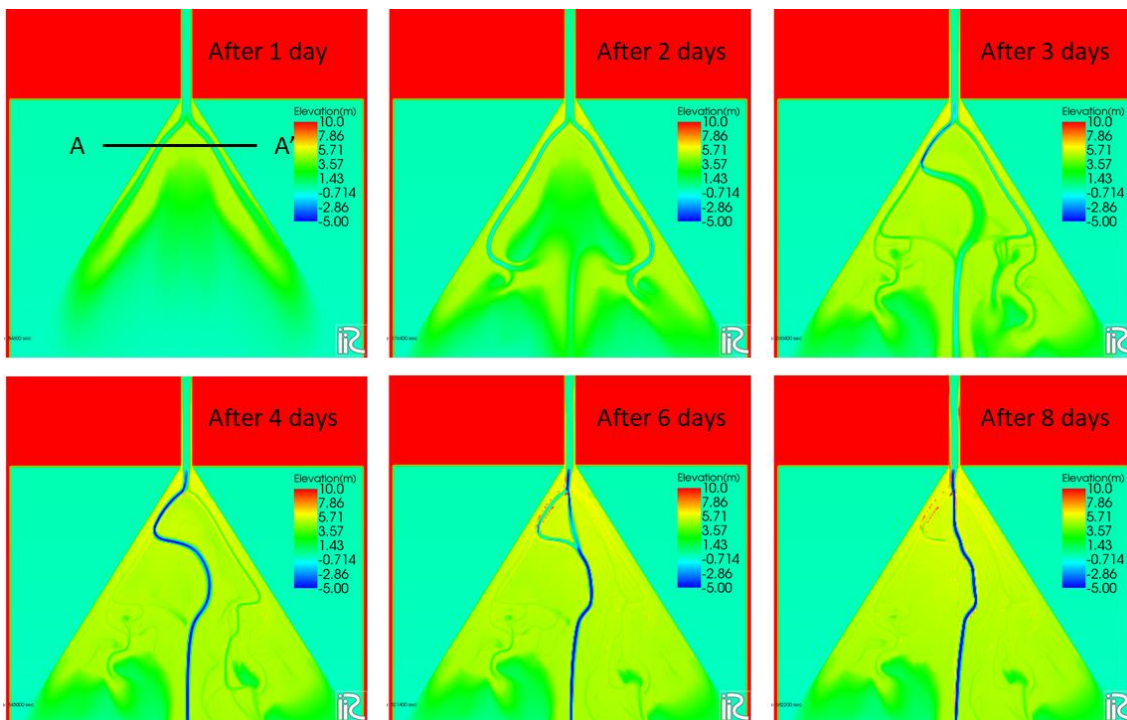


Figure 4.33 Temporal changes of channel pattern for Case 1

Figure 4.33 illustrates delta formation processes and temporal change in bed elevation for Case 1. It is seen that the main channel bifurcated into two different channels first, then gradually one channel died and flow diverted to the alternate channel. After 4

days of analysis of bed deformation, the right channel again shifted to the center and the previous path died. Such changes in bed elevation are also investigated as temporal change in cross-section at A-A'.

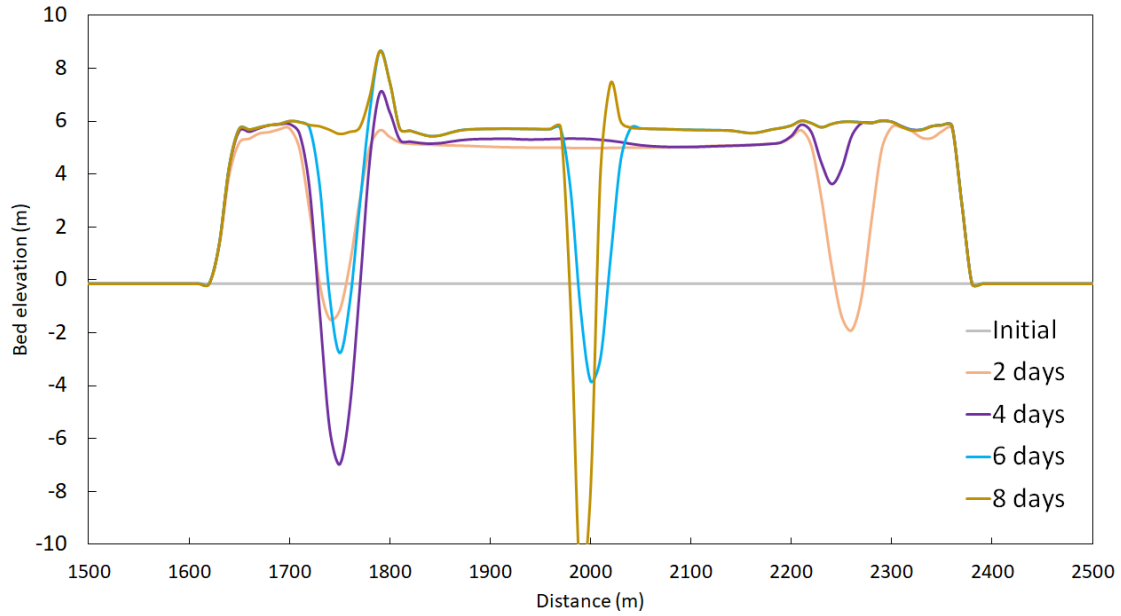


Figure 4.34 Temporal changes of lateral bed profile at cross-section A-A' (Figure 4.33)

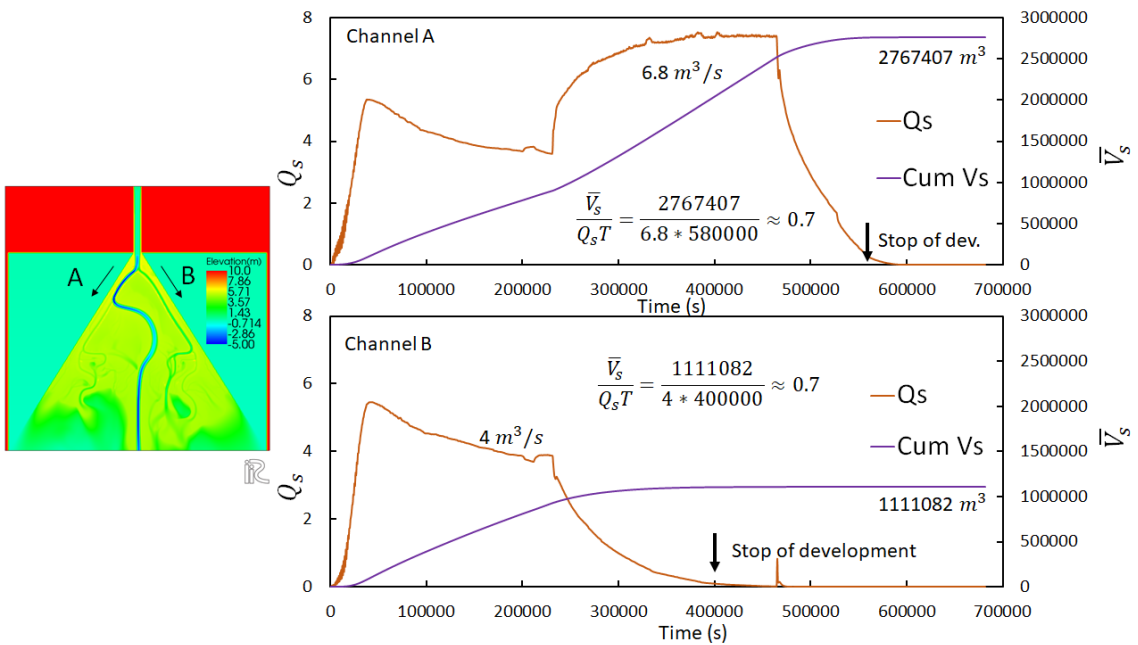


Figure 4.35 Suspended sediment discharge and its cumulated volume at different channels, A and B for Case 1

Figure 4.34 illustrates cross-sectional bed profiles to see the developing, decaying and shifting processes of channels. It is clearly seen that there used to be two identical channels near the left and right wall, then gradually the left channel died and flow got diverted to the right channel. Then on next stage the right channel died and a new channel was formed at the center.

The right channel is termed as Channel A and the left channel is termed as Channel B as shown in the index map of Figure 4.35. Using Equations 40, 41 and 42 in Chapter 3, suspended sediment discharge and cumulative volume of suspended sediment discharge are computed for channels A and B. When suspended sediment discharge goes down drastically, it shows stop of development of channel. The channel lifetime, T may be determined using Equation 42. For both the cases, the ratio of the cumulative volume of suspended sediment discharge and the product of lifetime and suspended sediment discharge is found as 0.7.

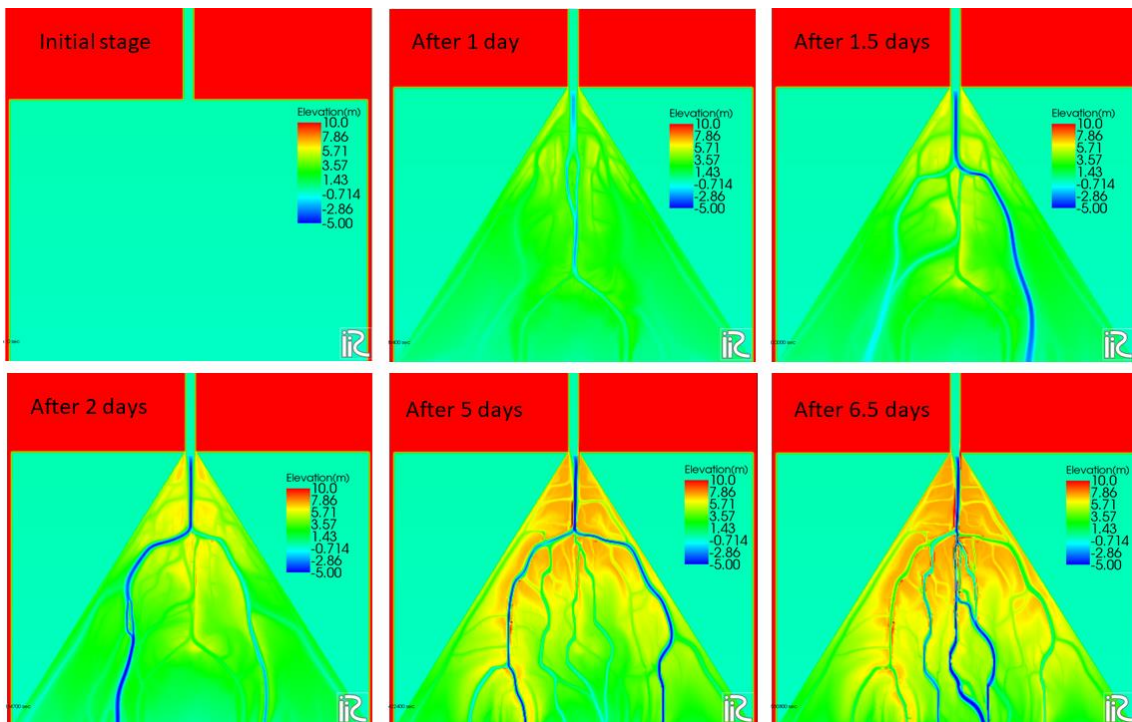


Figure 4.36 Temporal changes of channel pattern for Case 2

Figure 4.36 illustrates temporal change in bed elevation for Case 2. It is clearly seen that channel change is much rigorous and shifting from left to right bank occurs much more frequent. In addition, tidal influence brings about longitudinal shaped sand bars and presence of several active tidal channels.

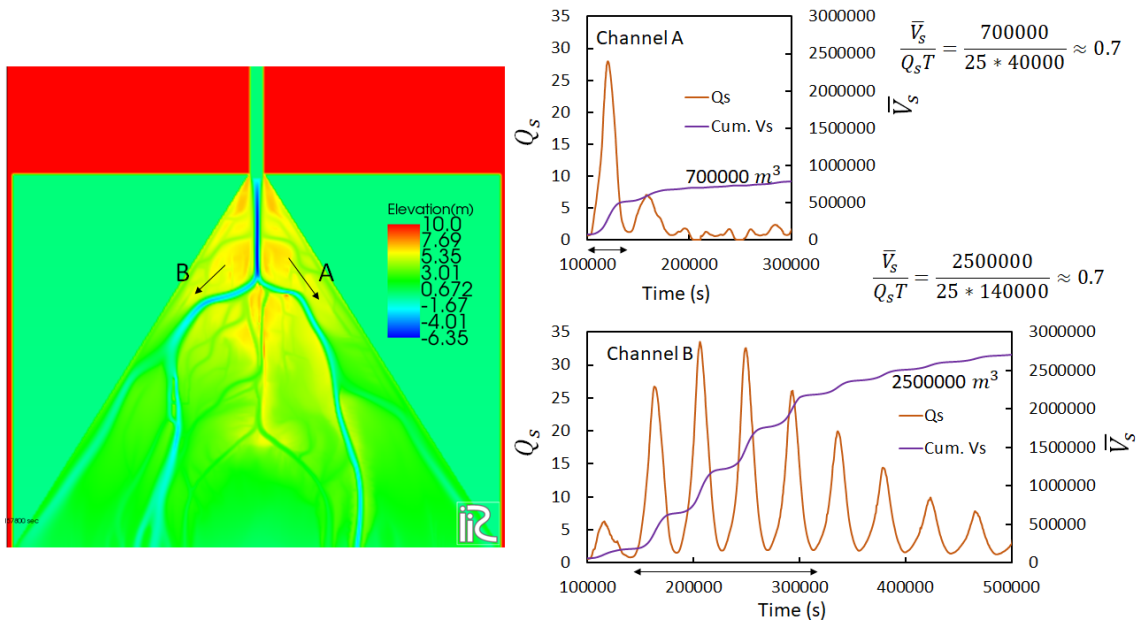


Figure 4.37 Suspended sediment discharge and its cumulated volume at different channels for Case 2

Figure 4.37 shows analysis of the ratio of cumulative volume of suspended sediment discharge and suspended sediment discharge along different channels for Case 2. Here the left channel is termed as Channel A and the right channel is termed as Channel B. For each channel, the lifetime, suspended sediment discharge and cumulative volume of suspended sediment discharges are also investigated following the Equations 40, 41 and 42. For this case also, the constant is found to be 0.7.

An asymmetric funnel shaped experimental domain which is identical to Sittuang river estuary is prepared to conduct periodicity of channel change on shorter scale. The dimensions, shape and physical properties of experimental domain are illustrated in Figure 4.38. The inflow channel is 700 m wide, the estuary is 30 km long and 40 km wide

at the outer boundary. General grid system is employed where Δx and Δy are same as 100 m along both x and y directions. Calculation conditions are specified in Table 5.

Table 5 Calculation conditions for asymmetrical funnel shaped experimental domain

Cases	Shape of estuary	Flow discharge at upstream end, Q (m^3/s)	Tidal motion at downstream $r =$ Amplitude (m)	Initial bed slope, i_b	Grid system $\Delta x =$ longitudinal $\Delta y =$ lateral
3	Asymmetric funnel shaped	3000	$T = 12$ hours $r = 2$ m	$\frac{1}{10000}$	$\Delta x = 100$ m $\Delta y = 100$ m
4		Measured discharge	Measured tidal motion	$\frac{1}{10000}$	

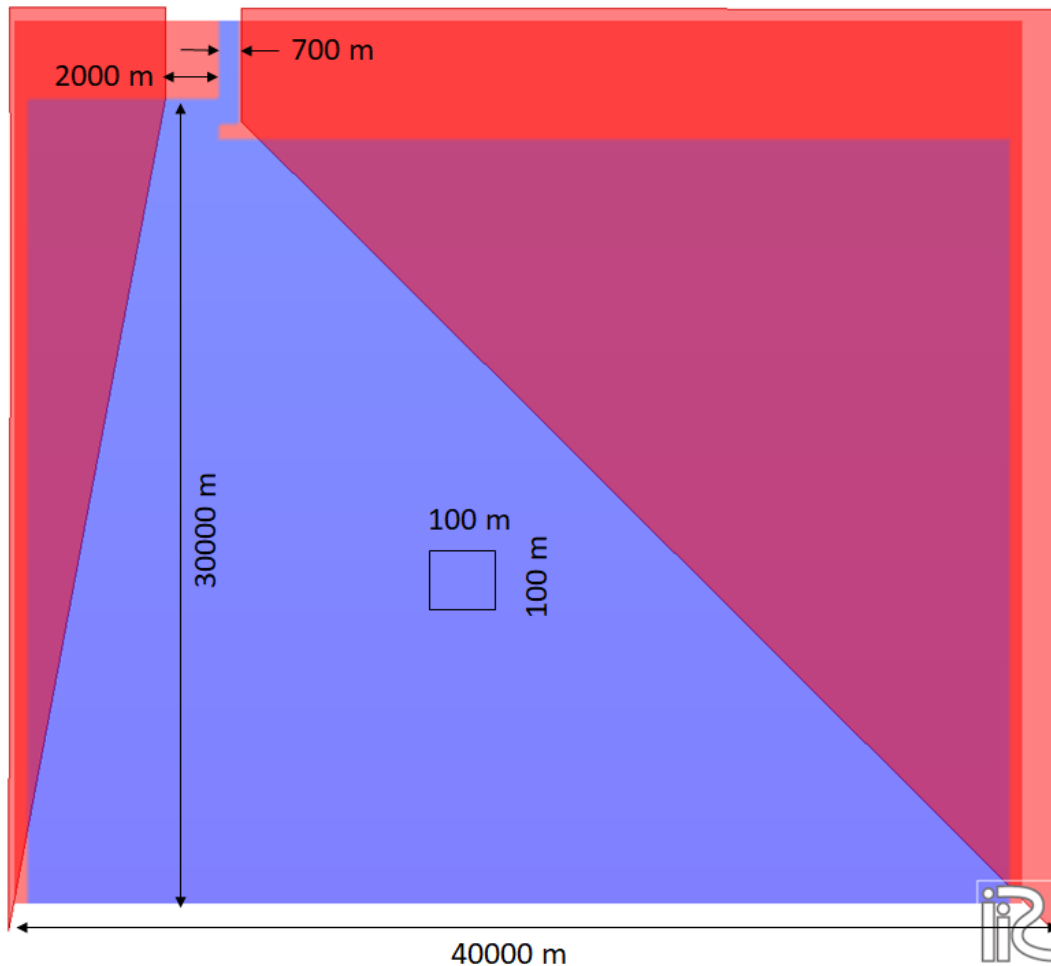


Figure 4.38 Experimental channel (asymmetric shape) to simulate decadal periodicity in a smaller scale

For Case 3, Average flood discharge of 3000 m³/s is employed as upstream boundary. In addition, tidal motion is specified at the downstream boundary as a sine curve with the amplitude of 2 m and the period of 12 hours. Reference grain size of bed material is specified as 0.03 mm based on the field investigation results. Initial bed surface is flat and inclines longitudinally in slope of 0.0001. Computation time step is 0.2 s.

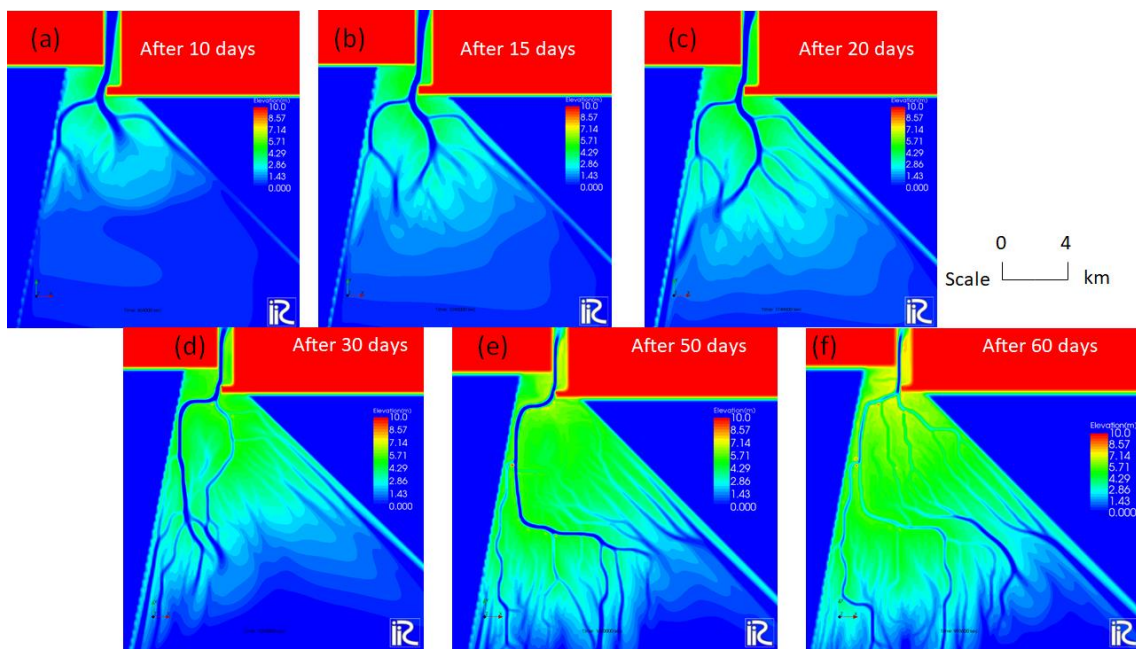


Figure 4.39 Developing process of channels with sand bars for Case 1 after computation of 10 days, 15 days, 20 days, 30 days, 50 days and 60 days

Figure 4.39 illustrates results of delta formation process with channels after 10, 15, 20, 30, 50 and 60 days of computation. Initially, channel bifurcation took place and both the bifurcated channels were flowing towards downstream. Then gradually the channel formed near the left bank and it became dominant. After 20 days of computation, it was seen that the channel near the left bank was dying and the alternate channel flowing near right bank became dominant. Then the channel kept flowing till 60 days and died. After that the flow started shifting towards left bank again. Such periodic switch is

observed in natural condition which is constituted by channel bifurcation characteristics and that is understood from such small basin scale numerical simulation.

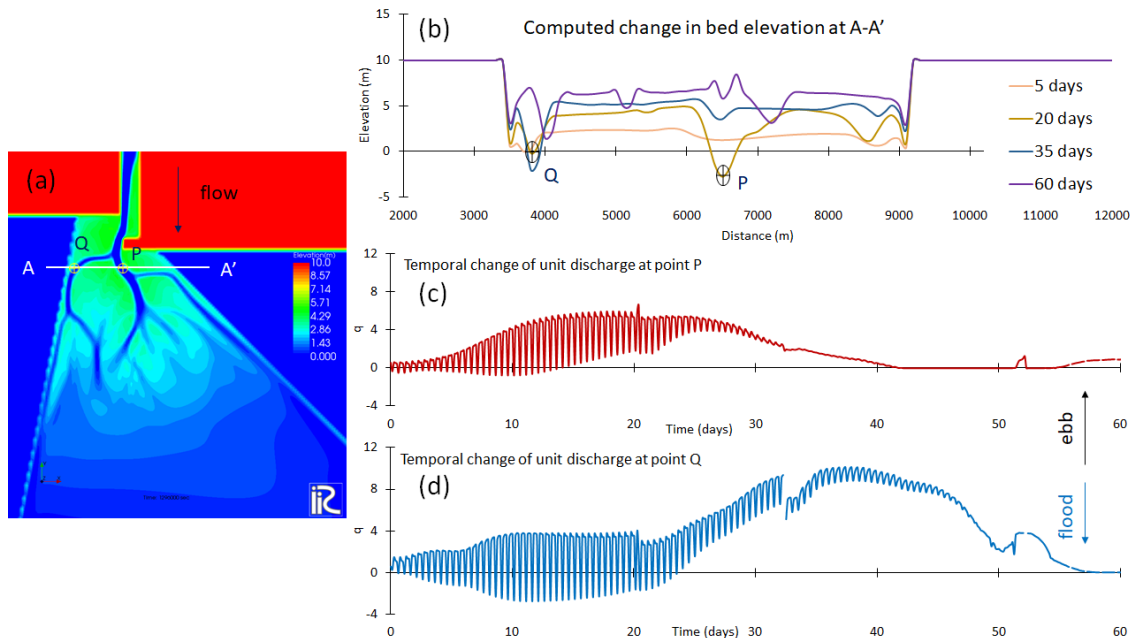


Figure 4.40 Temporal changes of cross-sectional shapes as well as of unit discharges at specified points for each channel

Cross-sectional shapes and unit discharges along the channels are investigated to understand channel formation and decay. Figure 4.40 shows the temporal changes of cross-sectional shape and the temporal changes of unit discharge at specified two points, P and Q within each channel. It is seen from Figure 4.40b that when deep channel remains at P, Q remains shallow, which means flow passes through P at first keeping the alternate channel shallow, then P becomes shallower and Q becomes deeper. Figure 4.40c,d shows computed unit discharges along the points P and Q where it is clearly seen that flow remains dominant at P during first 20 days, then gradually it died and Q became dominant and after 50 days it died. Such periodic change in flow pattern can be understood from shorter time and spatial scale simulation. To investigate periodicity of channel change on decadal scale which is observed in satellite images, measured discharge at Madauk and measured tidal motion at Mawlamyine (shown in Figure 2.1) are employed as upstream

and downstream boundary conditions in the computation domain illustrated in Figure 4.38. Such condition is described as Case 4 in Table 5. Figure 4.41a shows the measured discharge hydrograph during monsoon in one representative year and Figure 4.41b shows the measured tidal motion at the same time. Morphological acceleration factor is employed as 10. It is assumed that the inflow channel coming from the top resembles land and gradually widened shape towards outer boundary resembles the sea.

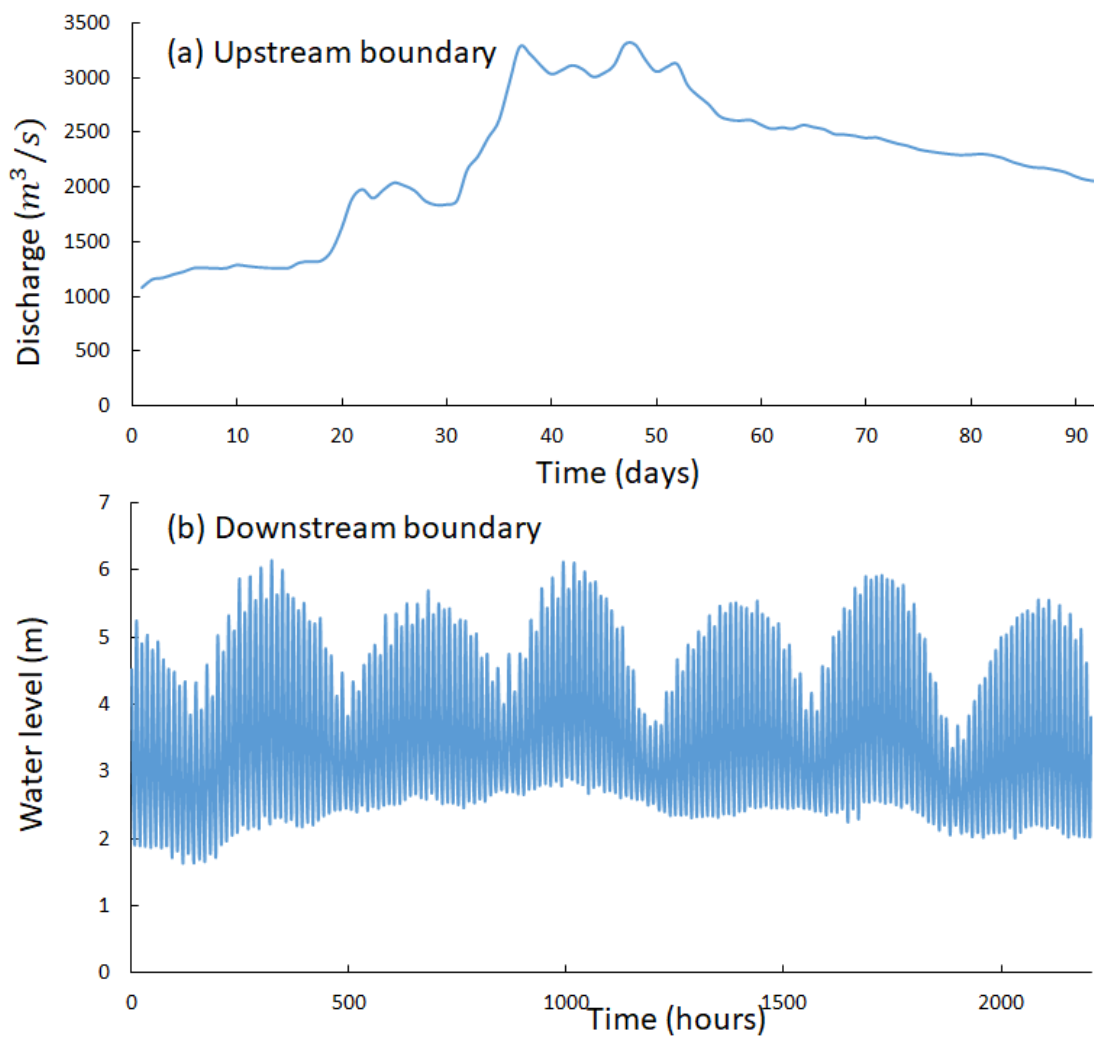


Figure 4.41 (a) Actual discharge hydrograph employed at upstream boundary and (b) corresponding measured tidal motion at Mawlamyine, employed as downstream boundary for Case 4

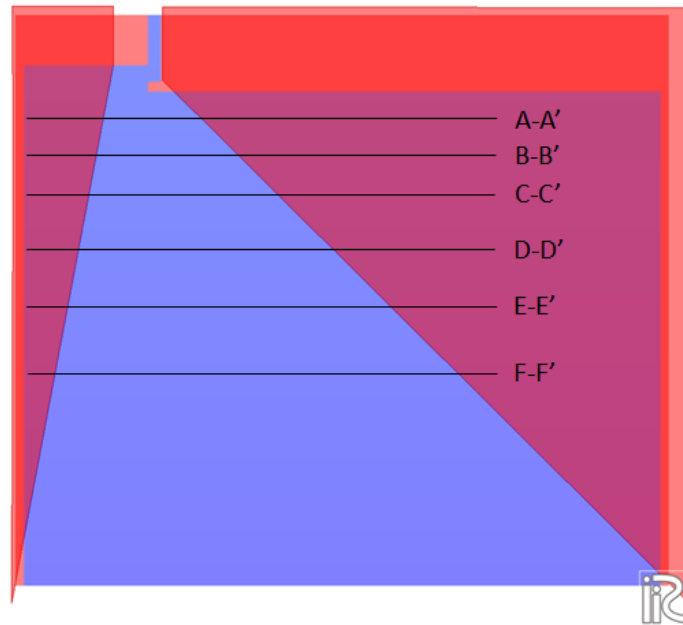


Figure 4.42 Specified cross-sections for investigating suspended sediment discharge and cumulative volume of suspended sediment discharge for Case 4

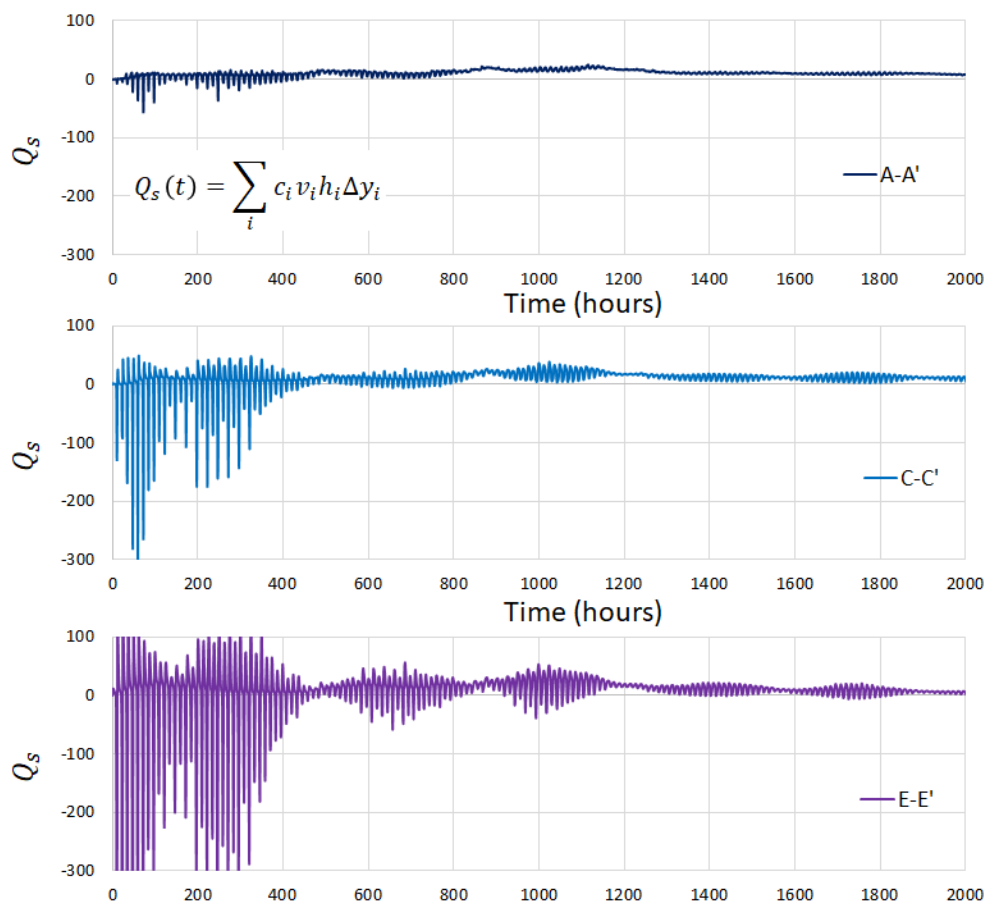


Figure 4.43 Temporal change of computed suspended sediment discharge at different cross-sections (see Figure 4.42) for Case 4

Suspended sediment discharges are investigated at different cross-sections which are illustrated in Figure 4.42. Figure 4.43 illustrates temporal change of computed suspended sediment discharge at cross-sections A-A', C-C' and E-E'. It is seen that suspended sediment flux at C-C' and E-E' are dominant towards landward direction. Such suspended sediment flux contributes to the delta formation process at the initial stage. However suspended sediment discharge is influenced by tidal motion as well as deposition pattern in the estuary.

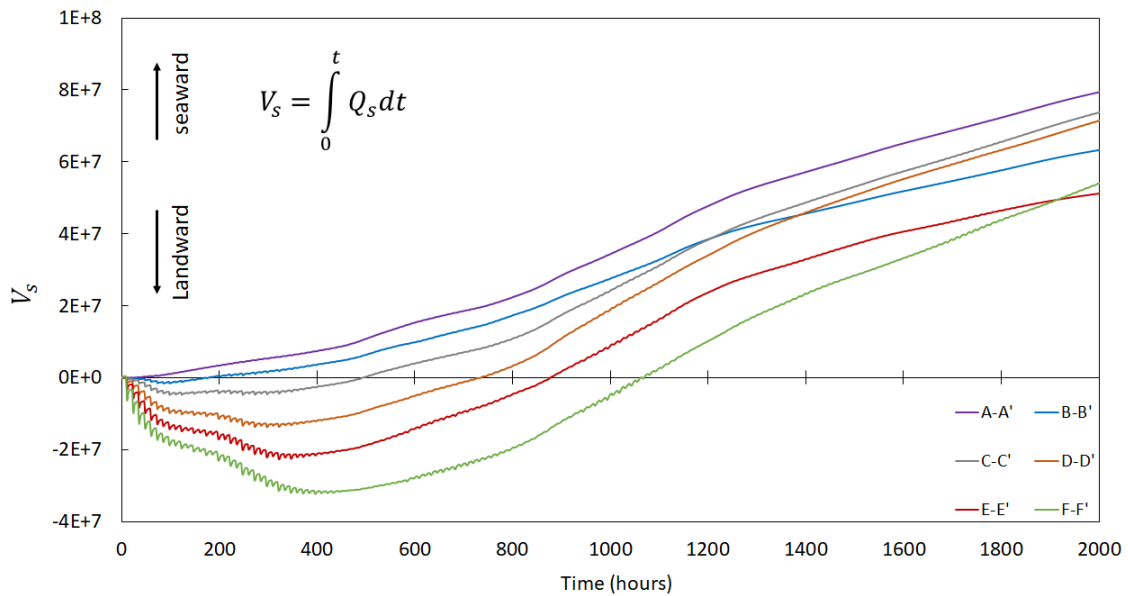


Figure 4.44 Temporal changes of cumulative volume of suspended sediment discharge at different cross-sections (see Figure 4.42) for Case 4

Figure 4.44 illustrates temporal change of cumulative volume of suspended sediment discharge at different cross-sections shown in Figure 4.42. It is seen that at A-A' and B-B', cumulative volume of suspended sediment flux are towards landward direction. However at C-C', D-D', E-E' and F-F', initially the flux was towards landward direction which contributed to the delta formation process and then gradually net flux of

suspended sediment turns to the seaward direction. Such cumulative volume of suspended sediment discharge plays key role to the delta formation process.

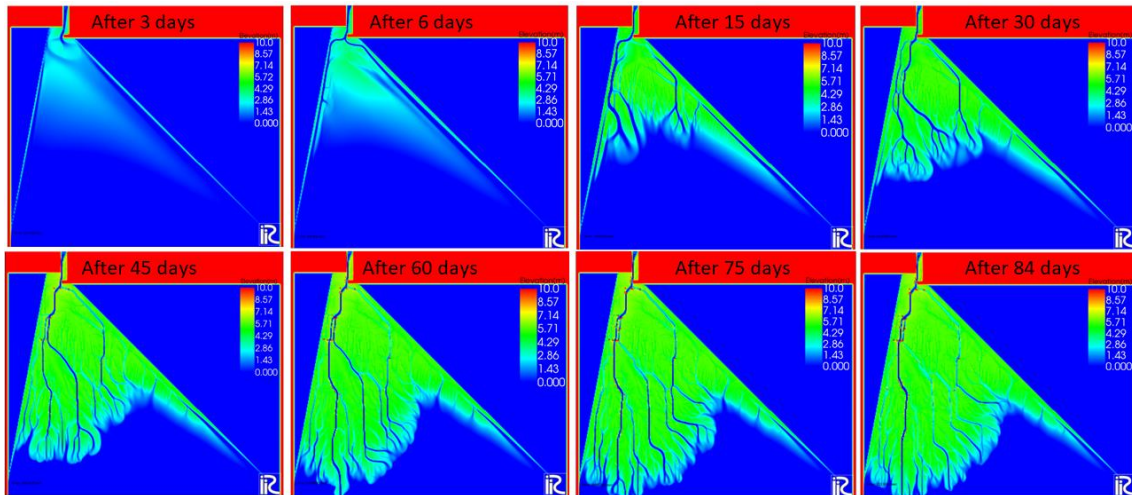


Figure 4.45 Developing process of channels with sand bars for Case 4 after computations of 3, 6, 15, 30, 45, 60, 75 and 84 days

Figure 4.45 illustrates delta formation process and changes in stream channel pattern for Case 4. It is clearly seen that initially, one major channel bifurcated into two and then gradually the left channel died and entire discharge started flowing through the right channel. After 15 days, the right channel started shifting towards middle of the estuary and then eventually it decayed. In the downstream part also several new branches formed and shifted to new locations. In view of the above discussions, it can be realized that periodic change in stream channel pattern and migration of sand bars are constituted by channel bifurcations. Such channel shift and characteristics of sediment transport identifies nature of periodic change in channel pattern and movement of sand bars in the estuary.

It requires long computation hours for predicting long term morphological change in the estuary. However, through employment of morphological acceleration factor as 10, periodic change is computed for short time period. Created morphology for Case 3 which

represents morphology in 2019 is employed as initial bed morphology, upstream and downstream boundary conditions are kept same as that explained for Case 3 in Table 1. Morphological acceleration factor is employed as 10. Bed evolution is computed for 15 days. Then the bed evolution is compared with satellite image in February, 2020.

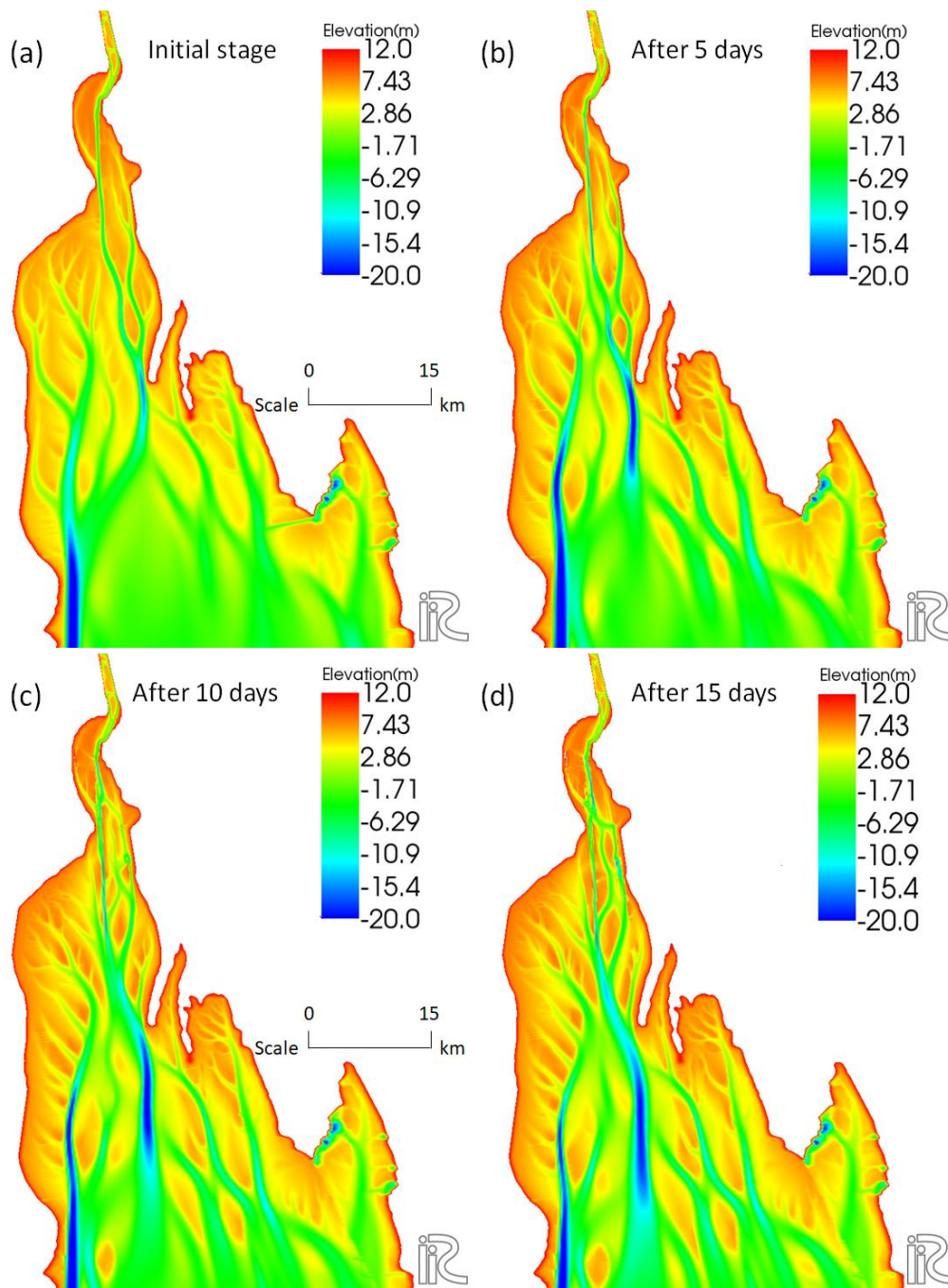


Figure 4.46 Developing processes of channel pattern with sand bars after computations of 5, 10 and 15 days using the initial configuration shown in (a)

Figure 4.46 illustrates sand bar deformation and corresponding channel changes computed on the previously created morphology. It is seen that channel bifurcations take place actively, deposition tendency is enhanced westwards and stream channel is shifting eastwards.

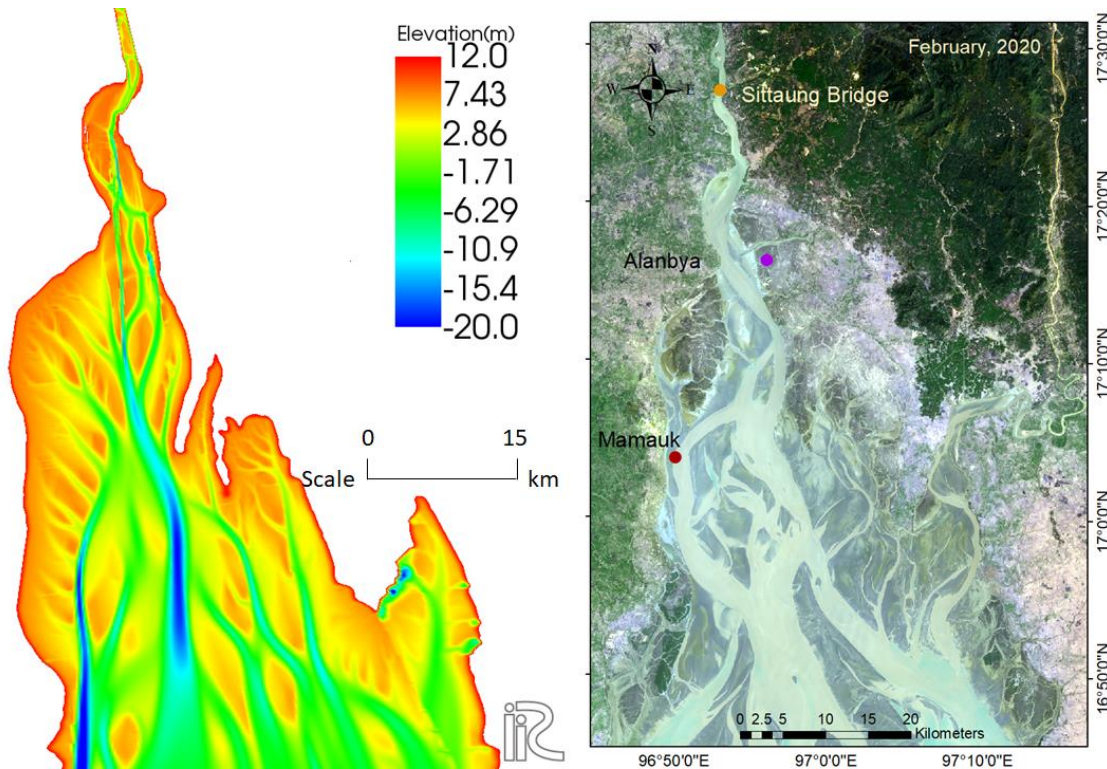


Figure 4.47 Comparison of the computed channel pattern with sand bars to recent satellite image

Figure 4.47 compares the bed evolution result with satellite image in February, 2020. It is clearly visible that due to channel bifurcation, near Alanbya, main channel shifted eastwards, divided into two channels near Mamauk and main flow is concentrated to the center towards further downstream. In addition, deposition zone at upstream of Mamauk is much prominent in the recent progress. To observe the channel pattern, velocity during ebb tide is investigated, too. Figure 4.48 illustrates velocity during ebb tide at initial stage as well as after 15 days. It is clearly seen that the main channel has moved to the center deposition has taken place westwards. In addition, channel

bifurcation has taken place leading to shifting of channels eastwards. On continuation of such kind of simulation, long term morphological change can be produced and such results could be helpful for policy makers to chalk out countermeasures. So using the present method, and with application of morphological acceleration factor, long term prediction of sand bar deformation and corresponding channel change could be obtained.

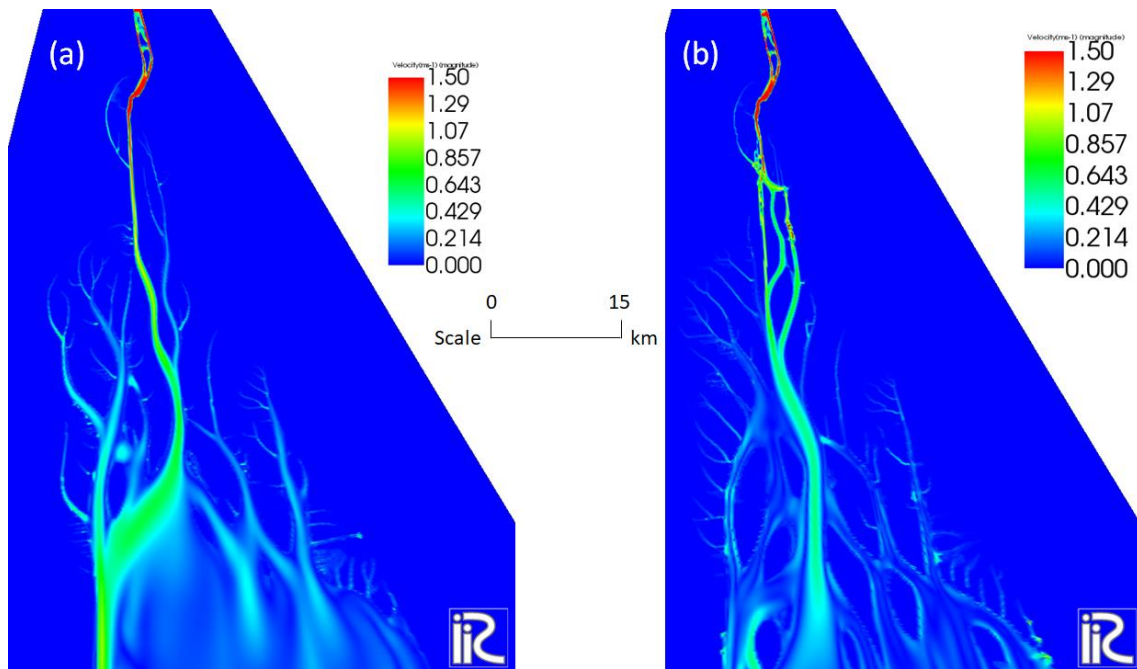


Figure 4.48 Spatial distribution of velocity during ebb tide at (a) initial stage and (b) after 15 days

4.6 Summary

Based on numerical results, this chapter discussed sand bar evolution with channel changes, sand bar control and developing process with channel bifurcation. The created bed morphology and velocity in ebb tide show channel patterns are reproduced well that can be compared with available satellite images. Sediment budget using estimation of cumulative volume of suspended sediment discharge shows net direction of suspended sediment transport in the estuary. On the created morphology, two types of boundary conditions are employed where tides of maximum and varied amplitudes are set as

downstream boundary conditions and it is understood that tidal range has significant impact on suspended sediment discharge in the estuary. The created morphology is employed as initial condition for bank erosion and it is realized that existing bank erosion needs some improvement. Different cases of spur dykes are employed to check applicability of the structures in sand bar and channel pattern control activity and it is realized that large spur dykes might be effective to combat against such strong bank erosion. Periodicity of channel change in a decadal to multi-decadal scale is understood by simulating in a shorter time and spatial scale that such phenomena could be reproduced numerically.

Chapter 5: Conclusion

This paper discusses tidal currents, sediment transportation and bed morphology as well as their mutual relations based on satellite image analysis, field surveys, and numerical simulation. Interesting results are obtained on the physical characteristics of the Sittaung River estuary, a simulation model of tidal currents, sediment transport and associated channel changes, as summarized below.

Chapter 1 describes the background, placement and location of this study through literature reviews with attention focused on the characteristics of estuary morphodynamics. The author explains the need for a study to understand the sediment transport process in estuaries where very fine sediment dominates, as well as the impacts of geomorphological changes on human society and the ecological system.

Chapter 2 describes the morphological and hydrological characteristics of the study area based on satellite image analysis and field investigation. Historical satellite images are analysed to show active changes in stream channels and sand bars which cause drastic bank-line shifts at a rate of around 1 km every year at the most active location. An asymmetric tidal range is observed with a shorter flood tide and a longer ebb tide. Bank erosion and associated sediment issues are discussed with attention focused on sediment particle sizes in the river reach and estuary as well as on the mechanism of bank erosion owing to tidal currents. The bed and banks of the estuary are found to be composed of very fine particles with average diameters of 0.02 to 0.04 mm. The existence of such fine particles increases the erodibility and transportability of bed materials and results in very active channel change, sand bar deformation and bank erosion. Bank erosion occurs in a cyclic process involving bank collapse and associated sediment supply to bank bases, the

elimination of deposited sediment and the erosion of base material by tidal currents. Analyses also point out that the sediment sizes of bed material along the reach change discontinuously at the boundary of the upper and lower reaches. Sediment constituting beds in the lower reach and the estuary is supplied by the bank erosion of the river reach and the estuary. The bank erosion of the estuary is caused mainly by strong tidal currents following the passage of a bore head.

Chapter 3 describes the weakness of existing formulas in treating fine sediments. To solve this issue, a new model is proposed for treating sediment transport process of very fine sediment and combined it with the depth-averaged two-dimensional Reynolds equations to simulate tidal bores, associated tidal currents, sediment transportation and active morphological changes. The proposed model is tested for validity, by being applied to the estimation of suspended sediment concentration and particle sizes.

Chapter 4 discusses the numerical results of sand bar evolution, the simulation of spur dykes as a possible structural countermeasure to erosion, and the analysis of channel bifurcation and lifetime. The development process of sand bars are simulated including the changing nature of stream channels and compared with those from available satellite images. Channel bifurcation and channel closing are also reproduced. The author explains that such channel-change elements are responsible for the development process of sand bars and that the cyclic change of the bank line shifting may be caused by stream channel bifurcation. Spur dykes are tested as potential structural interventions to prevent severe bank erosion in the estuary, the simulation verifies that they are an effective method. The periodicity of channel shifting on a decadal scale is simulated in the experimental basin. Such a tool to simulate tidal currents and sediment transportation is very useful for the

prediction of channel change, sand bar migration and vulnerable locations for bank erosion in the estuary. The proposed model can simulate tidal currents, sediment transportation, sand bar deformation and corresponding channel changes in estuary composed of very fine sediment. However we didn't have enough observed data to validate the model. So it is recommended to employ the proposed model at various other natural fields around the world and compare the computed results with observed data. In addition, improvement of the bank erosion model is a way forward. Major outputs of this study are as follows.

Present study identifies presence of very fine particles as bed and bank materials impacting erodibility and transportability of such materials due to influence of tidal currents. Proposed method is capable of simulating erosion rate of bed sediment that is composed of such fine particles with median grain size ranging 0.01 to 1 mm. Using such tool, stream channel pattern and sand bar migration can be predicted which will help identify vulnerable locations for bank erosion. Then hard and soft countermeasures on short and long term basis could be taken for protection of public properties from severe bank erosion problem. Based on the prediction made by numerical results, estuary management plans could be devised by relevant authorities of The Government of Myanmar. Possibility of construction of large spurs is tested that could be one probable countermeasure for checking erosion problem along both banks. Proposed method can be applied for prediction of sediment transport and channel change to the estuaries composed of fine materials. Such prediction would help decide policies for erosion control, drainage improvement and maintenance of navigability for ports and harbours.

Till now, bank erosion and subsequent adverse impacts are visible in Myanmar. But there was no good understanding about the physical processes and reasons and countermeasures. Present study discusses the problem, justifies the reasons behind such problem, proposes mathematical tool to predict sediment transportation and corresponding channel changes and recommends some countermeasures. Dissemination of such findings is an essential task for contribution to the actual field.

Directorate of Water Resources and Improvement of River Systems (DWIR) is responsible for conservation and protection of the water resources in Myanmar. In addition, Department of Meteorology and Hydrology (Myanmar) takes care of collection and preservation of hydrological information. Outputs of the study might be shared with these two core departments. Moreover, erosion problem, the tool and proposed countermeasures could be shared with the development partners like Japan International Cooperation Agency (JICA), Asian Development Bank (ADB), United Nations Office for Disaster Risk Reduction (UNDRR), United Nations Educational, Scientific and Cultural Organization (UNESCO), United Nations Environment Program (UNEP), Food and Agriculture Organization (FAO). Outputs of this study could be shared with several other non-government organizations are working for conservation of fisheries, agriculture and wildlife (especially seasonal birds) in the same area viz. Biodiversity and Nature Conservation Association (BANCA), International Union for Conservation of Nature (IUCN), Fauna & Flora International (FFI) and ArcCona Ecological Consulting. The World Water Council is another potential platform where the study outcome could be discussed. It is an international multi-stakeholder platform organization whose mission is to mobilize action on critical water issues at all levels, including the highest decision-

making level, by engaging people in debate and challenging conventional thinking. The Council focuses on the political dimensions of water security, adaptation and sustainability.

After discussing the key points of the study, it is recommended to arrange a Conference involving all the stakeholders mentioned above. The purpose of the conference is to promote actions, raise awareness and get attention of media and the public. The outputs of the study would be justified to convince potential organizers the reason why all people look that the conference have to happen. Any development partner or international organization of the Governmental department itself could take initiative to arrange a conference. It would depend on the party who might get interested in the outcomes of the study. Representatives from DWIR, Department of Meteorology and Hydrology, JICA, ADB, UNESCO, UNEP, UNDRR, FAO, BANCA, FFI, ArcCona, WWC, Political representatives and people's representatives from the affected areas could be potential attendees of the conference.

If the Government and the development partners are convinced with the study outcome, then it is important to decide the next steps forward on how to implement the outputs to the actual field. To perform such task, it is necessary to form committees and sub-committees and then assign them with specific tasks for preparation of action plan. To come to an agreement, a second Conference is to be held. Decision for arranging the second conference should come from the first conference. As the first conference would play role of the promoter, second conference is to set up the committee.

If and when the stakeholders find it convincing that this is quite good area of investment, then political decision is needed. Such message could be delivered and

decisions could be made in the conferences. To implement the outputs of the study, it is necessary to make the conference a success. In such a way the outputs could be utilized for improvement of socio-economic condition of people living alongside the estuary.

References

- Ahmed, T.S., Egashira, S., Harada, D., Yorozuya, A., Kwak, Y., Shrestha, B.B., Kuribayashi, D., Sawano, H., Koike, T., (2019), On bank erosion in estuary of Sittaung river in Myanmar, *Scour and Erosion IX-keh-Chia (Ed.)*, Taylor & Francis Group, London, ISBN 978-0-367-07467-8, 161-166.
- Ahmed, T.S., Egashira, S., Harada, D., Yorozuya, A., (2019), Sediment transportation and sand bar deformation owing to tidal currents in Sittaung river estuary, Myanmar, *Journal of Japan Society of Civil Engineers, Ser. B1 (Hydraulic Engineering)*, Vol. 75, No. 2, 1027-1032.
- Akiyama, J., and Fukushima, Y. (1986). "Entrainment of non-cohesive sediment into suspension." *3rd Int. Symp. on River Sedimentation*, S. Y. Wang, H. W. Shen, and L. Z. Ding, eds., Univ. of Mississippi, 804-813.
- Ashida, K., Fujita, M. (1986), Mechanism of particle suspension in an open channel, *Doboku Gakkai Ronbunshu*, 375, 79-88.
- Bartsch-Winkler, S., Lynch, D.K., (1988), *Catalog of worldwide tidal bore occurrences and characteristics*, U.S. Geological Survey Circular 1022, 17 pp.
- Bagnold, R. A., (1954), Experiments on a gravity-free dispersion of large solid spheres in a Newtonian fluid under shear. *Proc. Roy. Soc. London (A)* 225, 49.
- Bazin, M., (1865), Recherches hydrauliques experimentales sur la propagation des ondes, *Memoires presentes par divers Savants Etrangers a l'Academie des Sciences*, Paris 19, 495-652.

- Biswas, R.K., Yorozuya, A., Egashira, S., (2016), Numerical model for bank erosion in the Brahmaputra River, *Journal of Disaster Research*, Vol. 11, No.6, DOI: 10.20965/jdr.issn.1883-8030.
- Bonneton, P., Bonneton, N., Parisot, J.-P., and Castelle, B., (2015), Tidal bore dynamics in funnel-shaped estuaries, *J. Geophys. Res. Oceans*, 120, 923-941, DOI: 10.1002/2014JC010267.
- Celik, I., and Rodi, W. (1984). "A deposition entrainment model for suspended sediment transport." *Report SFB 210/T/6*, Universitat Karlsruhe, Karlsruhe, West Germany.
- Chanson, H., (1999), *The Hydraulics of Open Channel Flows: an Introduction*. Butterworth-Heinemann, Oxford, 512 pp.
- Chanson, H., (2001), Flow field in a tidal bore: a physical model, *Proceedings of the IAHR Congress, Beijing. Theme E. Tsinghua Universal Press*, 365-373.
- Chanson, H., (2011), Current knowledge in tidal bores and their environmental, ecological and cultural impacts, *Environ Fluid Mech*, 11:77-98, DOI: 1007/s10652-009-9160-5.
- Chanson, H., (2012), *Tidal bores, Aegir, Eagre, Mascaret, Pororoca: Theory and Observations*, World Scientific, Singapore, 200 pp.
- Dalrymple, R. W., Choi, K., (2007), Morphologic and facies trends through the fluvial-marine transition in tide-dominated depositional systems: A schematic framework for environmental and sequence-stratigraphic interpretation, *Earth-Science Reviews*, 81, 135-174.

- Dalrymple, R.W., Zaitlin, B.A., Boyd, R., (1992), Estuarine facies models: conceptual basis and stratigraphic implications, *Journal of Sedimentary Petrology (Society for Sedimentary Geology)*, Vol. 62, No. 6, 1130-1146.
- Davies, G., Woodroffe, C. D., (2010), Tidal estuary width convergence: Theory and form in North Australian estuaries, *Earth Surf. Proc. Land.*, 35, 737–749, <https://doi.org/10.1002/esp.1864>, 2010.
- DELTAWARES, (2016), *Delft3D Open Source Community*, Disponível em: <https://oss.deltares.nl/web/delft3d>. Acesso em: 12 Junho 2016.
- DHI, (2016), *MIKE powered by DHI*, Disponível em: <https://www.mikepoweredbydhi.com/>. Acesso em: 12 Junho 2016.
- Edmonds, D. A., Singerland, R. L. (2009). Significant effect of sediment cohesion on delta morphology. *Nature geoscience*, 105-109. doi: 10.1038/NGE0730.
- Egashira, S., Ashida, K., (1980), Studies on the Structures of Density Stratified flows, *Bulletin of the Disaster Prevention Research Institute*, 29(4), 165-198.
- Egashira, S., Miyamoto, K., Itoh, T., (1997), Bed load rate in view of two phase flow dynamics, *Annual Journal of Hydraulic Engineering, JSCE*, Vol. 41, 789-794.
- Einstein, H. A. (1950). "The bed load function for sediment transportation in open channels." *Technical Bulletin 1026*, U.S. Dept. of Agric, Soil Conservation Service, Washington, D.C.

- Einstein, H.A., Chien, N., (1953), Transport of sediment mixtures with large ranges of grain sizes, *University of California, Institute of Engineering Research*, Vol. 47, No. 4.
- Ellison, T.H., Turner, J.S., (1959), Turbulent entrainment in stratified flows, *Journal of Fluid Mechanics*, 6.3: 423-448.
- Engelund, F., and Fredsoe, J. (1976). "A sediment transport model for straight alluvial channels." *Nordic Hydrol.*, 7(5), 293-306.
- Engelund, F., Fredsoe, J., (1976), A sediment transport model for straight alluvial channels, *Nordic Hydrology*, 7, 293-306.
- Engelund, F., (1975), Steady transport of moderately graded sediment (part 2). *Progress Report No. 35, Inst. Hydrodynamics and Hydraulic Eng., Tech. Univ. Denmark.*
- Friedrichs, C.T., (2010), Barotropic tides in channelized estuaries, in *Contemporary Issues in Estuarine Physics*, Cambridge University Press, Cambridge, UK, 27-61.
- Fredstae, J., and Engelund, F., (1976), Bed concentration of suspended material. *Progress Report No. 39, Inst. Hydrodynamics and Hydraulic Eng., Tech. Univ. Denmark.*
- Garcia, M.H., Parker, G., (1991), Entrainment of bed sediment into suspension, *Journal of Hydraulic Engineering*, DOI: 10.1061/(ASCE)0733-9429(1991)117:4(414).
- Geleynse, N., Storms, J. E. A., Walstra, D. J. R., Jagers, H. R. A., Wang, Z. B., Stive, M. J. F. (2011). Controls on river delta formation; insights from numerical modelling. *Earth and Planetary Science Letters*, 302, 217-226. doi: 10.1016/j.epsl.2010.12.013.

- Harada, D., Egashira, S., Ahmed, T.S., Katayama, N., (2019), Erosion Rate of Bed Sediment by means of Entrainment Velocity, *Journal of Japan Society of Civil Engineers*, Ser. B1 (Hydraulic Engineering), Volume 75, Issue 4 (published).
- Hedley, P. J., Bird, M.I. & Robinson R.A. (2010). Evolution of the Irrawaddy delta region since 1850. *The Geographical Journal*, 176(2), 138–149. DOI: 10.1111/j.1475-4959.2009.00346.x.
- International team studies world's last uncharted major river delta (2018, May 31) retrieved 16 March 2020 from <https://phys.org/news/2018-05-international-team-world-uncharted-major.html>
- Itakura, T., Kishi, T., (1980), Open channel flow with suspended sediment, *Jour. Hydraulic Div.*, Vol. 106, HY. 8, pp. 1325-1343.
- Leuven, J.R.F.W., de Haas, T., Braat, L., Kleinhans, M.G., (2018), Topographic forcing of tidal sandbar patterns for irregular estuary planforms, *Earth Surface Processes and Landforms*, 43(1), 172-186.
- Leuven, J.R.F.W., Selakovic, S., Kleinhans, M. G., (2018), Morphology of bar-built estuaries: empirical relation between planform shape and depth distribution, *Earth Surf. Dynam.*, 6, 763–778, doi: 10.5194/esurf-6-763-2018.
- Liu, J.P., Kuehl, S.A., Pierce, A.C., Williams, J., Blair, N.E., Harris, C., Aung, D.W., Aye, Y.Y., (2020), Fate of Ayeyarwady and Thanlwin rivers sediments in the Andaman sea and Bay of Bengal, *Marine Geology*, 423, 106-137.
- Lynch, D.K., (1982), *Tidal bores*, Scientific American 247, 131-143.

- Lin, B.Y., (2008), *Characters of Qiantang Bore*, Chinese Ocean Press, Beijing, 212 pp, in Chinese.
- Martin, J., Sheets, B., Paola, C., Hoyal, D. (2009). Influence of steady base-level rise on channel mobility, shoreline migration, and scaling properties of a cohesive experimental delta. *Journal of Geophysical Research*, 114, F03017, doi: 10.1029/2008JF001142.
- Matamin, A.B.D., Ahmad, F., Mamat, M., Abdullah, K., Harun, S., (2015), Remote sensing of suspended sediment voer Gulf of Martaban, *Ekologia (Bratislava)*, Vol. 34, No. 1, 54–64, DOI: 10.1515/eko-2015-0006.
- Madsen, P.A., Simonsen, H.J., Pan, C.H., (2005), Numerical simulation of tidal bores and hydraulic jumps, *Coastal Engineering*, 52, 409-433.
- Morley, C.K., (2013), Discussion of tectonic models for Cenozonic strike-slip fault-affected continental margins of mainland SE Asia, *Journal of Asian Earch Science*, 76, 137-151, DOI: 10.1016/j.jseaes.2012.10.019.
- Nelson, J.M., Shimizu, Y., Abe, T., Asahi, K., Gamou, M., Inoue, T., Iwasaki, T., Kakinuma, T., Kawamura, S., Kimura, I., Kyuka, T., Mcdonald, R.R., Nabi, M., Nakatsugawa, M., Simoes, F.R., Takebayashi, H., Watanabe, Y., (2016), The International River Interface Co-operative: Public domain flow and morpho-dynamics software for education and applications. *Advances in Water Resources*, Vol. 93, pp. 62-74, 2016.

- Pan, C.H., Lin, B.Y., Mao, X.Z., (2007), Case Study: Numerical Modeling of the Tidal Bore on the Qiantang River, China, *Journal of Hydraulic Engineering, ASCE*, 133:130-138, DOI: 10.1061/(ASCE)0733-9429(2007)133:2(130).
- Peixoto, R.D.S., Rosman, P.C.C., Vinzon, S.B., (2017), A morphodynamic model for cohesive sediment transport, *Brazilian Journal of Water Resources, RBRH, Porto Alegre*, v. 22, e57, DOI: 2318-0331.0217170066.
- Ramaswamy, V., Rao, P.S., Rao, K.H., Thwin, S., Rao, N.S., Raiker, V., (2004), Tidal influence on suspended sediment distribution and dispersal in the northern Andaman Sea and Gulf of Martaban, *Marine Geology*, 208, 33-42.
- Rao, P.S., Ramaswamy, V., Thwin, S., (2005), Sediment texture, distribution and transport on the Aeyarwady continental shelf, Andaman Sea, *Marine Geology*, 216, 237-247.
- Riddler, M.P., (2017), *The tidal bore in the Sittaung river, a sensitivity analysis of the propagation* (Additional thesis), Master Hydraulic Engineering and Water Resource Management at the Delft University of Technology. An electronic version of this thesis is available at <http://repository.tudelft.nl/>
- Rijn, L.C.V., (1986), Mathematical modelling of suspended sediment in non-uniform flows. *Journal of Hydraulic Engineering*, 112(6), 433-455.
- Robinson, R.A.J., Bird, M.I., Oo N. W., Hoey T.B., Aye M. M., Higgitt D.L., Lhaing W. S., (2007), The Irrawaddy river sediment flux to the Indian Ocean: the original nineteenth century data revisited. *Journal of Geology*, 115, 629-640.
- Rossi, V. M., Kim, W., Lopez, J. L., Edmonds, D., Geleynse, N., Olariu, C., Steel, R. J., Hiatt, M., Passalacqua, P. (2016). Impact of tidal currents on delta-channel

- deepening, stratigraphic architecture, and sediment bypass beyond the shoreline.
Geology. doi: 10.1130/G38334.1.
- Rowbotham, F., (1983), *The Severn Bore*, David and Charles, Newton Abbot, UK, 3rd edition, 104 pp.
- Rubey, W.W., (1933), Settling velocities of gravel, sand and silt particles, *Am. Jour. Sc.-Fifth series*, Vol. XXV, No. 148, 325-338.
- Savenije, H.H.G., (2005), *Salinity and Tides in Alluvial Estuaries*, Elsevier, N.Y.
- Shimozono, T., Tajima, Y., Akamatsu, S., Matsuba, Y., Kawasaki, A., (2019), Large-scale channel migration in the Sittaung river estuary, *Scientific Reports*, 9:9862.
- Simpson, J.H., Fisher, N.R., Wiles, P., (2004), Reynolds stress and TKE production in an estuary with a tidal bore, *Estuarine, Coastal and Shelf Science*, 60, 619-627.
- Smith, J. D., and McLean, S. R. (1977). "Spatially averaged flow over a wavy surface." *J. Geophys. Res.*, 82(12), 1735-1746.
- Sindhu, B., Unnikrishnan, A.S., (2013), Characteristics of tides in the Bay of Bengal, *Marine Geodesy*, 36:377-407.
- Steijn, R.C., Cleveringa, J., Leuven, J.R.F.W., van der Baan, J., van der Zanden, J.J.G., (2019). Extreme coastal dynamics of Sittaung estuary (Myanmar), *Proceedings of the 10th International Conference on Asian and Pacific Coasts (APAC 2019) Hanoi, Vietnam*, 1193-1200, DOI: 10.1007/978-981-15-0291-0_163.
- Stuart, J.M.B., (1932), *The Sittaung River and its Vagaries*, Selected Engineering Papers, Institute of Civil Engineering, London, No. 127, 3-16.
- TELEMAC-MASCARET, (2016), *Open Telemac-Mascaret*, Disponivel em: <https://www.opentelemac.org/>. Acesso em: 12 Junho 2016.

- The 3rd field survey in the Sittaung River of Myanmar to investigate riverbanks and coastal erosion. (2019, April). *ICHARM News @ a Glance*. Retrieved from <http://www.icharm.pwri.go.jp/>
- Tricker, R.A.R., (1965), *Bores, Breakers, Waves and Wakes*, Mills & Boon, London, 33-80.
- Van Rijn, L. C. (1984). "Sediment transport, Part II: Suspended load transport." *J. Hydr. Engg.*, 110(11), 1613-1641.
- Wolanski, E., Williams, D., Spagnol, S., Chanson, H., (2004), Undular tidal bore dynamics in the Daly Estuary, Northern Australia, *Estuarine, Coastal and Shelf Science*, 60, 629-636.
- Wolanski, E., Williams, D., Spagnol, S., Chanson, H., (2004), Undular tidal bore dynamics in the Daly Estuary, Northern Australia, *Estuarine, Coastal and Shelf Science*, 60, 629-636.
- Yamashita, T., Aung, H., (2016), Projection and historical analysis of hydrological circulation in Sittaung river basin, Myanmar, *Journal of Civil Engineering and Agriculture*, 10, 736-742, DOI: 10.17265/1934-7359/2016.06.012.
- Xie, D., Pan, C., Gao, S., Wang, Z.B., (2018), Morphodynamics of the Qiantang estuary, China,: controls of river flood events and tidal bores, *Marine Geology*, 406, 27-33.
- Yu, Q., Wang, Y., Gao, S., Flemming, B., (2012), Modelling the formation of a sand bar within a large funnel-shaped, tide-dominated estuary: Qiantangjiang Estuary, China, *Marine Geology*, 299-302, 63-76.